Università Politecnica delle Marche
Scuola di Dottorato di Ricerca in Scienze dell'Ingegneria
Corso di Dottorato in Ingegneria Industriale

Energy efficiency of buildings: Dynamic simulations and experimental analyses.

Ph.D. Dissertation of:

Serena Summa

Supervisor:

Prof. Costanzo Di Perna

Ph.D. Course coordinator:

Prof. G. Di Nicola

XX edition - new series

Università Politecnica delle Marche
Scuola di Dottorato di Ricerca in Scienze dell'Ingegneria
Corso di Dottorato in Ingegneria Industriale

Efficientamento energetico degli edifici: Simulazioni dinamiche e analisi sperimentali.

Ph.D. Dissertation of:

Serena Summa

Supervisor:

Prof. Costanzo Di Perna

Ph.D. Course coordinator:

Prof. G. Di Nicola

XX edition - new series

To Aaron

Università Politecnica delle Marche
Dipartimento di Ingegneria Industriale e Scienze Matematiche (DIISM)
Via Brecce Bianche — 60131 - Ancona, Ita

Acknowledgements

I wish to thank Prof. Costanzo Di Perna for his assistance, support and collaboration during my doctoral period. I am grateful to all the technicians who helped me in the experimental activities and to all the students who contributed to their realisation. My thanks also go to all the people who worked with me during this period, especially my office colleagues.
A special thanks goes to my ex-Prof. Ettore Fedeli who, thanks to his passion for teaching, succeeded in instilling in me a curiosity towards science and knowledge in general.

Ancona, January 2022

Serena

Abstract

The studies reported in this thesis add to the current body of knowledge a contribution concerning both new dynamic hourly calculation models, useful for a reliable assessment of the energy needs of buildings, and innovative construction solutions to improve the energy efficiency of buildings and thus decarbonise the construction sector currently responsible for about 40% of global climate-changing gas emissions.

The new calculation models contained in the recent standards published by CEN are analysed, namely EN ISO 52016-1:2017 "Energy demand for heating and cooling, indoor temperatures and sensible and latent heat loads - Part 1: Calculation procedures" and the related EN ISO 52010-1:2017 "Outdoor climatic conditions - Part 1: Conversion of climate data for energy calculations". These standards offer the possibility to estimate energy requirements and operative temperatures with similar accuracy to that of major simulation software (such as Trnsys or Energy Plus), but in a less onerous way. As both standards are recently published, there are not enough studies in the literature to identify the actual validity of the methods and the fields of application. For this reason, using Tnsys as a basis, a comparative and sensitivity analysis was carried out, the main criticalities were identified and alternative calculation methods were proposed which, appropriately integrated into the standards, improved their accuracy.

At an experimental level, innovative construction solutions were proposed to improve winter and summer energy requirements, respectively with the study of a hyper-insulated building integrated with a solar greenhouse equipped with controlled mechanical ventilation and with the study of three different ventilated facades, also integrated with controlled mechanical ventilation, optimised using machine learning techniques.

Finally, the impact of climate change on current NZEBs in terms of needs and comfort was assessed, according to two scenarios proposed by the IPCC (Intergovernmental Panel on Climate Change): RCP4.5, which foresees a reversal of CO_2 emissions by 2070 and a maximum temperature increase of 2°C, and RCP8.5, which uses a "business-as-usual" approach and foresees quadruple CO_2 concentrations by 2100, with a temperature increase of more than 4°C.

Sommario

Gli studi riportati in questa tesi aggiungono all'attuale corpus di conoscenze un contributo riguardante sia i nuovi modelli di calcolo dinamico orario, utili per una valutazione affidabile del fabbisogno energetico degli edifici, sia le soluzioni costruttive innovative per migliorare l'efficienza energetica degli edifici e quindi decarbonizzare il settore delle costruzioni attualmente responsabile di circa il 40% delle emissioni globali di gas climalteranti.
Vengono analizzati i nuovi modelli di calcolo contenuti nelle recenti norme pubblicate dal CEN, ovvero la EN ISO 52016-1:2017 "Fabbisogno energetico per il riscaldamento e il raffreddamento, temperature interne e carichi di calore sensibile e latente - Parte 1: Procedure di calcolo" e la relativa EN ISO 52010-1:2017 "Condizioni climatiche esterne - Parte 1: Conversione dei dati climatici per i calcoli energetici". Tali norme offrono la possibilità di valutare il fabbisogno energetico e le temperature operative con un'accuratezza simile a quella dei principali software di simulazione (come Trnsys o Energy Plus), ma in modo meno oneroso. Essendo entrambi gli standard di recente pubblicazione, non esistono in letteratura studi sufficienti ad identificare l'effettiva validità dei metodi e i campi di applicazione. Per questo motivo, utilizzando Tnsys come base, è stata effettuata un'analisi comparativa e di sensibilità, sono state individuate le principali criticità e proposti metodi di calcolo alternativi che, opportunamente integrati nelle norme, ne hanno migliorato l'accuratezza.
A livello sperimentale sono state proposte soluzioni costruttive innovative per migliorare il fabbisogno energetico invernale ed estivo, rispettivamente con lo studio di un edificio iperisolato integrato ad una serra solare dotata di ventilazione meccanica controllata e con lo studio di tre diverse facciate ventilate, anch'esse integrate a ventilazione meccanica controllata, ottimizzate tramite tecniche di machine learning.
Infine, è stato valutato l'impatto del cambiamento climatico sugli attuali NZEB in termini di fabbisogni e comfort, secondo due scenari proposti dall'IPCC (Intergovernmental Panel on Climate Change): RCP4.5, che prevede un'inversione delle emissioni di CO_2 entro il 2070 e un aumento massimo della temperatura di 2°C, e RCP8.5, che utilizza un approccio "business-as-usual" e prevede concentrazioni di CO_2 quadruple entro il 2100, con un aumento della temperatura di oltre 4°C.

Contents

List of Figures

1990, I,d/b (6): Boland/Ridley 2007+Liu/Jordan 1960, I,d/b (7): Erbs 1982+Perez 1990, I,d/b (8): Reindl 1990+Perez 1990

Figure B1.3 Comparison between the models for separation of direct (I,b) and diffuse (I,d) solar irradiance on the vertical plane for the Malaga location. I,d/b (5): Perez 1991+Perez 1990, I,d/b (6): Boland/Ridley 2007+Liu/Jordan 1960, I,d/b (7): Erbs 1982+Perez 1990, I,d/b (8): Reindl 1990+Perez 1990.

Figure B1.4 Comparison between the models for separation of direct (I,b) and diffuse (I,d) solar irradiance on the vertical plane for the Paris location. I,d/b (5): Perez 1991+Perez 1990, I,d/b (6): Boland/Ridley 2007+Liu/Jordan 1960, I,d/b (7): Erbs 1982+Perez 1990, I,d/b (8): Reindl 1990+Perez 1990.

Figure B1.5 Comparison between the models for separation of direct (I,b) and diffuse (I,d) solar irradiance on the vertical plane for the Rome location. I,d/b (5): Perez 1991+Perez 1990, I,d/b (6): Boland/Ridley 2007+Liu/Jordan 1960, I,d/b (7): Erbs 1982+Perez 1990, I,d/b (8): Reindl 1990+Perez 1990.

Figure B1.6 Comparison between the models for separation of direct (I,b) and diffuse (I,d) solar irradiance on the vertical plane for the Stockholm location. I,d/b (5): Perez 1991+Perez 1990, I,d/b (6): Boland/Ridley 2007+Liu/Jordan 1960, I,d/b (7): Erbs 1982+Perez 1990, I,d/b (8): Reindl 1990+Perez 1990.

List of Tables

Table B2.5 - Comparison of standard statistical parameters for the Stockholm location. Evaluation against Trnsys' algorithm of all oriented vertical surfaces. Gray cells are those with the minimum error

Nomenclature

The following abbreviations are used in this thesis:

U	Thermal trasmittance	W/(m^{2}K)
Ms	Surface mass	kg/m²
YIE	Periodic thermal transmittance	W/(m^{2}K)
fa	Attenuation factor	-
φ/phi	Phase shift	h
κj	Internal areal heat capacity	kJ/(m²K)
Ctot	Total heat capacity	kJ/(m²K)
ggl	Total solar energy trasmittance	-
ggl,n	Total normal transmittance of solar energy	-
Fw	Exposition factor	-
Isol,dir/dif,t	Direct/diffuse solar radiation incident on the glazed surface	W/m^2
Fsh,obst,t	Shading reduction factor	-
ϑsol,t	Angle of incidence of direct solar radiation	°
p	Number of glass panels	-
q	Coefficient of glass coating type	-
θe	Outdoor temperature	°C
IH	Horizontal solar radiation	W/m^2
HDD	Heating degree days	-
α_{sol}	Solar altitude angle	°
βic	Surface tilt angle from horizon	°
γic	Orientation angle of the inclined surface (surface azimuth)	°
δ	Declination	°
δ_r	Rayleigh's extinction factor	-
Δ	Sky brightness parameter	-
ε	Clearness parameter	-
$\theta_{sol,ic}$	Solar angle of incidence on the inclined surface	°
θ_z	Solar zenith angle	°
λw	Longitude	°
$\rho_{sol;grnd}$	Solar reflectivity of the ground (Albedo)	-
φ_{sol}	Solar azimuth angle	°
φ_w	Latitude	°
ω	Hour angle	°
$G_{sol;b}$	Direct solar irradiance on horizontal plane	W/m^2

$G_{sol;bn}$	Direct normal (beam) solar irradiance	W/m^2
$G_{sol;c}$	Solar costant	W/m^2
$G_{sol;d}$	Diffuse solar irradiance on horizontal plane	W/m^2
$G_{sol;g}$	Global solar irradiance	W/m^2
H	Altitude	m
I_{circum}	Circumsolar irradiance	W/m^2
I_{dir}	Direct irradiance	W/m^2
$I_{dir;tot}$	Total direct irradiance	W/m^2
I_{ext}	Extra-terrestrial radiation	W/m^2
$I_{ext,h}$	Global extra-atmospheric solar irradiance on a horizontal plane	W/m^2
$k_{T,d}$	Clearness index of the atmosphere (relating to diffuse radiation)	-
m	Relative optical air mass	-
m_0	Relative optical air mass (see level)	-
n_{day}	Day of the year	-
n_{hours}	Actual (clock) time for the location	-
Rdc	Earth orbit deviation	◦
t_{eq}	Equation of time	hh
T_L	Linke turbidity coefficient	-
t_{shift}	Time shift	hh
t_{sol}	Solar time	hh
TZ	Time zone (UTC – Universal Time Coordinated)	-

Chapter 1.
Introduction

Buildings and their construction represent more than a third of the world's final energy consumption and almost 40% of total direct and indirect CO^2 emissions.
The International Energy Agency (IEA) has estimated that in order to obtain a carbon-neutral building stock by 2050 and move closer to the Paris agreement target [1], direct and indirect CO^2 emissions must be reduced by 50% and 60% respectively [2] by 2030. How to do this? In the construction sector, the possible actions listed in the latest EPBD [3] are essentially six: (i) energy efficiency of the building envelope on new and existing buildings, (ii) the use of innovative building materials and solutions, (iii) microclimate control, (iv) the use of high-efficiency electric heat pumps or other carbon-free systems, (v) intelligent controls (domotics) and (vi) digitisation for a better energy efficiency policy.
The research activities carried out during the PhD and the topics of this thesis are mainly related to the topics listed in the first three points of the above-mentioned list and will be explained below.
Improving the performance of the building envelope is key to reducing greenhouse gas emissions by 2050. Although all countries will have to implement mandatory building codes within the next decade to satisfy Net Zero ambitions, most have not yet made them an explicit policy priority [4]. Energy codes provide a simple and economic way to verify the minimum energy performance requirements set by countries in order to reduce energy consumption and address the issues of increased dependence on energy imports, scarcity of energy resources, the need to limit climate change and the need to overcome the economic crisis.
To help Member States to correctly implement the new EPBD [3], the European Commission mandated the European Committee for Standardization (CEN) to develop a complete set of standards (ISO 52000 series) in order to have a systemic approach for energy performance assessment taking into account the dynamic interaction between systems, users and external climate variations. Among the main standards are EN ISO 52016-1:2017 *"Energy needs for heating and cooling, internal temperatures and sensible and latent heat loads - Part 1: Calculation procedures"* [5] and EN ISO 52010-1:2017 *"External climatic conditions - Part 1: Conversion of climatic data for energy calculations"* [6] which, being recently published, are not well reflected in the literature in terms of validation.
For this reason, after presenting a general overview of the energy efficiency of buildings in Chapter 2, a comprehensive analysis of the accuracy of the dynamic hourly calculation method of EN ISO 52016-1:2017 [5] is carried out in Chapter 3 of this thesis, focusing in particular on the evaluation of heat transfer through the opaque elements of the building

envelope. Using the thermoelectric analogy, the standard models each opaque element with a fixed network of resistors and capacitors (RC).
This model is compared in terms of energy requirements, as well as with Trnsys, with the model proposed by Italy in the national annex of the standard (Annex A), in which the number and position of the capacitive nodes and resistive layers varies according to the thermophysical characteristics of the real layers of the opaque component. This study also identifies the main critical issues that lead EN ISO 52016-1 to deviate from the energy requirements calculated by Trnsys [7]. In addition to the heat transfer model of the opaque elements, the use of constant values of the thermal transmittance of the transparent elements and the use of constant values of the solar transmittance coefficient (ggl) lead to strong divergences. For this reason, an alternative algorithm to the standard for the calculation of the solar transmittance coefficient is proposed and tested. This algorithm, by varying the ggl at each time step according to the angle of incidence of direct solar radiation, leads to a better alignment with Trnsys of the solar loads, especially in the summer season.
In Chapter 4, a closely related standard to EN ISO 52016-1:2017 [5] is evaluated and validated, namely EN ISO 52010-1:2017 "External climatic conditions - Part 1: Conversion of climatic data for energy calculations"[6]. A correct evaluation of the energy consumption of the building implies an accurate assessment of the solar gains and consequently an exact estimation of the direct and diffuse solar radiation on inclined and oriented surfaces. In this chapter, the calculation algorithm contained in EN ISO 52010-1:2017 is analysed and an alternative calculation procedure is proposed. These two algorithms are then compared with two other solar radiation fractionation methods implemented in Meteonorm[8] and Trnsys [7]. In order to test the performance and limitations of the different calculation algorithms, a comparative analysis between these methods was carried out on five European cities with different climatic characteristics. Using the algorithm contained in Trnsys as a baseline, the criticalities of EN ISO 52010-1:2017 regarding the calculation of direct, diffuse and global irradiance on vertical surfaces starting from the horizontal global irradiance were highlighted, which were then overcome by the proposed calculation algorithm.

Promoting research and testing of innovative building materials and solutions is another point listed in the EPBD 2018/844 that can improve the energy performance of existing and new buildings. In a context where about 75% of the EU building stock is inefficient, promoting a 3% annual renovation with smart solutions and energy efficient materials would lead to a reduction of total energy consumption by 5-6% and carbon dioxide emissions by about 5% [3][9].
In this context, a promising construction technique on both new and existing buildings is ventilated facades (VF). In the Chapter 5, a comparative analysis is conducted on three types of VFs, with emphasis on a novel design variant that couples the benefits of (i) replacing multi-layer assemblies with a monolayer structure that uses cement-bonded wood fiber blocks' air gaps as ventilated cavities and (ii) easy-to-implement and cost-saving design,

notably regarding the details of the metallic support. The novel design variant is compared with two heavyweight, multi-layered designs, that differ in the position of the massive layer with respect to the ventilated cavity. In this study, a thermophysical analysis is performed on each design variant under equal boundary conditions and under the influence of controlled mechanical ventilation in the cavity, in order to investigate the dynamic response of the envelope. An experimental dataset was built-up by varying the operating parameters during the month-long monitoring campaign on a test-room with all VF variants aligned on the same wall. For the data analysis, an approach based on machine learning algorithms was used to predict the cavity temperatures and heat fluxes of the individual VFs. By training three different regression algorithms on the collected data, low prediction errors were obtained, particularly for temperatures. Using these models, the thermophysical behaviour of the VFs was simulated and the most energy-efficient design variant was determined.
Another technical solution to improve the energy efficiency of existing and new buildings is passive solar systems, including bioclimatic solar spaces. Bioclimatic solar spaces are essentially solar greenhouses adjacent to the air-conditioned thermal zones (ztc) of buildings that transfer heat radiatively to the interior space, contributing positively to the winter energy balance. However, these systems, being exclusively radiative, are not very 'reactive' and ineffective when used on hyper-insulated buildings and/or buildings with high thermal mass. For this reason, in Chapter 6, an experimental study is presented to investigate the integration of a mechanically controlled ventilation system (VMC) on the partition between the ztc and the solar greenhouse, in order to integrate radiative and convective heat transfer.
The VMC, operating through an inlet hole located near the ceiling and an outlet hole located near the floor, is activated whenever the temperature of the solar space exceeds the temperature inside the conditioned space by a predetermined deltaT (2, 1 or 0.5 °C). The set-point of the ztc is reached by prioritising the activation of the fans over the heating terminals (electric radiators). This study has shown what is the optimal configuration (i) for the glass surface of the solar greenhouse, (ii) for the VMC activation threshold with regard to the electrical consumption and the degree of comfort inside the ztc, and (iii) for the climatic boundary conditions.

While buildings and related activities are responsible for a significant proportion of greenhouse gas emissions, they also represent a major opportunity to limit climate change. Although the number of countries committing to achieving zero emissions in the coming decades continues to grow, their actions still fall short of what is needed to bring global energy-related carbon dioxide emissions to zero by 2050 [2]. Based on the mitigation strategies to be taken in the coming years, the United Nations' Intergovernmental Panel on Climate Change (IPCC) provided its fifth report on the effects of climate change (AR5) in 2014 [10].
The report shows in four scenarios (RCPs - Representative Concentration Pathways) how the climate could change by 2100 according to different levels of mitigation implemented by

countries. Under bold mitigation strategies, greenhouse gas emissions could be halved by 2050 with a maximum temperature increase of 2 °C, while under a 'business-as-usual' approach, atmospheric CO^2 could increase four times over pre-industrial levels with temperature differences of more than 4 °C. The corresponding change in global and local climatic conditions will have an impact on the energy requirements of the existing building stock and, consequently, on primary energy demand.

For this reason, in Chapter 7, the impact of climate change on (i) the heating and cooling consumption of an nZEB multi-family house designed according to current Italian regulations [11], and (ii) the comfort level achieved inside the building according to the adaptive theory [12] and to a long-term evaluation [13] was evaluated.

Three dataset were predicted: (i) current climate conditions, (ii) 2050 - RCP8.5 climate conditions , (iii) 2050 - RCP4.5 climate conditions. The current climatic data are developed on a data set of temperatures and solar irradiances measured between 2000-2009 and 1991-2009, respectively; while future scenarios are simulated through ERA-Interim / UrbClim [14]. This model shows that Rome is the location with the highest temperature increase in Italy, as a consequence of the climate change and the urban heat island effect; therefore, this city was chosen as case study.

Finally, Charpter 8 reports some critical conclusion and the future advancements of the work presented.

The topics discussed in the various chapters are extracted from the following scientific articles:

- **Chapter 3**: “Comparative and Sensitivity Analysis of Numerical Methods for the Discretization of Opaque Structures and Parameters of Glass Components for EN ISO 52016-1” [15]
- **Chapter 4**: “Evaluation of ISO 52010-1: 2017 and proposal for an alternative calculation procedure” [16]
- **Chapter 5**: “Combining artificial intelligence and building engineering technologies towards energy efficiency: the case of ventilated façades” [publishing]
- **Chapter 6**: “Sunspace coupling with hyper-insulated buildings: Investigation of the benefits of heat recovery via controlled mechanical ventilation” [17]
- **Chapter 7**: “Impact of climate change on the energy and comfort performance of nzeb: A case study in Italy” [18]

Chapter 2.
Overview of energy efficiency in buildings

2.1. European Union Directives

In terms of legislation, Europe first addressed the issue of energy efficiency in buildings in 1993 with the focus on limiting carbon dioxide emissions with Directive 1993/76/EC [15], known as SAVE [19]. This Directive required Member States to develop and implement programmes to improve (i) energy efficiency in public and private buildings, (ii) insulation of new buildings, (iii) regular inspection of boilers, (iv) energy audits of energy-intensive companies, (v) energy metering of cooling and hot water systems, (vi) invoicing of heating costs and (vii) the financing of energy efficiency investments in the public sector through third parties.

Subsequently, the evident consequences of climate change expressed internationally by the Kyoto Protocol [20] in 1997 (the first international agreement containing commitments by industrialised countries to reduce emissions of greenhouse gases responsible for global warming), prompted Europe to release a series of EU laws (EPBD I - II - III and EED) aimed at dictating stricter obligations and performance requirements, facilitating energy certification of buildings and promoting the use of renewable energy sources in substitution to traditional energy sources.

In 2002, Directive 2002/91 EPBD [21] (Energy Performance of Buildings Directive) was introduced to promote the improvement of the energy performance of buildings in the European Community, taking into account local and external climatic conditions. In particular, it required (i) the definition of a methodology for calculating the energy performance of buildings in order to certify them, (ii) the definition of minimum energy requirements for new buildings and large existing buildings subject to major renovation, (iii) the regular inspection of boilers and air conditioning systems and (iv) the verification of their performance. The calculation method also had to take into account the thermal characteristics of the building, the heating and hot water systems, the air conditioning systems, the controlled mechanical ventilation, the lighting system, the presence of shading systems and the quality of indoor comfort, and had to highlight the advantages of adopting active solar systems and other systems for generating heat from renewable energy sources, cogeneration systems, district heating and cooling.

Article 7 also introduced the obligation for Member States to adopt, at the time of construction, sale or rental, the energy performance certificate (ACE), made available by the owner to the future buyer or tenant.

The 2002 EPBD highlighted the necessity for the construction sector to improve its standards in order to make a real contribution to the reduction of greenhouse gas emissions.
For this reason, in 2010 the Directive 2010/31/EU [22] called EPBD II "Recast" was adopted, introducing the concept of "nearly Net Zero Energy Building" (NZEB), i.e. very high performance buildings, with very low or almost zero energy requirements and covered to a significant extent by energy from renewable sources produced on site. A new concept is also introduced to help understand the meaning of 'nearly zero', namely the concept of 'cost-optimal energy performance level'. Each Member State, taking into account investment costs related to energy, maintenance, operation and disposal, had to determine which level of energy performance of the building represents the lowest cost (cost optimum) during the estimated economic life cycle.
To this end, with the intention of providing a common comparative methodology, in July 2011 the European Commission released an initial draft of the Guidelines that envisaged the creation, for each Member State, of "reference buildings" representative of national building types on which to calculate the minimum energy performance levels. By encouraging Member States to promote energy efficiency through incentive measures, the directive established that from 1 January 2021 all new buildings should be NZEB. As with the first EPBD, the Recast emphasises the importance of having a suitable energy performance assessment methodology but adds a differentiation of calculation according to building category.
In this context a change in building design is initiated, favouring the recovery and energy requalification of the existing patrimony and pushing new buildings towards reduced consumption covered by clean energy sources and giving considerable importance to technologies with decentralised energy supply systems based on renewable sources such as cogeneration, district heating or cooling and heat pump systems.

In 2012, Directive 2012/27/EU (EED) [23] extends the obligations to European countries and establishes a common framework to guarantee a 20 % energy efficiency improvement by 2020, also setting indicative national targets. Member States are obliged to (i) ensure annual energy savings of 1. 5% per year for energy suppliers and distributors, (ii) to ensure that 3% of the total surface area of the buildings owned and occupied by the central government is renovated each year to respect the minimum energy performance requirements it has set in application of Article 4 of Directive 2010/31/EU, (iii) to acquire only products, services and buildings with high energy efficiency, and (iv) to guarantee end customers competitive prices for electricity, natural gas, district heating, district cooling and domestic hot water in order to accurately measure consumption and actual time of use.

In 2018, Directives 2010/31/UE [22] and 2012/27/UE [23] are revised by the third version of the EPBD, namely Directive 2018/844/EU [3]. The EPBD III sets new energy and climate

targets, such as reducing greenhouse gas emissions by at least 40% by 2030 and developing a sustainable, competitive, secure and decarbonised energy system by 2050.
To achieve these objectives, a number of innovations are introduced, the most important of which are (i) the obligation to improve the energy performance of new and existing buildings, (ii) supporting electric mobility and the development of appropriate recharging infrastructures, and (iii) promoting the installation of automation and control systems for technological systems in buildings (domotics). The new directive, in fact, in addition to the already existing building classification based on energy performance, introduces an "indicator of building predisposition to intelligence". The purpose of this indicator is to make owners and occupants aware of the value of automation and electronic monitoring of technical building systems through smart technologies in order to adapt energy consumption to the real needs of occupants, maximising energy savings.

2.2. European Standards

For the first time, Directive 2002/91/EC (EPBD) [21] required the European Commission to define a methodology for calculating the energy performance of buildings. Although in many European countries the monthly calculation for the assessment of the annual energy consumption for heating was done with EN 832:1998 [24] (later evolved into EN ISO 13790:2004 [25]), the calculation of cooling requirements was absent and the calculation of plant and primary energy was not unified at all. In the following years, due to the increased use of air conditioning and the increase in energy consumption in summer, EN ISO 13790:2008 [26] was published, which not only provided a dynamic calculation method, but also implemented the monthly calculation method with the assessment of the cooling energy needs of residential and non-residential buildings.
Directive 2002/91/EC, in the absence of European standards capable of covering the whole building calculation, limited itself to listing a number of factors to be taken into account in evaluating energy performance. At the same time, however, the European Commission gave CEN the task of developing a package of standards for the application of the entire Directive which, according to the 2008 CENSE project, resulted uncoordinated, ambiguous, uneven and not translatable into software.
In 2010 with the publication of Directive 2010/31/EU [22], the Commission was again concerned about the lack of unified and interconnected European calculation methods, so in 2012 it decided to give CEN a second mandate to revise all 40 standards of the previous EPBD package. In addition to defining the contents of all standards and including a dynamic hourly method to be used as a basis for checking the legal requirements, the coordination group established a common structure for all documents in the preliminary phase of work. Each standard had to: (i) have exclusively normative contents, (ii) have a supplementary technical report in the case of informative contents, (iii) be tested and demonstrated with a

spreadsheet and (iv) have a template specifying all necessary calculation data and all default application data (Annex A) in order to make the calculation algorithm usable even in the absence of national specifications (Annex B) [27]. After the preliminary phase, the real revision work began. From 2013 to 2016, the whole EPBD package was revised and in 2017 CEN published the new set of standards: EN ISO 52000 [28]. Nowadays, this series defines a comprehensive method of calculating the energy performance of buildings capable of taking into account users, external climatic variations and the whole dynamics between technical systems, considering the total primary energy consumed as the sum of the primary energies of heating, cooling, lighting, ventilation and hot water (see Fig.2.1).

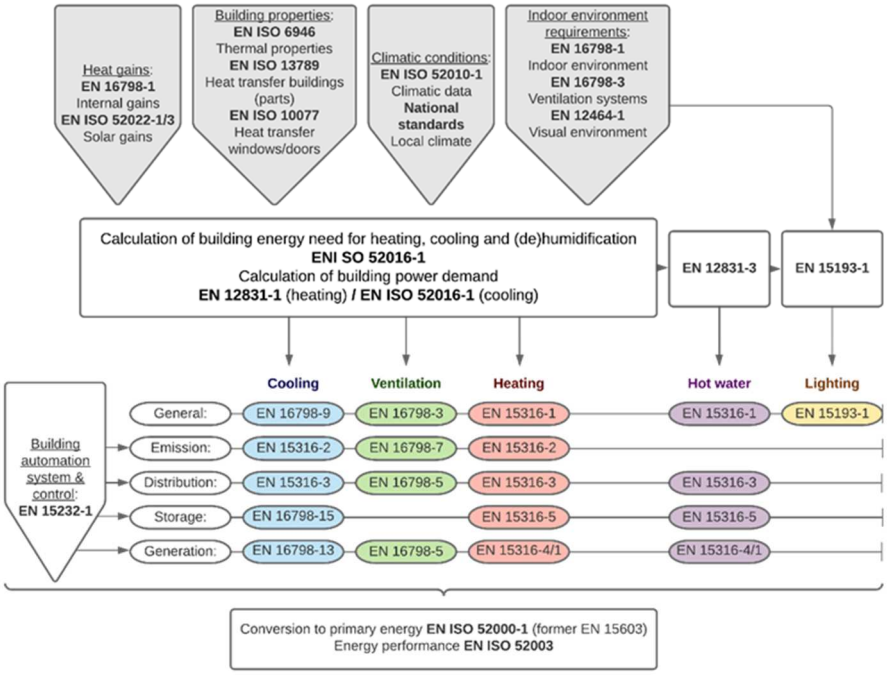

Figure 2.1. Main technical standards of the new EPBD package.

Among all the standards, special attention should be given to EN ISO 52016-1. This standard proposes two calculation methods for estimating the energy needs of buildings: a stationary monthly method and a dynamic hourly method. In particular, the dynamic method (evolution of the dynamic method of EN ISO 13790:2008 [26]) is extremely necessary for the calculation of summer needs, because these are governed by much more variable phenomena than winter ones, and for the calculation of buildings with intermittent systems, especially those in the tertiary sector. In Table 1, the main differences between the methods of EN ISO 13790:2008 [26] and EN ISO 52016-1 [5] are shown, but in the following (Chapter 3) only the hourly dynamic method of EN ISO 52016-1[5] will be described.

Table 2.1. Main differences between the monthly and dynamic calculation method of EN ISO 13790 and EN ISO 52016-1.

	EN ISO 13790		**EN ISO 52016-1:2018**	
	Monthly	**Hourly**	**Monthly**	**Hourly**
Element discretisation	-	Model with 5 resistances and 1 capacitance	-	The number of resistances and capacitances is variable according to the characteristics of the element in question.
Solar gain	The solar radiation incident on opaque and transparent components, as well as the extraflows, compose the final value of the solar gains.		The solar radiation incident on the transparent surfaces composes the final value of the solar gains while the radiation incident on the opaque components and the extraflows are calculated with the envelope dispersions.	
Thermal zoning	There are 5 criteria for defining thermal zones		A 10-step procedure is defined to identify thermal zones.	
Adjacent unconditioned areas	Only one type of adjacent unconditioned zone is defined. The correction coefficient (btr) is applied to the heat transfer coefficients		Two types of adjacent non-air-conditioned zones are defined. The correction coefficient (btr) is applied to the temperatures	
Calculation of system intermittency	The correction coefficient (a_{red}) is applied to the thermal energy needs.	The system's hourly operating profiles are used	The correction coefficient (a_{red}) is applied to the temperatures in the winter case and to the heat energy needs in the summer case.	The system's hourly operating profiles are used
Humidification and dehumidification	-	-	Humidification is calculated as the sum of the incoming, outgoing and internally produced steam flow rates. Dehumidification is related to the need for thermal energy for cooling..	The humidification and dehumidification is calculated as the difference of incoming and outgoing water vapour flow rates and the internal production and other parameters.

2.3. Literature review

In order to reach the ZEB target, energy efficiency measures must be applied to both new and existing buildings. In particular, existing buildings, due to their very poor energy performance and their high number compared to new buildings, play a major role in achieving the goal of reducing energy demand.

2.3.1 New buildings

The performance of new buildings is increased year by year according to the requirements imposed by regulatory developments and available technical solutions.
Currently, experimental studies in the literature show that building geometry and morphology (form factor and window-wall ratio WWR) can limit energy needs and promote indoor comfort. Particularly in cold regions, the optimisation of heat flows is performed using low form factors (compact buildings) [29–31], while in warmer regions, in order to avoid overheating, special attention should be paid to orientation, WWR, shading, low insulation and the effect of free-cooling [32].The latter technique, combined with heat recovery and controlled mechanical ventilation systems, allows for increased efficiency in new buildings.
Another fundamental aspect for achieving NZEB highlighted in the literature is the use of geothermal heat pumps (HP) coupled with photovoltaic (PV), although the performance of the latter is closely linked to the latitude of the site.
Last but not least is energy management through the use of advanced controls and intelligent systems such as BEMS (Building Energy Management System). These, in addition to managing the technical systems [31,33–35], allow, thanks to the control of heating, cooling and ventilation, to optimize internal comfort in terms of temperature and air exchange [30,36,37].

2.3.2 Renovated existing buildings

There is a large overview in literature in terms of energy efficiency in existing buildings. The most suitable technologies for achieving the ZEB target can be grouped into three categories: (i) passive and active efficiency measures, (ii) generation and power systems, and (iii) energy control and management strategies.

(i) Passive efficiency measures are intended to reduce consumption by using the geometry of the building, the thermo-physical characteristics of the materials, the floating mechanism that favours ventilation, thermal inertia and the evaporative effect [38]. Consumption reduction can be achieved by: optimising the size of the windows in relation to the opaque element, depending on glazing systems, shading systems and

façade orientation. [39–41]; increasing the thermal resistance of the envelope in order to reduce heat loss in the winter period [42–45]; using natural ventilation and solar radiation respectively in solutions such as Trombe Walls and Solar Chimneys to achieve passive heating and cooling [46–50]; or reducing solar albedo by installing green roofs and walls in order to lower solar loads and consequently summer needs [51–56].

Active solutions for heating, cooling and lighting mainly include HVAC systems, radiant systems that can reduce consumption by 10% to 80% depending on system configuration and control strategies [57], controlled mechanical ventilation [58,59] and LED lamps [60,61]. According to the state of the art, conventional HVAC systems are responsible for half of the energy consumption in buildings, so solutions to improve their energy efficiency have been tested in recent decades. One of these is thermal energy storage (TES) [62–64] in order to optimise the efficiency of the system and another is the recovery of sensible and latent heat, which must however be balanced with the electrical energy consumed by the fans[65,66].

(ii) Regarding generation systems, the most studied in the literature are solar and wind power systems, heat pumps, district heating/cooling systems and bioenergy. Photovoltaic technology is the most commonly used technology in the building sector as it is easily scalable, produces electrical power in proportion to the surface area exposed and gives good results from both an energy and environmental point of view [67,68]. For this reason, various technologies have been added to PV to maximise the potential of this system such as: photovoltaic-thermal technology (PVT) designed to keep the photovoltaic panel at the optimal temperature for absorbing solar radiation, increasing the total conversion efficiency and using waste heat to produce hot water[69] or BIPV (building-integrated photovoltaic) technology, i.e. systems designed to be integrated into the building envelope to replace traditional passive building elements, such as roof and facades, windows, shutters and blinds [70].

In addition to photovoltaics, there is wind power, which converts mechanical energy into electricity. Compared to photovoltaic panels, wind turbines are more limited in their use because they are closely linked to the site and the presence of wind. In order to overcome this limitation and bring wind power into an urban environment, Lee et al have shown that small vertical axis wind turbines (VAWT) can pick up turbulent winds much better than horizontal axis turbines, a fundamental characteristic in urban contexts.[71–74].

Among the generation systems mentioned in the literature are heat pumps. Studies on the residential building stock show that heat pumps (HP), by using renewable energy sources (aerothermal, hydrothermal and geothermal), are able to bring considerable energy savings to the building. Air source HPs (ASHP), in particular

air-water HPs, and Water and Ground Source HPs (WSHP and GSHP) are able to save between 20% and 40% of the building's energy in the case of energy refurbishment [75,76].

Another effective system described in the literature, which differs from the others in its centralised energy production, is district heating/cooling (DH/DC).

Tele-energy is more efficient than individual systems because it can efficiently manage and control the overall energy network[77], producing electricity and heat at the same time. Many studies have shown how the integration of renewable energies (solar, HPs and biomass) can improve energy, economic and environmental performance and help achieve the NZEB objective [78–80].

(iii) Regarding energy control and management strategies, there are two solutions: Building Automation Systems (BAS) and Building Energy Management Systems (BEMS). BAS, currently under development, allow the optimisation of different services and devices such as HVAC, ACS, lighting and shading systems, energy conversion and storage, on-site energy generation, monitoring and data management, communications and security management [81], reducing consumption by up to 40% [82]. BEMS, on the other hand, more studied in the literature, have excellent potential in terms of energy saving and environmental impact [83,84]. These systems, made up of sensors that connect with the environment and communicate with actuators, are able to control and regulate the consumption and comfort of buildings through specific algorithms [85–88].

Chapter 3.
Comparative and sensitivity analysis of numerical methods for the dynamic calculation of the building energy needs

3.1 EN ISO 52016-1:2017 in Literature

The necessity to reduce the energy demand of buildings by 80% (compared to 1990) by 2050 [89] and CO^2 emissions [90], has prompted the European Committee for Standardisation (CEN) to approve a package of new standards to support the implementation of the Energy Performance Building Directive (EPBD) [91]. In particular, EN ISO 52016-1:2017 [92] introduced a new methodology for the hourly calculation of energy needs for heating and cooling, that allows to investigate the dynamic energy performance of buildings. This standard shows great potential but currently there are not enough studies in the literature to validate its accuracy. Application studies used the standard to evaluate the summer performance of Trombe walls [48] or to assess the impact of highly massive envelope on the energy performance of a building [93]. In Ref. [94] the authors compare the energy requirements, obtained with the semi-stationary monthly method of EN ISO 13790, with the dynamic hourly method of the Standard and show discrepancies up to 100% for the winter period and up to 11% for the summer period. Congedo et al [95] want to demonstrate that the hourly monitoring of the indoor operating temperature, according to EN ISO 52016, allows to univocally define the performance of the building, especially in terms of indoor comfort. Comparative studies, such as that of Ballarini et al [96], argue that the main causes of deviation between the new hourly model and dynamic software, such as EnergyPlus, can be mainly attributed to usage of different surface heat transfer coefficients and a different modelling of the extra thermal radiation to the sky. Also, the work proposed by Zakula et al [97],[98] shows that the discrepancies between EN ISO 52016-1:2017 and Trnsys (albeit with acceptable CVRSME values), are mainly caused by three factors: (i) the use of constant values for the window transmittance (Uw), (ii) the use of constant values for the solar transmission coefficient (gw) and (iii) minimally the calculation of heat transfer through opaque elements. Concerning the latter aspect, the work carried out by Mazzarella et al [99] (incorporated in the Italian national annex of the standard), proposes an alternative method for the spatial discretization of the nodes of opaque structures based on the material and distribution of the effective layers. Analyses on individual walls have shown that this alternative method provides a more accurate approximation than the method proposed in the main text of the International Standard.

The purpose and novelty of this work is to answer some problems that emerged from the previously mentioned studies and to expand the current knowledge of EN ISO 52016-1:2017[92]. In fact, for the first time it was:

- tested the new method described in Annex A (Italian Annex) of EN ISO 52016-1:2017 [92];
- proposed a model capable of varying the ggl at each time step (1 hour), according to the orientation of the window and the angle of incidence of solar radiation;
- explored the effects of thermo-physical parameters of opaque surfaces on building energy needs through a sensitivity analysis of the Italian annex, the European annex and Trnsys.

In addition to identifying the application limits and problems of the standard, as already done in other works in the literature, this work proposes solutions that improve the hourly dynamic method of EN ISO 52016-1 [92], bringing the results closer to those obtained with Trnsys.

3.2 Methods

In order to identify the hourly energy demand for heating and cooling under different boundary conditions, three methods were compared. The following were used: (i) the calculation procedure defined in EN ISO 52016-1:2017 with European Annex [92] (later in the text referred to as Annex B), (ii) the calculation procedure defined in EN ISO 52016-1:2017 with Italian Annex [99] (later in the text referred to as Annex A) and (iii) the algorithm implemented in the energy modelling software TRNSYS[7].

3.2.1 EN ISO 52016-1:2017

The calculation algorithm defined by EN ISO 52016-1 [92] provides in output, for each thermal zone and for each hour, the values of parameters such as the internal air temperature, the average internal radiant temperature, and the internal operating temperature useful to evaluate the internal comfort of the environments according to EN ISO 15251 [100]. In addition to temperatures, it also provides the energy needs for heating and cooling, which are essential for the energy assessment of the building. For each heated thermal zone and for each hourly time interval, the standard follows this procedure:

1 in absence of heating and cooling plant the internal operating temperature is evaluated; if this is between the heating and cooling set-point temperature, the system is not switched on and the output power is zero;

2 if the operating temperature is lower/upper than the heating/cooling set-point respectively, the power required by the system to guarantee the defined set-point temperature is calculated;

3 if the power of the system is sufficient, the set-point temperature is guaranteed;

4 if the power of the system is not sufficient, the set-point temperature is not reached;

the node temperatures of all the structures are determined according to the European or National Annex;

the effective energy load for heating and cooling is determined.

This is shown in Figure 3.1.

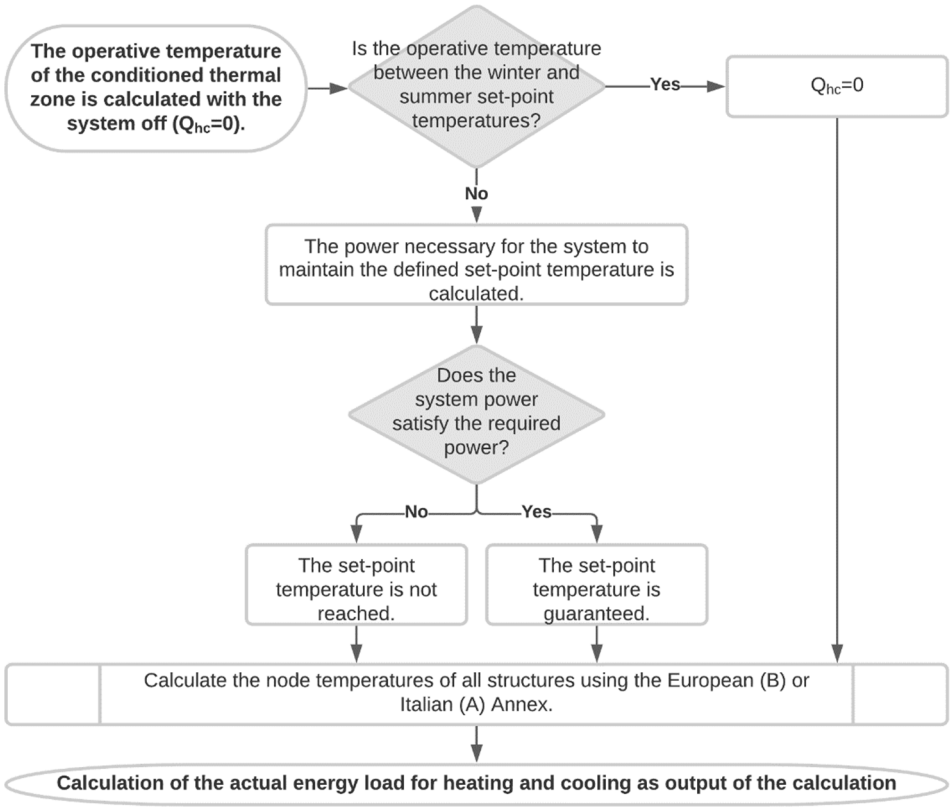

Figure 3.1. Flow chart of the calculation algorithm.

In order to determine the temperatures of the nodes of the structures, the calculation algorithm requires, for each time interval, the resolution of a system of energy balance equations carried out both for each thermal zone and for each individual building elements. The heat balance of the thermal zone provides, for each time interval, the evaluation of (i) the internal thermal capacity, (ii) the convective heat exchanges with the surface nodes of all structures, (iii) the heat exchange by ventilation, (iv) the heat exchange due to thermal bridges and, lastly, (v)

the convective fractions of the total internal contributions, the solar contributions transmitted through the glass surfaces and the contributions due to the load of the heating/cooling plant.
The thermal balances of building elements are evaluated by breaking down each building element (i.e. floors, walls, doors and windows) into a number of capacitive nodes and resistive layers. From the position of the node inside the opaque element, there are three different energy balances:
the balance of the inside-facing node that considers the convective heat exchanges with the inside air, the conductive heat exchanges with the first node inside the opaque element, the heat exchanges by radiation with the surface nodes of all the structures delimiting the thermal zone, the eventual heat capacity associated with the surface node considered and the complementary quotas of the convective fractions of the total internal contributions, the solar contributions transmitted through the glass surfaces and the contributions due to the load of the heating/cooling system.
the energy balances of the nodes inside the opaque element that consider the conductive thermal exchanges with adjacent nodes and any associated thermal capacities of the nodes.
the balance of the outside-facing node, which considers convective heat exchanges with the outside air, radiation heat exchanges with the sky and solar contributions calculated as a function of the solar absorption coefficient, direct and diffuse solar radiation and any shading factor due to external obstacles.
The size of the matrix system is equal to the number of thermal zones plus the number of nodes of all building elements.
The method of EN ISO 52016, based on the electro-thermal analogy, represents the thermo-physical characteristics of building structures with a resistive-capacitive circuit model where the mass is the accumulator (node), the transmittance is the resistive element (layer) and the heat flow is the current. The number of nodes of transparent elements is always 2, while the number of nodes of opaque elements differs according to the European Annex (Annex B) or Italian Annex (Annex A). The differences between the two Annexes are specified below.

3.2.1.1 European Annex

The model for building construction elements in EN ISO 52016–1:2017 is based on a predefined lumped parameters approximation: as shown in Fig. 3.2, the wall RC-network is made of 5 nodes interconnected by four resistances[99].

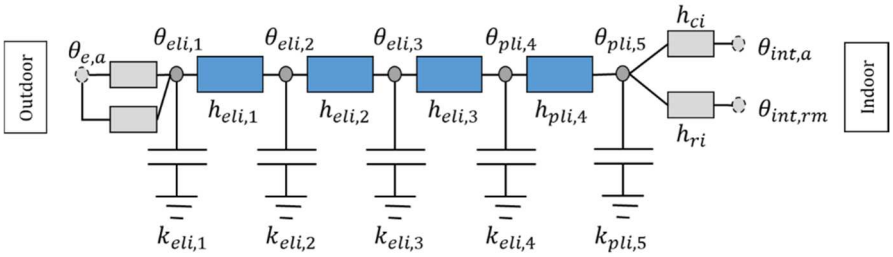

Figure 3.2 RC network of lumped parameters model proposed in EN ISO 52016-1.

Since the position of the nodes is independent of the number and the ther-mal-physical characteristics of each layer, the input parameters necessary for the method are the thermal resistance of the opaque element in m^2K/W and areal heat capacity of the opaque element in J/(m^2K). The conductance between nodes pli and node pli-1 are fixed in function of the thermal resistance of the opaque element, as follows: heli;1 = heli;4 = 6/Rce,eli and heli;2 = heli;3 = 3/ Rce,eli. While the thermal capacity of the element (see Tab.1) is divided to the nodes according to the position of the masses in the construction, namely internal (class I), external (class E), divided between inside and outside (class IE), equally distrib-uted (class D) or inside concentrated (class M). The areal capacity value (κm,eli) can be the actual value, stated in Table A.14 of the EN ISO 52016–1:2017 template, or a predefined value depending on the weight of the wall.

Table 3.1. Values of the thermal capacities of the nodes as a function of the position of the mass, as defined in EN ISO 52016.

Mass Position	κpl1,eli	κpl2,eli	κpl3,eli	κpl4,eli	κpl5,eli
I	0	0	0	0	κm,eli
E	κm,eli	0	0	0	0
IE	κm,eli/2	0	0	0	κm,eli/2
D	κm,eli/8	κm,eli/4	κm,eli/4	κm,eli/4	κm,eli/8
M	0	0	κm,eli	0	0

3.2.1.2 Italian Annex

Concerning the Italian model (Annex A), instead, the number of nodes is not predefined but is calculated for each j-th real layer of the building component, obtaining a number of capacitive nodes equal to the result of the following expression:

$$Ncn,j = \max\{1; (Fo_{ref}/Fo_j)1/2 + 0.999999\} \quad (3.1)$$

where:
Fo_{ref} is the reference Fourier number set to 0.5 [99]
Fo_j is the Fourier number of the j-th layer, calculated as $Foj = \Delta t \cdot \lambda/(\rho j \cdot cj \cdot dj^2)$ [101]

with:
ρj: density of the material of the j-th layer of the building element (kg/m^3)
cj: thermal capacity of the j-th layer of the building element (J/(kg·K))
dj: thickness of the j-th layer of the building element (m)
Once identified the number of nodes in each j-th layer, the internode conductive resistances are assigned using the real thermal conductivity of the material and its relative layer thickness, as shown by Mazzarella et al[99]

3.2.2 Trnsys

TRaNsient SYstems Simulation [7] is the most popular calculation code used by researchers and engineers for the dynamic simulation of complex systems such as building-plant systems. As in this case study, the simulation of a joint building-plant system requires two Trnsys interfaces: SimulationStudio and TRNBuild. Simulation Studio is a virtual environment that allows the study of physical phenomena through blocks called "Type". Among the various types required, "Type 56 - Multizone Building" is the one that enables a multi-zone building to be modelled through the interface called TRNBuild. TRNBuild defines all the thermal zones that compose the building, the opaque and transparent elements, the thermophysical characteristics of the materials, the use profiles of the plants and all the input and output variables necessary to establish the connections between the model and the Simulation Studio environment. Figure 3.3 shows the diagram of the models used for our simulations. The external temperatures, relative humidity and solar radiation used for the two previous methods are given as input.

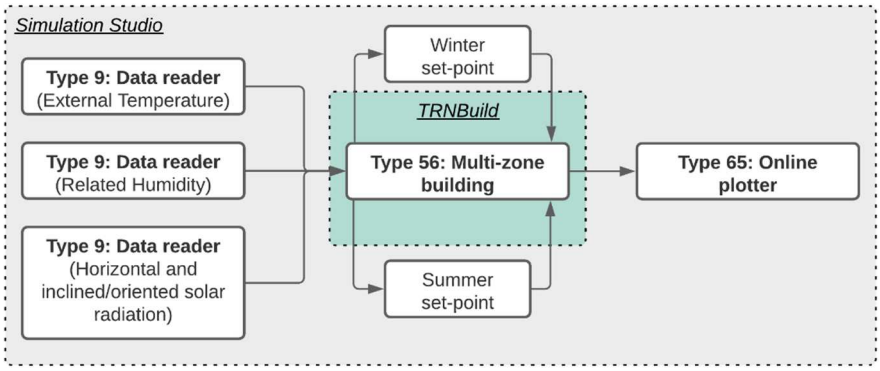

Figure 3.3. Model flowchart in Trnsys.

3.3 Case studies

The study includes three different types of analysis: the first aims to validate Annex A and Annex B of ISO 52016-1:2017 [92], the second aims to evaluate the response of the Standard to impulsive loads (solar radiation) through the variation of the solar transmission coefficient ggl and the third aims to evaluate the impact of the thermo-physical parameters of opaque walls on the calculation of energy needs. In the second analysis, an algorithm is also tested which allows the calculation of solar transmission coefficient as a function of the window orientation and the angle of incidence of solar radiation [102].

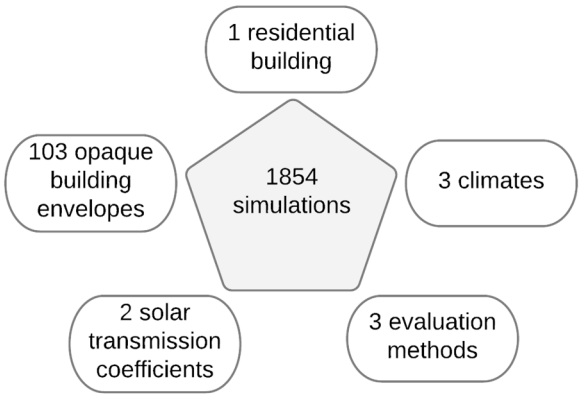

Figure 3.4. Overview of case studies: Evaluation of 3 heat transfer models for buildings with different thermal inertia and different solar transmission coefficients.

3.3.1 Geometry and zoning

The residential case study analysed (see Figure 3.5) is two floors building with a bathroom, a storage room, a kitchen and a living room on the ground floor, and two single rooms, a double room, a bathroom and a hallway on the first floor. EN ISO 52016-1 provides general guidelines for zoning buildings, suggesting that all adjacent spaces in the same category should be grouped together in a single thermal zone. Despite these indications many studies collected by Shin et al [103] show that it is appropriate to divide the space into different thermal zones according to solar loads, orientation, occupancy and air conditioning schedule. Therefore, each room of the building was defined as a different thermal zone. Only the stairwell, unlike the other zones, is classified as an unheated thermal zone. The geometric characteristics of each thermal zone, i.e. the useful surface area (Afloor), the internal volume (V), the average internal height (havg) and the window area (Awindow), are shown in Table 3.2.

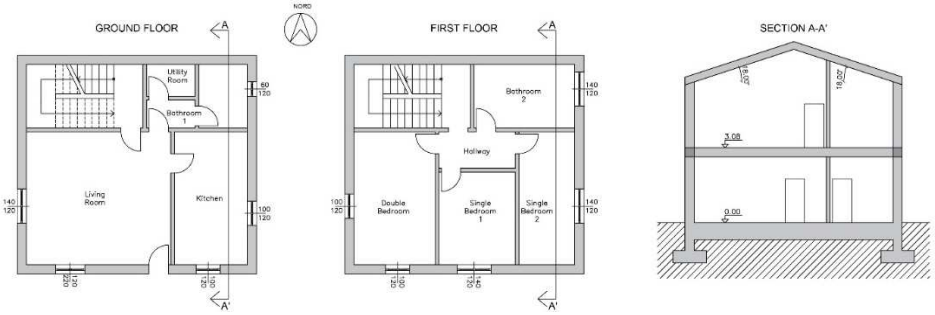

Figure 3.5. Plan view of the ground floor, first floor and section of the building model.

Table 3.2. Geometrical characteristics of thermal zones.

Room	A_{floor}	V	h_{avg}	A_{window}
-	m^2	m^3	m	m^2
Bathroom 1	7.50	20.25	2.70	0.41
Utility Room	2.60	7.02	2.70	0.00
Kitchen	16.35	44.15	2.70	1.64
Living Room	32.43	87.55	2.70	3.25
Bathroom 2	10.79	33.69	3.12	1.22
Hallway	4.73	18.11	3.83	0.00
Single Bedroom 1	11.97	39.71	3.32	1.22
Single Bedroom 2	12.54	43.58	3.48	1.22
Double Bedroom	18.26	63.47	3.48	1.64
Stairwell	12.48	72.66	5.82	0.00

3.3.2 Opaque surfaces

In order to evaluate the effect of the thermophysical characteristics of the opaque vertical envelope and to significantly compare the various simulations, it was decided to keep some opaque structures constant, such as: ground slab, inter-floor slab, roof and internal walls. In addition to the thermo-physical characteristics of the listed structures, Tab.3.3 also reports information on the distribution of mass within the opaque element, which is a necessary information for the purpose of applying Annex B of the EN ISO 52016-1: 2017 standard [92].

Table 3.3. Thermo-physical characteristics of fixed structures. I: mass concentrated on the internal side. D: distributed mass.

Building Element	Distribution of Mass	U	M_s	Y_{IE}	fa	φ	κ_j
-	-	W/(m²K)	kg/m²	W/(m²K)	-	h	kJ/(m²K)
Roof	I	0.264	401.60	0.061	0.230	7.66	91.41
Ground Floor	D	0.353	1369.40	0.010	0.028	18.08	62.15
Interior Floor	D	0.354	403.80	0.039	0.111	12.28	52.20
Interior Walls	D	1.125	111.60	0.673	0.598	6.18	50.99

One hundred and three different vertical opaque envelopes were simulated, each characterized by different values of thermal transmittance, surface mass, periodic thermal transmittance and internal areal heat capacity. Among these walls, according to the classification reported in the Standard, 16 have a mass divided between internal and external (EI), 23 have a concentrated mass on the external side (E), 24 have a concentrated mass on the internal side (I) and 40 have a distributed mass (D). The 103 walls studied include the following technological solutions: single-layer masonry in thermo-brick, multi-layer masonry with cavity insulation, masonry with external insulation, masonry with internal insulation, light wood and plaster fiber walls. Tab.3.4 shows the ranges of the thermo-physical parameters of the analysed walls, while in Table A.1 in Appendix A gives detail.

Table 3.4. Range of thermo-physical parameters of the walls analysed.

Parameter	Min	Max
U [W/(m²K)]	0.163	0.598
M_s [kg/m²]	18.60	444.15
Y_{IE} [W/(m²K)]	0.001	0.339
f_a [-]	0.003	0.953
φ [h]	2.05	32.77
κ_j [kJ/(m²K)]	21.56	50.13

3.3.3 Transparent surfaces

The glazed structures were sized (see Tab.3.5) taking the minimum surface value obtained between the calculation of the daylight factor (at least 2%) and the calculation of 1/8 of the usable floor area of each thermal zone. These two limits are given in the Italian Ministerial Decree of 05/07/1975 [104] while the calculation of the daylight factor was carried out according to the UNI 10840:2007 standard [105]. In order to evaluate the management of

impulsive loads by the calculation algorithm reported in EN ISO 52016-1:2017[92], it was decided to consider two solar transmission coefficients: ggl,n = 0.77 (case study 1) and ggl,n = 0.34 (case study 2). In no case fixed or movable shading systems are considered, therefore only the influence of ggl on the calculation of the energy demand is evaluated.

Table 3.5. Thermal transmittance and solar transmission coefficient of windows used.

b_{window}	h_{window}	$U_{case\ study\ 1\ =\ case\ study\ 2}$	$g_{gl,n,case\ study\ 1}$	$g_{gl,n,case\ study\ 2}$
m	m	W/(m²K)	-	-
0.60	1.20	2.00	0.77	0.34
1.00	1.20	2.19	0.77	0.34
1.40	1.20	2.27	0.77	0.34
1.20	2.20	2.34	0.77	0.34

Considering an average thickness of all the walls used of 36 cm, the ratio of glazed to opaque surfaces is: 0% in the North, 11.1% in the South, 8.6% in the East and 4.7% in the West.

3.3.4 Climate and other assumptions

The energy needs for heating and cooling were calculated for a typical meteorological year for three Italian climatic zones identified in DPR 412/1993 [106]: Milan, Rome and Palermo. Hourly climatic data defined in national databases were used for each location (see Tab.3.6).

Table 3.6. Outdoor temperature (min, max and average), horizontal solar radiation (max and verage) and heating degree days of the three considered locations.

Site	$\theta_{e,min}$	$\theta_{e,max}$	$\theta_{e,avg}$	$I_{H,max}$	$I_{H,avg}$	HDD	Köppen-classification
-	°C	°C	°C	W/m²	W/m²	-	-
Milan	-1.80	33.70	14.29	1000.00	150.27	2274	Cfa
Rome	-0.12	37.38	16.72	968.90	180.81	1630	Csa
Palermo	0.21	36.91	18.99	986.10	181.08	1089	Csa

For the calculation of direct and diffuse radiation on horizontal and inclined/oriented surfaces, EN ISO 52016-1:2017[92] refers to EN ISO 52010-1:2017 [6], which allows the use of different calculation models. In this study, the calculation method proposed in [16] is used. This method, in a comparative analysis on five European cities and for four calculation algorithms (Trnsys [7], Meteonorm [8], EN ISO 52010-1:2017 [6] and the proposed method) returns values closer to those calculated with Trnsys. The UNI-TS 11300-1: 2014 [107] standard was used to determine the internal gains, where, for useful surfaces of residential

buildings greater than 120 m^2, the value of the internal contributions is set at 450 W. Dividing this value by the useful surface of each thermal zone, the thermal inputs for each room are obtained. These contributions are considered constant throughout the calculation period. Moreover, a constant natural ventilation was considered, using an air exchange rate of 0.50 1 / h.
For the winter season the set-point temperature was set at 20°C, and for the summer season at 26°C. The switch-on profile of the systems is constant for each location. The heating system is switched on for 12 hours a day, from 7:00 AM to 11:00 AM and from 4:00 PM to 10:00 PM, while the cooling system is switched on for 8 hours a day, from 11:00 AM to 6:00 PM, both from 1 January to 31 December with infinite power .
In this study, thermal bridges and shading caused by external elements or curtains were not considered, while the heat exchange with the ground is considered adiabatic. In particular, the choice not to consider shading has allowed to highlight better the inci-dence of the total solar energy transmission coefficient (ggl) on the method of EN ISO 52016, avoiding having energy requirements "forcedly" aligned with Trnsys due to absent solar gains.

3.4 Results and discussion

The following metrics were used to assess the accuracy of the Standard (European and Italian annexes) compared to Trnsys:
CV(RMSE) (Coefficient of Variation of the Root Mean Square Error) is used to calibrate models in measured building performance. This metric indicates instability in the observed relationship between variables in the baseline period. It is the coefficient of the variation of the predicted input series relative to the observed input series (Trnsys).
According to ASHRAE guideline 14 [108], an hourly energy model is considered accurate if the CV(RMSE) value is less than 30%.

$$\text{CV(RMSE)} = \sqrt{(\sum_{i=1}^{n}(T_i - M_i)^2/n)}/\,\bar{T} \cdot 100\ [\%] \tag{3.2}$$

where Ti and Mi are respectively the hourly data from Trnsys and the hourly data from the other methods used, n is the number of hours in which Trnsys gives a non-zero value in the considered interval (heating or cooling hours) and $\bar{T}$ is the average of the hourly data from Trnsys.

RMSE (Root Mean Square Error) is the standard deviation of the residuals (prediction errors). The effect of each error on RMSE is proportional to the size of the squared error; thus, larger errors have a disproportionately large effect on RMSE. Consequently, RMSE is sensitive to outliers [26,27].

$$\text{RMSE} = \sqrt{(\sum_{i=1}^{n}(T_i - M_i)^2/n)} \text{ [kWh or °C]} \quad (3.3)$$

3.4.1 Accuracy of the Standard (European and Italian Annex)

Analysing as a case study the building defined in Pragraph 3.3, with ggl=Fw·ggl,n=0.9·0.77=0.693, the results obtained with Annex B and Italian Annex A are compared with Trnsys. Considering the maximum annual heating, cooling and total demand of 61.4 kWh/m^2, 34.1 kWh/m^2 and 75.8 kWh/m^2, and a minimum annual heating, cooling and total demand of 2.9 kWh/m^2, 11.4 kWh/m^2 and 30.9 kWh/m^2, the building in all its configurations and locations can be categorised as a low energy building [111]. For each city in the case study, the RMSE is extremely small. Regarding heating, both methods show variations of less than 1 kWh, and for cooling variations of less than 2 kWh. Furthermore, unlike heating where the RMSE seems to vary as a function of the annual hourly needs, in the cooling phase the error seems to be less dependent on the energy needs (see Figure 3.6). While the absolute error RMSE is low, the relative error CV(RMSE) is often above the ASHRAE limit of 30%. However, it should be noted that this is predominantly caused by the low energy needs of the analysed solutions, which affect the denominator of Eq. 3.2, increasing the relative error. From Figure 3.7, in the heating period, the error increases to 98% for the city with the warmest climate and decreases to 23% for the city with the coldest climate. Conversely, in the cooling period the error reaches a maximum of 150% for the coldest city and a minimum of 35% for the warmest city. Only in the winter phase there are cases where the CV(RMSE) is less than 30%, precisely 16 cases (5.2%) for Annex B and 45 cases (14.6%) for Annex A. Although these percentages are low, considering the small number of kWh/m^2 consumed by the building, they are consistent with those obtained from the Zakula et al. study [98].

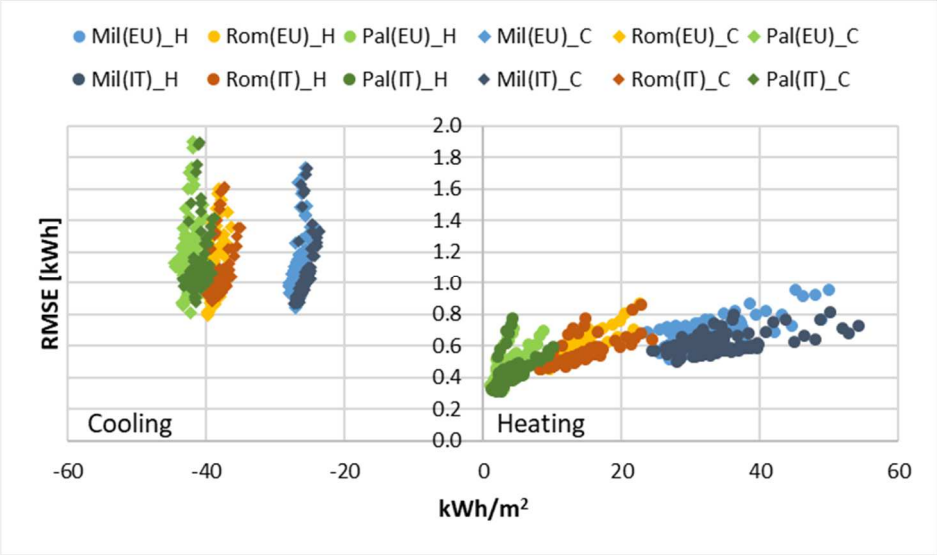

Figure 3.6. RMSE for heating and cooling needs, for all climates of the case study and for both methods (EU: Annex B, IT: Annex A): Case study with ggl,n=0.77.

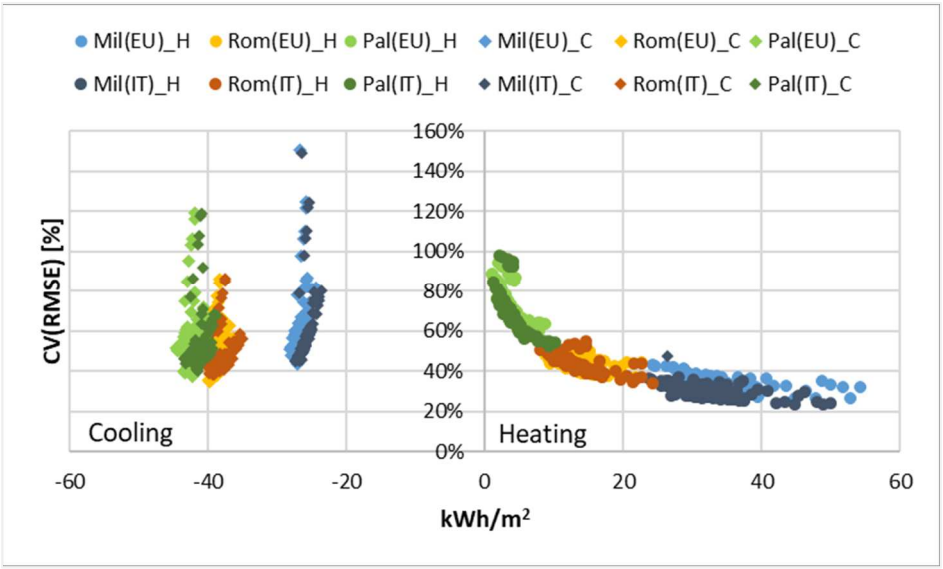

Figure 3.7. CV(RMSE) for heating and cooling needs, for all climates of the case study and for both methods (EU: Annex B, IT: Annex A): Case study with ggl,n=0.77.

Table 3.7. Minimum, maximum, average, and standard deviation value of CV(RMSE) and the RMSE of both methods of EN ISO 52016 (Annex A and Annex B). The gray cells show the best percentages.

	Heating				Cooling			
	CV(RMSE) [%]		RMSE [kWh]		CV(RMSE) [%]		RMSE [kWh]	
	EU	IT	EU	IT	EU	IT	EU	IT
Min	26.2%	23.4%	0.32	0.31	34.6%	38.3%	0.80	0.87
Max	94.0%	98.0%	0.95	0.86	150.5%	149.0%	1.90	1.90
Avg	51.8%	48.4%	0.57	0.53	56.4%	53.3%	1.14	1.07
Dev.St.	18.6%	18.2%	0.12	0.11	14.9%	14.8%	0.19	0.18

In order to evaluate the differences in terms of internal temperatures and surface temperatures, we studied four different envelope configurations on a single thermal zone of the building. Taking the living room, that is the largest room and with the most glazed area, as the reference thermal zone (see Figure 3.8) we compared the internal temperatures and surface temperatures (points 1 to 10) of four layers with the same thermal transmittance but different mass positions (see Tab.3.8). Walls 21, 75 and 87 (see Tab.3.8) have respectively distributed mass, internal mass (external insulation) and external mass (internal insulation), while 44 is a low surface mass wall. RMSE is calculated between the temperatures obtained from Trnsys and those obtained from models described in the European and Italian annexes.

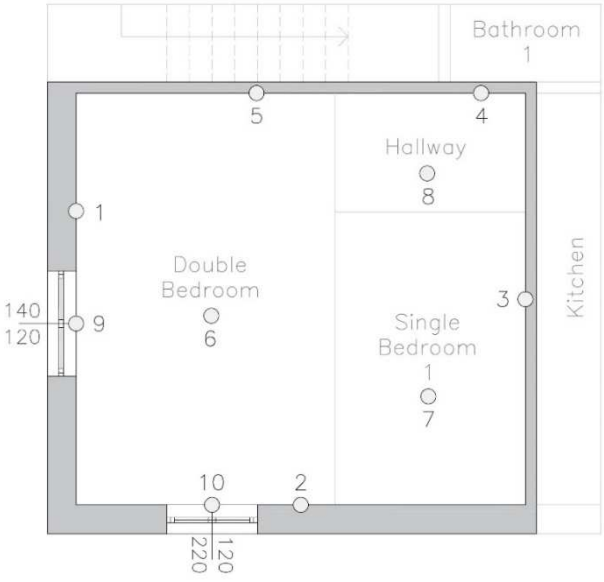

Figure 3.8. Indication of the points on which the surface temperatures of the living room are calculated

Table 3.8. Selected structures, among those analysed, with similar transmittance but different surface mass and mass distribution.

N.	Distribution of Mass	U	M_s	Y_{IE}	f_a	φ	κ_j
-	-	W/(m²K)	kg/m²	W/(m²K)	-	h	kJ/(m²K)
21	D	0.23	432	0.001	0.005	5.93	39.57
75	I	0.23	405	0.001	0.005	26.85	41.52
87	E	0.23	405	0.001	0.006	2.53	22.33
44	IE	0.23	21	0.192	0.888	3.81	34.26

The results in Figure 3.9, show that the use of Annex B leads to a greater error in terms of temperatures than the use of Annex A. In addition, it is important to note that the surface temperatures of the external walls (1 and 2) calculated with Annex A have an approximately constant error (about 0.4°C) for all four stratigraphies analysed, when compared to Trnsys. In contrast, for annex B the error seems to vary according to the position of the mass inside the wall; obtaining the worst result for wall 87, that is characterized by external mass and internal insulation. This error affects the entire thermal zone by modifying the surface temperatures of the internal walls (3, 4 and 5) and the floor (6, 7 and 8) (see Figure 3.9). Also with regard to the operative, air and average radiant temperatures, the smallest error is obtained with Annex A.

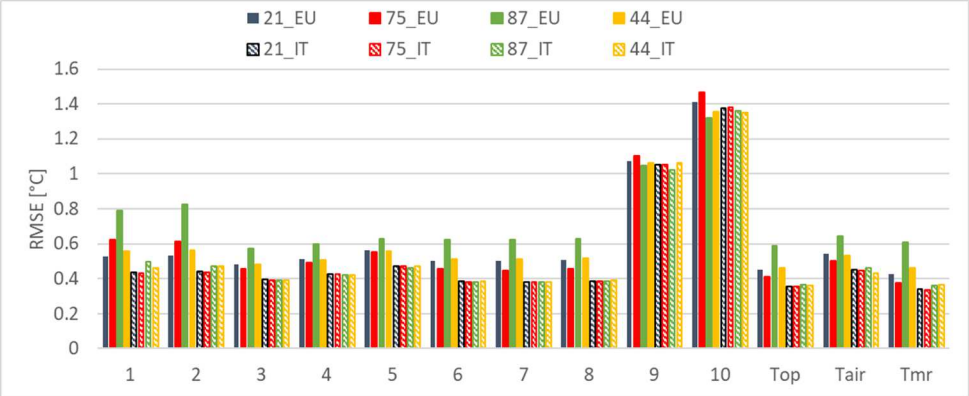

Figure 3.9. RMSE [°C] calculated for indoor and surface temperatures in the living room. (EU: Annex B, IT: Annex A)

3.4.2 Impact of the solar transmission coefficient (ggl) on the calculation of energy needs

Considering as case study the building defined in Paragraph 3.3, with ggl=Fw·ggl,n=0.9·0.34=0.306, the results obtained with Annex B and Italian Annex A are compared with Trnsys. In this configuration, the maximum annual heating, cooling and total demand is 72.3 kWh/m^2, 14.3 kWh/m^2 and 76.8 kWh/m^2 and the minimum annual heating, cooling and total demand is 9.1 kWh/m^2, 2.2 kWh/m^2 and 22.5 kWh/m^2. Decreasing the solar transmission coefficient by 44% (from 0.77 to 0.34), leads to an increase in the heating demand and a decrease in the cooling demand (see Tab.3.9). For all three climates, however, total energy demand decreases by 3.7%, 16.4% and 28.4% for Milan, Rome and Palermo, respectively.

Table 3.9. Average percentage difference (a) and average energy difference (b) between the case study with ggl,n=0.77 and ggl,n=0.34. Δφ%= (φ_ggl,0.77- φ_ggl,0.34)/ φ_ggl,0.77. ΔkWh= (φ_ggl,0.77- φ_ggl,0.34).

	Δφ,h [%]	**Δφ,c [%]**	**Δφ,tot [%]**
Milan	-26.4%	68.3%	3.7%
Rome	-61.2%	61.0%	16.4%
Palermo	-126.0%	59.3%	28.4%

a)

	Δφ,h [kWh]	**Δφ,c [kWh]**	**Δφ,tot [kWh]**
Milan	-1193.0	1427.5	234.5
Rome	-1191.4	2069.5	878.1
Palermo	-876.9	2106.0	1229.2

b)

As in the case study with ggl,n =0.77, the RMSE is extremely small (see Figure 3.10). For heating, both methods show variations of less than 1 kWh, while for cooling the variations are greater than in the previous case study but still not more than 2.2 kWh. While the absolute error (RMSE) is low, the relative error CV(RMSE) is often above the ASHRAE limit of 30%. As already mentioned, this is mainly due to the low energy requirements of the analysed solutions, which affect the denominator of Eq. 3.2, increasing the relative error. In fact, from Figure 3.11, during the heating phase, the error increases to 71% for the city with the warmest climate and decreases to 24% for the city with the coldest climate. Conversely, in the cooling phase the error reaches a maximum of 366% for the coldest city and a minimum of 62% for the warmest city. Only in winter some cases are characterized by the CV(RMSE) smaller than 30%, precisely 51 cases (16.5%) for Annex B and 81 cases (26.2%) for Annex A. With a lower solar transmittance coefficient, hence less incoming solar contributions, both models seem to perform better in terms of CV(RMSE) in the winter period, but only for the cooler city, while in the summer period no case satisfies the ASHRAE limit of 30%.

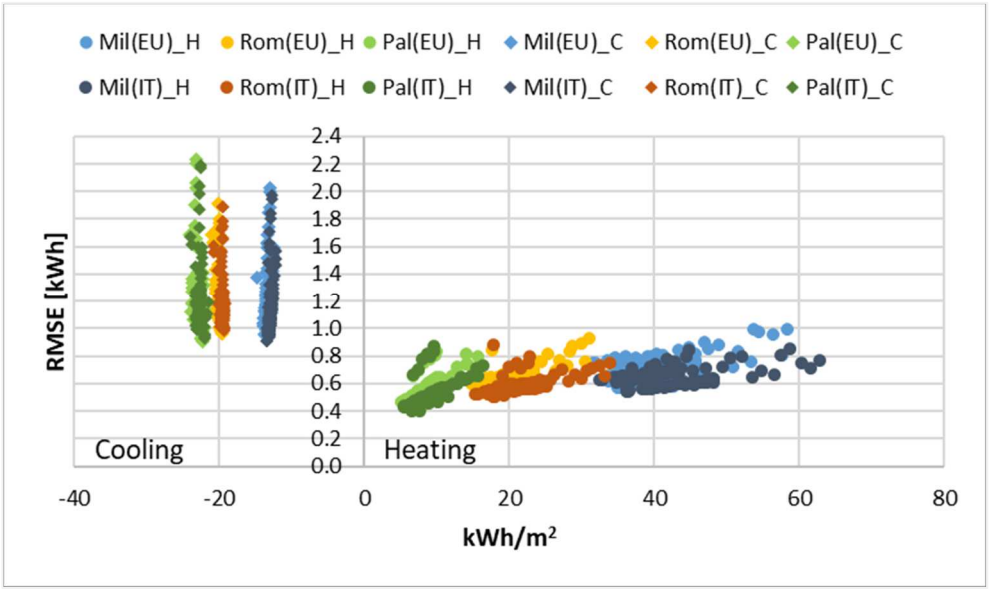

Figure 3.10. RMSE for heating and cooling needs, for all climates of the case study and for both methods (EU: Annex B, IT: Annex A): Case study with ggl,n=0.34.

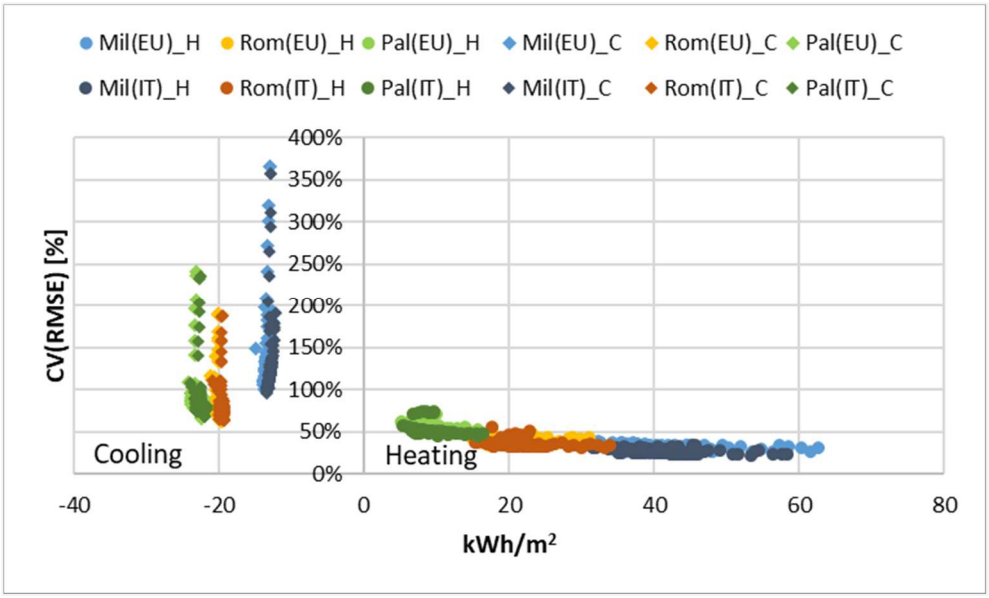

Figure 3.11. CV(RMSE) for heating and cooling needs, for all climates of the case study and for both methods (EU: Annex B, IT: Annex A): Case study with ggl,n=0.34.

Comparing the two methods, from Tab.3.10, the variable node method described in the Italian Annex A is closer to the results reported by Trnsys. Despite the greater number of structures that verify the relative error of 30%, decreasing the ggl,n leads to a worse RMSE absolute error than the case study with ggl,n = 0.77. In fact, in the winter season the average error is 12.9% and 11.6% worse for the method described in Annex B and Annex A respectively, while in the summer season it is 9.3% and 11.7% worse.

Table 3.10. Minimum, maximum, average, and standard deviation value of CV(RMSE) and the RMSE of both methods of EN ISO 52016 (Annex A and Annex B). The gray cells show the best percentages.

	Heating				Cooling			
	CV(RMSE) [%]		RMSE [kWh]		CV(RMSE) [%]		RMSE [kWh]	
	EU	IT	EU	IT	EU	IT	EU	IT
Min	24.1%	22.4%	0.41	0.40	62.0%	63.1%	0.91	0.91
Max	70.7%	74.5%	0.99	0.88	366.0%	356.6%	2.23	2.19
Avg	41.6%	38.5%	0.64	0.59	106.4%	102.6%	1.24	1.20
Dev.St.	11.0%	11.3%	0.11	0.09	43.4%	42.2%	0.23	0.23

3.4.2.1 Improved calculation of the total solar energy transmission coefficient (ggl)

As pointed out by Zakula et al. [10,11], while TRNSYS uses a relatively complex mathematical model for the calculation of the total solar energy transmission coefficient (ggl) of the window, ISO 52016-1 uses very simplified correction factors (i.e. Fw=0.9), although it considers the angle of incidence of solar radiation. This difference between the two calculation methods inevitably leads to the estimation of different solar contributions and energy needs, especially for the summer period. For this reason, in this analysis the algorithm of Karlsson et al. [102], also reported in the Italian National Annex, is tested, which allows to calculate the ggl coefficient as a function of a variable Fw coefficient:

$$Fw = \frac{(\mathrm{Fw,dif} \cdot \mathrm{Isol,dif,t} + \mathrm{Fw,dir} \cdot \mathrm{Isol,dir,t} \cdot \mathrm{Fsh,obst,t})}{(\mathrm{Isol,dif,t} + \mathrm{Isol,dir,t} \cdot \mathrm{Fsh,obst,t})} \tag{3.4}$$

where Fw,dir is the correction factor for direct radiation, Fw,dif is the correction factor for diffuse radiation equal to 0.8, Isol,dir,t e Isol,dif,t is the direct and diffuse solar radiation incident on the glazed surface and Fsh,obst,t is the shading reduction factor for external obstacles calculated in accordance with Annex E.

$$Fw, dir = 1 - 8 \cdot \frac{\vartheta \mathrm{sol,t}}{90} \cdot 5.2 + 0.7q - \frac{0.25}{q} \cdot \frac{\vartheta \mathrm{sol,t}}{90} \cdot 2 + \\ + \left(7 + \frac{0.25}{q}\right) \cdot \frac{\vartheta \mathrm{sol,t}}{90} \cdot [(5.26 + 0.06\mathrm{p}) + (0.73 + 0.04\mathrm{p})q] \quad (3.5)$$

where ϑsol,t is the angle of incidence of direct solar radiation in degrees, p is the number of glass panels and q is the coefficient indicating the type of glass coating. The solar loads of the living room are calculated using the Fw coefficient of 0.9 (as suggested by Standars) and the variable Fw coefficient as shown in equations 3.4 and 3.5; these loads are then compared with those of Trnsys.

From this analysis we observe that the variable Fw method allows summer solar loads to be more closely aligned with Trnsys loads, but the problem persists in the winter phase. The annual CV(RMSE) calculated for the method with ggl,cost and ggl,var is 33.54% and 28.95%, respectively. In particular, as can be observed in Tab.3.11, in spring and summer the difference between the two CV(RMSE) is about 14% and between the two RMSE is about 40%, with the best results obtained for the proposed method (ggl,var). In autumn and winter, the difference between the two CV(RMSE) is about 7% and between the two RMSE is less than 20%, with the best results obtained for the method with ggl,cost. Despite the fact that in the cold seasons the proposed method seems to perform worse, the solar gains being lower than in the summer, have less impact on the heating needs. Conversely, as already observed in paragraphs 4.1 and 4.2, the error obtained on the calculation of the cooling requirement is extremely greater than that of heating and, as emerges in the literature, is mainly caused by solar loads [112–115].

Table 3.11. Seasonal CV(RMSE)[%] and RMSE[kWh] calculated for the ggl,cost and ggl,var method

	Spring		**Summer**		**Autumn**		**Winter**	
	21/03 - 21/06		**22/06 - 22/09**		**23/09 - 21/12**		**22/12 - 20/03**	
	CV(RMSE)	**RMSE**	**CV(RMSE)**	**RMSE**	**CV(RMSE)**	**RMSE**	**CV(RMSE)**	**RMSE**
$g_{gl,cost}$	33.29%	73.97	32.05%	76.78	33.59%	62.05	34.99%	58.47
$g_{gl,var}$	19.20%	42.66	17.26%	41.35	39.62%	73.21	43.10%	72.03

Thus, implementing the Karlsson et al. method [102] within the general algorithm of EN ISO 52016-1[92] will allow the estimation of more accurate solar loads and consequently more precise summer energy demand.

3.4.3 Sensitivity analysis of the thermophysical parameters of opaque walls on the calculation of energy needs

Performing a sensitivity analysis is important in order to check the robustness of the conclusions of a study. This analysis allows to examine how the output results of the models used (i.e. heating or cooling energy needs) are influenced by the values of the input variables (i.e. the thermophysical parameters of the opaque elements).
Using the "Weight by Correlation" operator of the RapidMiner Studio software [116], the absolute values of the attribute weights (i.e. thermophysical parameters of opaque elements) were calculated with respect to the label attribute (i.e heating or cooling energy needs). Values close to 1 will indicate a high correlation between the parameters, while values close to zero will indicate a low correlation. The weights obtained from the analysis of the models described in Annex A and B of EN ISO 52016-1 were compared with those obtained with the Trnsys software.
The dataset was divided by city and by case study (ggl,n=0.77 and ggl,n=0.34) and 6 different analyses were conducted. The specific values of the weights calculated by correlation are given in Appendix A.2 of this manuscript.
In the heating season, for both ggl configurations (see Figure 3.12 and Figure 3.13) and for all calculation models (Annex A, Annex B and Trnsys), the stationary thermal transmittance (U) is the most important parameter. The periodic thermal transmittance (Yie), the phase shift (phi), the total thermal capacity (Ctot), the surface mass (Ms), the attenuation (fa) and lastly the internal heat capacity (ki) follow in descending order. This means that the different models are well aligned during heating.

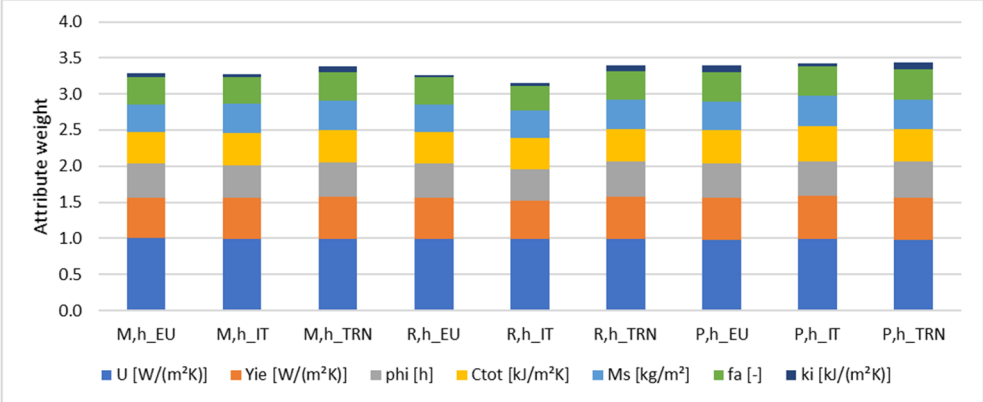

Figure 3.12. Weight analysis of the thermo-physical attributes of opaque structures, for the winter period and with ggl,n=0.77.

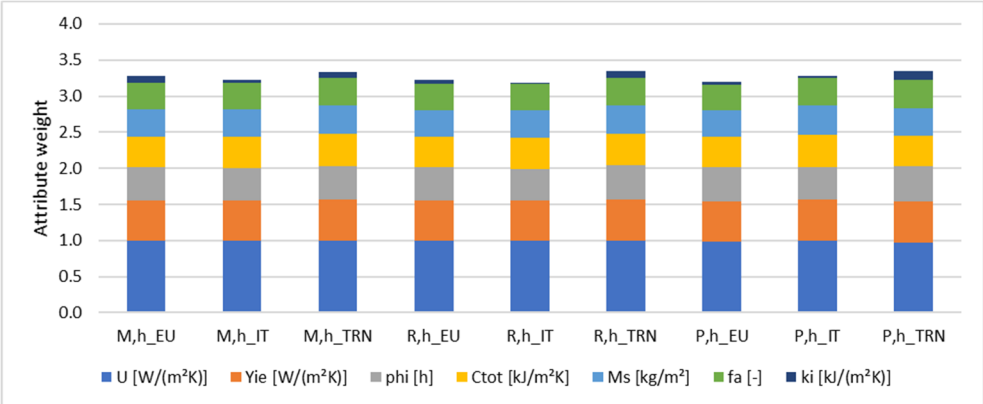

Figure 3.13. Weight analysis of the thermo-physical attributes of opaque structures, for the winter period and with ggl,n=0.34.

In the cooling season, the weights of the attributes turn out to be very variable for the different methods and case studies. In Figure 3.14, for the case study with ggl,n=0.77, the thermal transmittance is still the most important attribute, although with a weight of 17.4% lower than the winter one. Then, for Trnsys, in descending order, the phase shift (phi), the periodic thermal transmittance (Yie), the internal heat capacity (ki), the total heat capacity (Ctot), the surface mass (Ms) and finally the attenuation (fa) follow. Although there is a similarity in terms of weights, Annex A and Annex B tend to underestimate some parameters such as internal heat capacity by about 93% and 81%, attenuation by 85% and 86% and surface mass by 62% and 70%, especially in warmer climates such as Palermo.

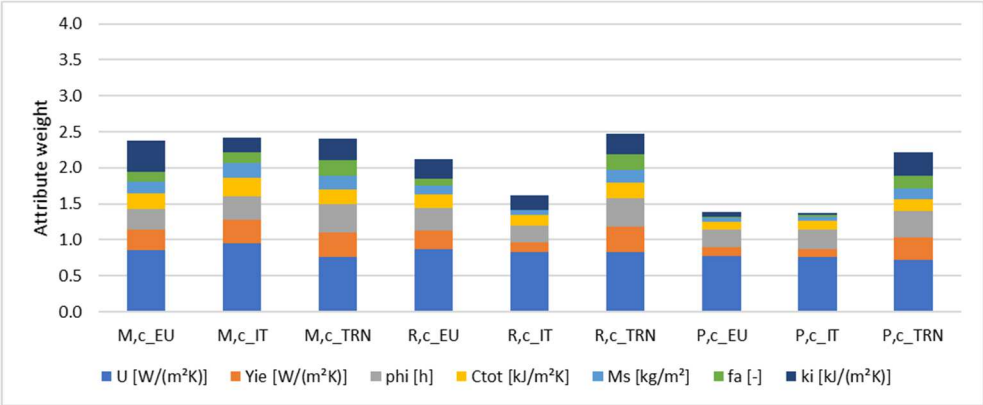

Figure 3.14. Weight analysis of the thermo-physical attributes of opaque structures, for the summer period and with ggl,n=0.77.

The weights of the attributes calculated by Annex A and Annex B seem to have no more correspondence with the weights calculated by Trnsys if the solar transmission coefficient is

set to 0.34. From Figure 3.15 it can be observed that the thermal transmittance, except for the city of Milan, is underestimated by both Annexes of EN ISO 52016-1. This leads to state that for particularly energy efficient structures in the summer period, where there is a strong dynamism of the boundary conditions, the method of EN ISO 52016-1 fails to correctly evaluate the weight of some parameters.

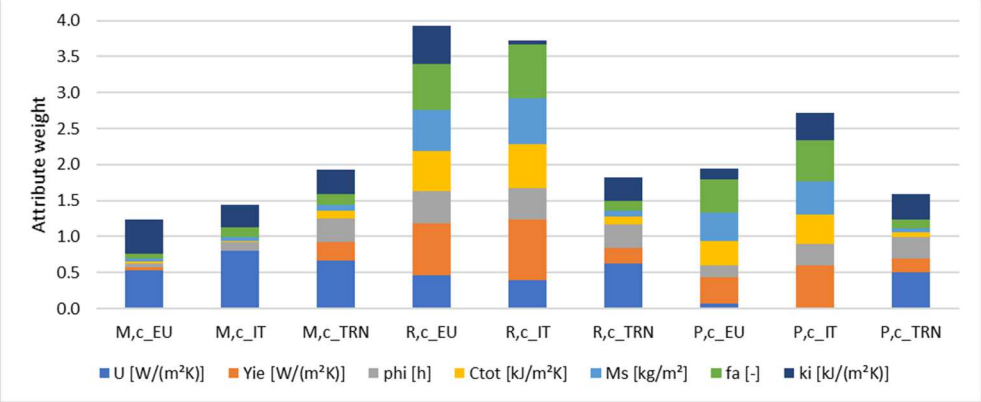

Figure 3.15. Weight analysis of the thermo-physical attributes of opaque structures, for the summer period and with ggl,n=0.34.

3.5 Conclusion

A total of 1854 cases were analysed using three different calculation methods, including the combination of 103 different stratigraphies, three climate zones and two solar transmission coefficients. These combinations produce low energy building solutions. Comparison between Trnsys results and those obtained from the two annexes of EN ISO 52016-1 showed that:

- The absolute error RMSE is extremely small. Both methods show variations of less than 1 kWh for heating, while for cooling the variations are less than 2 kWh (in the case of ggl,n=0.77) and less than 2.2 kWh (in the case of ggl,n=0.34). In absolute terms, Annex A performs better. This result is congruent with the comparative analysis carried out by Mazzarella et al.[99] between the two models of the Annexes and the analytical solution with sinusoidal boundary conditions. In all the test cases, the results obtained applying the Italian Annex provide better results, with a reduction of the error on the internal flow amplitude between 14% and 67% and an overestimation of the external flow amplitude compared to the analytical solution of 3%.
- The relative error CV(RMSE) is often over the 30% ASHRAE limit. It should be noted, however, that this is mainly caused by the low energy requirements of the analysed solutions, which affect the denominator of the relative error formula. Only in the winter phase

and for the coldest city the CV(RMSE) is verified. Specifically, for the case study with ggl,n=0.77 the verification is satisfied for 16 cases (5.2%) with Annex B and for 45 cases (14.6%) with Annex A, while for the case study with ggl,n=0.34, 51 cases (16.5%) with Annex B and 81 cases (26.2%) with Annex A. The contrast between the excellent results obtained in terms of RMSE and the low percentage of cases that satisfy the limit of 30% in terms of CV (RMSE) leads us to affirm that the verification proposed by ASHRAE to validate dynamic calculation methods, does not it is fully adequate in the case of low-energy buildings.

- In general, decreasing the ggl (thus increasing the performance of the glazed structures) produces a higher RMSE. Indeed, a worse average error of 12.9% and 11.6% is obtained in the winter season for the method described in Annex B and Annex A, respectively, while 9.3% and 11.7% in the summer season. These results suggest that the EN ISO 52016-1 algorithm, regardless of the annex used, has an accuracy inversely proportional to the performance of the building: the lower the consumption, the greater the error committed with respect to the energy needs calculated by Trnsys.

- In terms of internal and surface temperatures, the RMSE of Annex B compared to Trnsys seems to vary according to the positioning of the mass inside the wall, with the worst result for the wall with external mass. For Annex A, the RMSE is approximately constant for each proposed solution. This allows us to state that the heat transfer model of the opaque elements proposed in the European Annex (Annex B) favors some masonry types over others, in particular the one with distributed thermal mass. Overestimating the surface temperatures of the thermal zones implies an incorrect calculation of the operating temperature and consequently an incorrect energy requirement.

- Through a sensitivity analysis of the thermo-physical parameters of the walls, it can be stated that in the heating period the different calculation models are particularly aligned. In the summer period, on the other hand, the weights of the contributions are very variable for the different methods and the different case studies. In particular, for solar transmission coefficient equal to 0.34, the weights of the attributes calculated by Annex A and Annex B seem to have no correspondence with the weights calculated by Trnsys.

- Although ISO 52016-1 considers the angle of incidence of solar radiation, it overlooks that ggl can vary considerably depending on the time of day and the day of the year. Implementing the Karlsson et al. method [102] within the general algorithm allows to improve the RMSE of summer solar loads by 46.7% compared to the method proposed by the standard. Improving the estimation of solar loads let an improvement in the calculation of summer needs.

In conclusion, it can be stated that the method proposed in the Italian national annex and the Karlsson method for the calculation of solar contributions are represent an improvement on the current EN ISO 52016-1. Future work will focus on the comparative analysis of the

methods described in the two Annexes of EN ISO 52016-1 and the measurements collected in the field through an experimental mock-up.

Chapter 4.
Conversion of climatic data for energy calculations

4.1 Introduction

The dynamic model of EN ISO 52016-1 allows in-depth investigation of the energy performance of buildings by requiring a limited number of input data. Some of these data, however, such as climate data, must be provided on an hourly basis. Although climate datasets are available, they are unable to provide all the information needed for a dynamic simulation, such as global, direct and diffuse irradiances on inclined and oriented surfaces. In order to overcome this limitation, EN ISO 52010-1:2017 (International Organization for Standardization, 2017b) specifies a procedure to calculate direct and diffuse irradiance on all tilted and oriented surfaces from global irradiance on horizontal plane.

An accurate assessment of incident radiations on envelope surfaces is of utmost importance to correctly calculate solar gains, since they significantly influence summer cooling demands, particularly of highly glazed buildings located in hot climate zones [117][118][119]. In fact, even if there are solutions to control solar gains, such as low-emission [120][121] or reflective [122] glass, they do not exempt from providing correct data inputs in order to obtain a simulation of the building as close as possible to the real behavior.

Currently, ground-based radiometry is the most reliable method for obtaining data for solar irradiances, and the main mathematical models to predict solar diffuse irradiance on horizontal and inclined surfaces have been developed from its measurements. Nevertheless, due to some problems (e.g., instruments calibration, data quality control or missing data [123]), ground-based radiometry is affected by measurement errors and hence the use of these data may impact on the accuracy of the resulting models. In fact, the use of the model included in EN ISO 52010-1:2017 in some cases may result in an inaccurate estimation of the diffuse irradiance on the horizontal plane and of the direct irradiance on the vertical surfaces.

In the present chapter we define a calculation procedure that may be considered as alternative to the one described in EN ISO 52010-1:2017[6]. The proposed procedure represents a revised version of UNI 10349-1:2016[124] and allows to perform splitting between direct and diffuse irradiance on tilted and oriented surfaces by using global irradiance on horizontal plane as input.

4.2 Description of the calculation procedure

The proposed calculation procedure takes as input the hourly global irradiance on the horizontal plane and returns the direct and diffuse fractions on any surface. It consists of several steps, as depicted in Figure 4.1. The procedure represents an improvement of the hourly method described in the Annex A of the national UNI 10349-1:2016 [124], in particular for what concerns the estimation of both the angle of solar incidence and the direct irradiance on tilted and oriented surfaces.

Figure 4.1. Description of the calculation procedure

4.2.1 Calculation of the sun path

In order to apply this method, the geographical parameters of the location (i.e., latitude (φw), longitude (λw) and altitude (H)), climate data (i.e. global solar irradiance (Gsol;g), ground solar reflectivity (ρsol;grnd)), and surface position data (i.e. inclination (βic) and azimuth (γic)), must be used as input (reference values indicated in Table 4.1).

	Horizontal surface	Tilted surface			
Orientation	-	South	East	West	North
βic	0°	90°			
γic	0°	0°	-90°	90°	±180°

Table 4.1. Angle convention for surface azimuth (γic).

The first step of the proposed methodology is the calculation of the sun path. The solar declination δ [125] in degrees is:

$$\delta = \frac{360^\circ}{2\pi} \cdot [0.006918 - 0.399912 \cdot \cos R_{dc} + 0.070257 \cdot \sin R_{dc} - 0.006758 \cdot \cos 2R_{dc} + 0.000907 \cdot \sin 2R_{dc} - 0.002697 \cdot \cos 3R_{dc} + 0.00148 \cdot \sin 3R_{dc}] \quad (4.1)$$

where

$$R_{dc} = 2\pi \cdot \frac{n_{day}-1}{365} \text{ is the earth orbit deviation in radians.} \quad (4.2)$$

The equation of time t_{eq} proposed by Spencer in hours is:

$$t_{eq} = \frac{24}{2\pi} \cdot [0.000075 + 0.001868 \cdot \cos(R_{dc}) - 0.032077 \cdot \sin(R_{dc}) - 0.014615 \cdot \cos(2R_{dc}) - 0.04089 \cdot \sin(2R_{dc})]. \quad (4.3)$$

The solar time t_{sol} is determined on the basis of the equation of time, the time shift and the hour of the day.

The solar time in hours is:
$t_{sol} = n_{hours} + t_{eq} + t_{shift}$, (4.4)

where
n_{hours} is the actual (clock) time for the location
$t_{shift} = \frac{\lambda_W - 15° \cdot TZ}{15°}$ is the difference of hours between the longitude of the site and the actual path of the sun (4.5)
TZ is the time zone (UTC – Universal Time Coordinated)
λ_W longitude

The hour angle ω in degrees is:
$\omega = 15° \cdot (t_{sol} - 12)$. (4.6)

Knowing δ, ω and φw of the considered location, the solar altitude angle α_{sol} in degrees is calculated as:
$\alpha_{sol} = arcsin(\sin\delta \cdot \sin\varphi_w + \cos\delta \cdot \cos\varphi_w \cdot \cos\omega)$, (4.7)

while the solar zenith angle is $\theta_z = 90 - \alpha_{sol}$. When α_{sol} tends to 0, it should be approximated to such value.

The solar azimuth angle φ_{sol} can be calculated starting from:
$\sin(\varphi_{sol;aux1}) = \frac{\cos\delta \cdot \sin\omega}{\cos\alpha_{sol}} \rightarrow \quad \varphi_{sol;aux1} = arcsin\left(\frac{\cos\delta \cdot \sin\omega}{\cos\alpha_{sol}}\right)$. (4.8)

Since φsol can assume values greater than 90°, while the arcsine function returns values from -90° to +90°, we propose the following considerations:

$$\begin{cases} \sin\alpha_{sol} \geq \frac{\sin\delta}{\sin\lambda w} \quad \text{for} \quad \lambda w \geq 0 \quad \rightarrow \quad \varphi_{sol} = \varphi_{sol;aux1} \\ \sin\alpha_{sol} < \frac{\sin\delta}{\sin\lambda w} \quad \text{for} \quad \lambda w < 0 \quad \rightarrow \quad \varphi_{sol} = \varphi_{sol;aux1} \\ \text{otherwise} \rightarrow \quad \varphi_{sol} = \text{sgn}(\varphi_{sol;aux1}) \cdot [180 - |\varphi_{sol;aux1}|] \end{cases} \quad (4.9)$$

The solar azimuth angle is negative if solar projection is towards east (in the morning before solar noon) and it is positive if solar projection is towards west (afternoon).

The solar angle of incidence $\theta_{sol,ic}$, that is the angle between solar rays and the normal to the surface, can be calculated, after having fixed βic and γic, on the basis of α_{sol} and φ_{sol}.
Differently from what is reported in Annex A of UNI 10349-1 (Equation 4.10),
$\theta_{sol,ic} = arccos[\sin\alpha_{sol} \cdot \cos\beta_{ic} + \cos\alpha_{sol} \cdot \cos(\varphi_{sol} - \gamma_{ic}) \cdot \sin\beta_{ic}]$, (4.10)

we propose the following equation:

$$\theta_{sol,ic} = arccos[\sin\delta \cdot \sin\varphi_w \cdot \cos\beta_{ic} - \sin\delta \cdot \cos\varphi_w \cdot \sin\beta_{ic} \cdot \cos\gamma_{ic} + \cos\delta \cdot \cos\varphi_w \cdot \cos\beta_{ic} \cdot \cos\omega + \cos\delta \cdot \sin\varphi_w \cdot \sin\beta_{ic} \cdot \cos\gamma_{ic} \cdot \cos\omega + \cos\delta \cdot \sin\beta_{ic} \cdot \sin\gamma_{ic} \cdot \sin\omega]. \quad (4.11)$$

Calculating the solar angle of incidence as a function of fundamental angles (φw, δ, ω, β_{ic}, γ_{ic}) (Equation 4.11) and not with the general equation (Equation 4.10), allows to avoid problems in evaluating the solar angle of incidence at sunrise and sunset, when the solar altitude angle αsol, particularly in winter, is lower on the horizon (Figure 4.2 and 4.3).

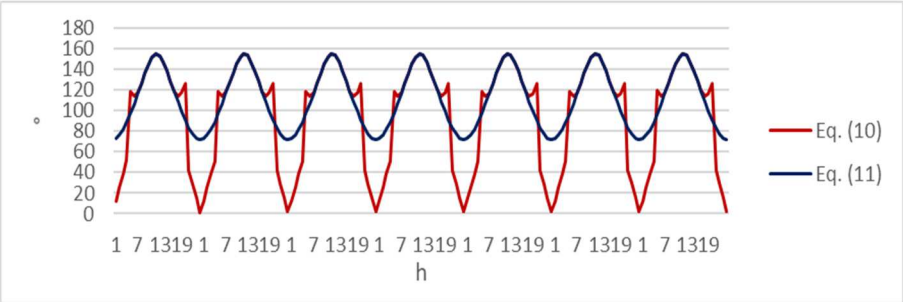

Figure 4.2. Solar incidence angle on the inclined surfaces, 19-25 December. Example: Rome (lat:41.8°- long:12.6°)

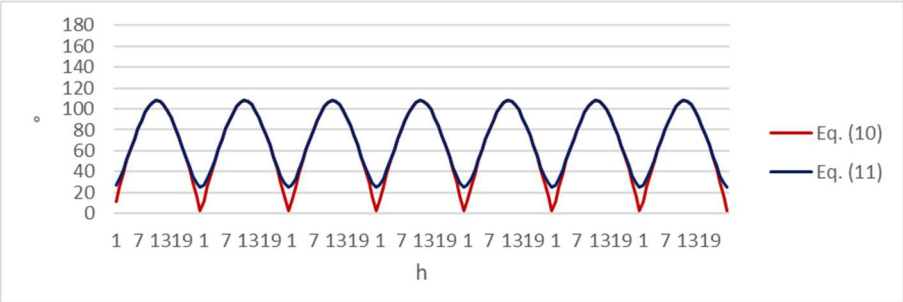

Figure 4.3. Solar incidence angle on the inclined surfaces, 19-25 June. Example: Rome (lat:41.8°- long:12.6°)

The extra-terrestrial radiation I_{ext} [125] in radians is:

$$I_{ext} = G_{sol,c} \cdot [1.000110 + 0.034221 \cdot \cos(R_{dc}) + 0.001280 \cdot \sin(R_{dc}) + 0.000719 \cdot \cos(2R_{dc}) + 0.000077 \cdot \sin(2R_{dc})], \quad (4.12)$$

where

$G_{sol,c} = 1366.1 \frac{W}{m^2}$ is the solar constant (ASTM E-490:2000)

4.2.2 Split between direct and diffuse solar irradiance on horizontal surface

The direct and diffuse fractions of the solar irradiance on the horizontal plane can be derived from the global solar irradiance on the same plane, which can be easily measured.
In the proposed calculation procedure, the Boland and Ridley 2007 model [126] is used to calculate the diffuse solar irradiance on horizontal plane $G_{sol;d}$ (W/m^2) as follows:

$$G_{sol;d} = \frac{1}{1+e^{-5+8.6 \cdot k_{T,d}}} \cdot G_{sol;g}, \quad (4.13)$$

where

$k_{T,d} = \frac{G_{sol;g}}{I_{ext,h}}$ is the clearness index of the atmosphere (relating to diffuse radiation) (4.14)

$I_{ext,h} = I_{ext} \cdot \sin \alpha_{sol}$ is the global extra-atmospheric solar irradiance on a horizontal plane (4.15)

therefore, the direct solar irradiance on horizontal plane (W/m^2) is:

$$G_{sol;b} = G_{sol;g} - G_{sol;d}. \quad (4.16)$$

As the solar energy reaching the Earth, due to the phenomena of diffusion and absorption, is lower than the energy incident on a surface hypothetically located outside the atmosphere, the method evaluates, for each value of extra-atmospheric radiation $(I_{ext,h})$, the clearness index of the atmosphere $k_{T,d}$, which expresses the percentage value of the amount of solar energy reaching the ground.

4.2.3 Calculation of direct and diffuse solar irradiance on tilted and oriented surfaces

The short-wave radiation reaching the earth's surface can be divided into direct, diffuse or reflected irradiance. Direct irradiance hits the Earth's surface with no interaction with particles in the atmosphere. The diffuse radiation consists of the Sun's rays scattered by gases and aerosols (i.e. dust, sulphates, smoke, salt, pollen, etc.). The reflected irradiance is mainly reflected from the Earth's surface and is therefore particularly important in areas with complex morphology.

The UNI 10349-1 standard calculates the direct irradiance I_{dir} (W/m^2) as follows:

$$I_{dir} = \frac{G_{sol;b}}{\sin \alpha_{sol}} \cdot \cos \theta_{sol;ic}, \quad (4.17)$$

where $\theta_{sol;ic}$ is the solar angle of incidence on the inclined surface according to Equation 4.10.

The problem with Equation 4.10 is that for hours very close to sunrise and sunset (i.e., for very small αsol), the denominator tends to zero so it could give excessively high direct irradiance values.
In order to prevent this issue, considering Linke's turbidity factor as a very convenient approximation for modelling the atmospheric absorption and the dispersion of solar radiation under a clear sky, we introduce this consideration :

$$\begin{cases} \frac{G_{sol;g}}{\sin\alpha_{sol}} \leq I_{ext} \cdot e^{(-m\cdot\delta_r\cdot T_L)} \quad \rightarrow \quad G_{sol;nb} = \frac{G_{sol;g}}{\sin\alpha_{sol}} \\ otherwise \qquad\qquad \rightarrow \quad G_{sol;nb} = I_{ext} \cdot e^{(-m\cdot\delta_r\cdot T_L)} \end{cases} \tag{4.18}$$

where

$m = m_0 \cdot e^{\left(-\frac{H}{8446}\right)}$ is the relative optical air mass (4.19)

$m_0 = \frac{1}{\sin\alpha_{sol}+0.50572\cdot(\alpha_{sol}+6.07995)^{-1.6364}}$ is the relative optical air mass (sea level)[127] (4.20)

H is the altitude of the site

$\delta_r = (9.4 + 0.9 \cdot m)^{-1}$ it is Rayleigh's extinction factor[128] (4.21)

T_L Linke turbidity coefficient (TL=1 for clean and dry air, TL=3 for clean air and with medium humidity, TL=6 for polluted air. The most realistic values are TL=1.5 or TL=2)[129]

The diffuse solar irradiance due to ground reflection irradiance $I_{dif;grnd}$ (W/m^2), is:

$$I_{dif;grnd} = G_{sol;g} \cdot \rho_{sol;grnd} \cdot \frac{[1-\cos\beta_{ic}]}{2} \tag{4.22}$$

where

$\rho_{sol;grnd}$ solar reflectivity of the ground (Albedo). It is usually assumed equal to 0.2[130].

$\frac{[1-\cos\beta_{ic}]}{2}$ view factor between the i-th surface and the visible portion of the soil. This factor can be used if the soil has an unlimited extension in relation to the surface and/or there are no reflective surfaces. If the ground surface is not horizontal or has a limited extension and/or reflective surfaces, the view factor must be calculated graphically or with solar simulation programs.

The term ‘sky model’ refers to the way in which the solar radiation is imagined to be distributed in the sky. There are several sky models for the calculation of diffuse irradiance. Specifically, a fraction of the radiation is projected directly from the solar disk, while a second part is diffused from the atmosphere according to an effect called scattering. The scattering is differently managed depending on the chosen sky model.
For the calculation of the diffuse irradiance, EN ISO 52010-1 uses Perez's anisotropic sky model, which considers the sky composed of a perfectly diffuse and isotropic part and an anisotropic part, depending on the cloudiness of the sky, i.e. the circumsolar irradiance.

In this work, instead, we chose the isotropic sky model, which considers the sky as a perfectly diffuse and uniform source of radiation, thus not considering the anisotropic (directional and non-uniform) components.

The circumsolar irradiance I_{circum} (W/m^2), is [131]:

$$I_{circum} = G_{sol;d} \cdot \frac{1+\cos \beta ic}{2} \quad (4.23)$$

The total diffuse irradiance $I_{dif,tot}$ (W/m^2), is:

$$I_{dif,tot} = I_{circum} + I_{dif;grnd} \quad (4.24)$$

The total solar irradiance on the inclined surface I_{tot} (W/m^2), is:

$$I_{tot} = I_{dir,tot} + I_{dif,tot} \quad (4.25)$$

4.3 Evaluation of solar radiation prediction models

4.3.1 Case study

The calculation procedure reported in Paragraph 4.2 and the one included in EN ISO 52010-1:2017 are compared with those implemented in Trnsys 17 and Meteonorm 7.3 software.
The considered locations are: De Bilt (Netherlands), Malaga (Spain), Paris (France), Rome (Italy) and Stockholm (Sweden). This choice was made mainly with the aim of evaluating how the different calculation procedures respond to the different European climates.
The datasets of each city in the case study were obtained from meteorological stations officially recognized by the World Meteorological Organization (WMO) (see Table 4.2 and Figure 4.4).

Table 4.2. Geographical coordinates of the weather stations and main climate data of the analysed cities. Cfb: temperate oceanic climate, Csa: warm-summer Mediterranean climate.

	De Bilt	**Malaga**	**Paris**	**Rome**	**Stockholm**
Geographic Data					
Latitude (°)	52,10	36,67	48,82	41,80	59,35
Longitude (°)	5,18	-4,48	2,33	12,58	17,95
Altitude (m)	40	7	75	131	11
UTC (-)	1	1	1	1	1
WMO - Weather station code (-)	62600	84820	71560	162390	24640
Climatic Data					
Gsol,g,H,max (W/m^2)	896	1038	946	1045	848
max Temp	32,0	40,2	33,7	36,9	30,5
min Temp (°C)	-7,2	2,1	-4,2	-2,4	-15,3
Climate classification (Köppen/Geiger)	Cfb	Cfb	Cfb	Csa	Csa

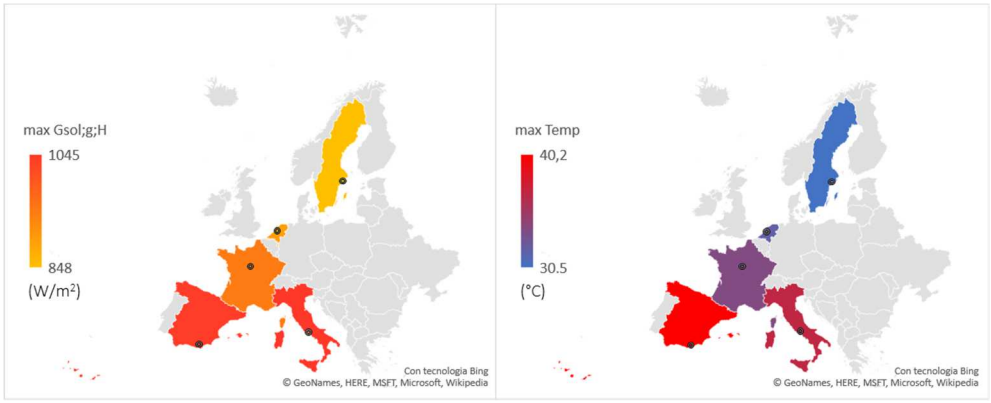

Figure 4.4. Distribution of maximum global horizontal solar radiation and maximum outdoor temperature

The four calculation procedures considered in this work involve the use of the following models for the calculation of direct and diffuse solar radiation in the horizontal plane: (i) Perez (1991)[132] implemented in Meteonorm 7.3 software, (ii) Reindl et.al. [133] as a function of the clearness index, solar altitude angle, ambient temperature, and relative humidity, which is used in Trnsys' type 16, (iii) Erbs 1982[134] implemented in the algorithm defined in EN ISO 52010-1:2017 and (iv) Boland and Ridley 2007[126] proposed in Paragraph 4.2 (see Table 4.3). To separate direct and diffuse global radiation on a vertical surface, Meteonorm, TRNSYS and EN ISO 52010-1:2017 use the Perez 1990 model [135] while the methodology proposed in Paragraph 4.2 uses the Liu and Jordan model 1960 [131]. Table 4.3 summarizes the models employed to calculate solar direct and diffuse irradiance both on horizontal and tilted surfaces.

Table 4.3. Mathematical relationships used in the calculation procedures examined in this case study.

	Meteonorm 7.3	**Trnsys 17**	**ISO 52010:2010**	**Proposed methodology**
Horizontal surface	Perez 1991	Reindl 1990	Erbs 1982	Boland and Ridley 2007
Tilted surface	Perez 1990	Perez 1990	Perez 1990	Liu and Jordan 1960

4.3.2 Data analysis and evaluation of models for calculating radiation on horizontal plane

By comparing the results of solar diffuse irradiance on horizontal plane for all the cities and all the tested models, it can be observed that the Erbs model overestimates by about 61.8% the annual average (x_m), 54.9% the standard deviation (σ) and 11.6% the maximum value (x_{max}) (see Table 4.4).

The mean annual value of solar diffuse irradiance on horizontal plane was calculated considering 8760 hours, thus including null night values.

Table 4.4. Mean annual (x_m), standard deviation (σ) and maximum value (x_{max}) of horizontal diffuse irradiance in W/m^2 for all cities of the case study.

Horizontal surface		Perez 1991	Boland et al. 2007	Erbs 1982	Reindl 1990
De Bilt	x_m	66,1	65,0	97,5	67,1
	σ	98,1	95,7	143,2	99,6
	x_{max}	425,0	392,3	466,7	417,2
Malaga	x_m	74,1	75,3	144,9	91,6
	σ	102,7	103,1	178,2	122,5
	x_{max}	498,0	433,1	479,3	453,0
Paris	x_m	69,0	67,9	105,0	71,2
	σ	103,5	100,3	151,2	104,5
	x_{max}	452,0	402,6	470,1	419,0
Rome	x_m	76,6	76,1	123,6	78,9
	σ	109,3	107,0	163,0	108,7
	x_{max}	482,0	426,1	475,2	443,9
Stockholm	x_m	56,2	57,8	97,5	58,7
	σ	86,9	87,3	145,9	86,7
	x_{max}	395,0	359,3	466,0	367,8

Results obtained by performing a frequency analysis show that for all five locations the Erbs model is the only one to have about 10% of solar diffuse irradiance on horizontal plane included between 400 W/m^2 and 500 W/m^2. Specifically,
7.16% in De Bilt, 15.92% in Malaga, 8.73% in Paris, 11.13% in Rome and 7.91% in Stockholm (see Figure 4.5).

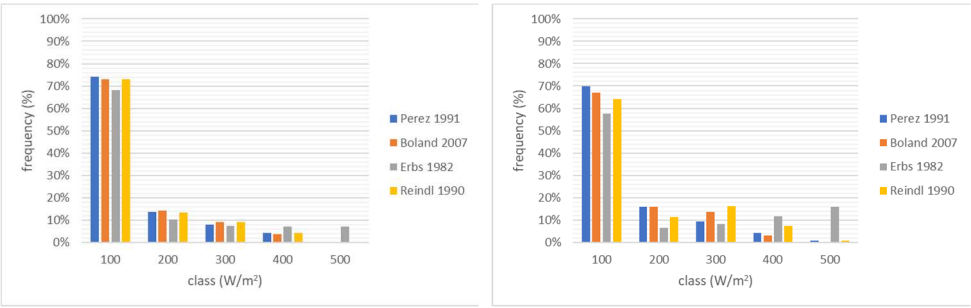

(a) (b)

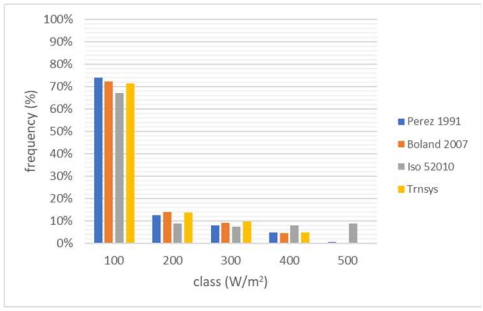

(c)

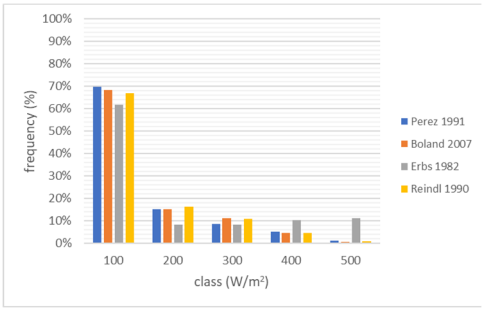

(d)

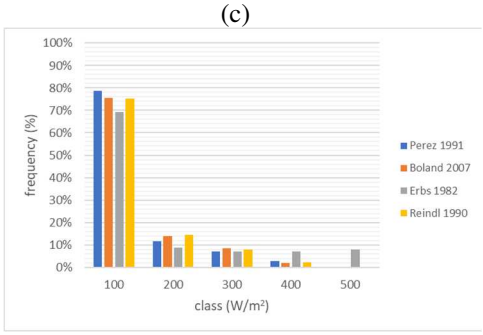

(e)

Figure 4.5 Frequency distribution of diffuse horizontal irradiance. (a) De Bilt, (b) Malaga, (c) Paris, (d) Rome; (e) Stockholm

We compared solar diffuse irradiances on horizontal plane, obtained from Perez 1991, Erbs 1982 and Boland & Ridley 2007 models, taking Trnsys (which implements Reindl 1990 model) as a baseline.

The choice to use Reindl model as reference is due to two main reasons: firstly, it proposes a regression based mainly on experimental data from European locations; secondly, this model is the only among those analyzed that includes more predictive variables in the calculation of solar direct irradiance on horizontal plane, i.e. clearness index, solar altitude angle, ambient temperature and relative humidity.

Specifically, Reindl states that, although the clearness index is the most important variable for low-medium kT values (cloudy sky), in case of high kT values (clear sky) the weight of the clearness index decreases dramatically while the solar altitude angle becomes predominant. Moreover, it claims that the use of its model results in a 26% improvement over Erbs' model for the same locations [136].

The comparison among models was performed by considering the following metrics:

- Percentage error between maximum diffuse irradiance peaks

$$\Delta(x_{max}) = \frac{y_{max;i} - x_{max;i}}{x_{max;i}} \cdot 100 \quad (4.26)$$

- Mean Bias Error (MBE%)

$$MBE\% = \frac{\sum_{i=1}^{N}(y_i - x_i)}{N \cdot x_m} \cdot 100 \quad (4.27)$$

- Root Mean Square Error (RMSE%)

$$RMSE\% = \frac{\sqrt{\frac{\sum_{i=1}^{N}(y_i - x_i)^2}{N}}}{x_m} \cdot 100 \quad (4.28)$$

where
yi: i-th value calculated with Perez or Boland et al. or Erbs model.
xi: i-th value calculated with Reindl model
N: total number of hours in a year (i.e., 8760)
xm: mean annual value of irradiances according to Reindl

Table 4.5. Errors on horizontal diffuse irradiance for the considered locations. Gray cells are those with the minimum error.

Horizontal surface		**Perez 1991 vs Reindl 1990**	**Boland et al. 2007 vs Reindl 1990**	**Erbs 1982 vs Reindl 1990**
De Bilt	Δ(xmax)	1,86%	-5,97%	11,85%
	MBE%	-1,55%	-3,17%	45,38%
	RMSE%	45,24%	28,24%	110,02%
Malaga	Δ(xmax)	9,93%	-4,40%	5,80%
	MBE%	-19,14%	-17,74%	58,22%
	RMSE%	77,06%	54,87%	112,76%
Paris	Δ(xmax)	7,87%	-3,93%	12,18%
	MBE%	-3,05%	-4,55%	47,54%
	RMSE%	55,13%	36,96%	108,66%
Rome	Δ(xmax)	8,58%	-4,01%	7,05%
	MBE%	-2,97%	-3,63%	56,53%
	RMSE%	30,47%	28,05%	120,06%
Stockholm	Δ(xmax)	7,40%	-2,30%	26,70%
	MBE%	-4,28%	-1,45%	66,14%
	RMSE%	28,73%	41,14%	147,44%

For what concerns the percentage error between maximum diffuse irradiance peaks and root mean square error (RMSE%), the Boland and Ridley 2007 model is the one that best matches Reindl model for the majority of considered cities, except for De Bilt where Perez 1991 algorithm reaches the best results.

All the performed analysis suggest that Erbs 1982 model is the one that most overestimate the solar diffuse irradiance on horizontal plane. To support this, Figure B.1 n Appendix B displays daily trends of solar diffuse irradiance for two typical days: 21 January and 21 July.

Summarizing, the calculation procedure for the diffuse horizontal irradiance proposed in Paragraph 4.2 is the closest to the baseline (i.e., Trnsys) while the worst model is the one described in EN ISO 52010-1:2017.

4.3.3 Estimation of irradiance on tilted and oriented surfaces

Once the split between direct and diffuse irradiance on the horizontal plane is performed, the direct and diffuse irradiances on tilted and oriented surfaces are calculated according to the four cardinal points.
Meteonorm, TRNSYS and EN ISO 52010-1:2017 use the Perez 1990 model, while the methodology proposed in Paragraph 4.2 uses the Liu and Jordan 1960 model (see Table 4.3). As reported in Figure 4.6, mean global irradiances on south-exposed surfaces tend to have the highest values with "Perez 1991 – Perez 1990" (P-P henceforth) combination and the lowest values with "Erbs 1982 – Perez 1990" (E-P henceforth) combination, due to an underestimation of direct irradiance. "Boland et al.2007 – Liu et al.1960" (B-L henceforth) and "Reindl 1990 – Perez 1990" (R-P henceforth) combinations have similar values that are intermediate respect to the two above-mentioned models.
Such considerations apply for every location of the case study except for Malaga where the "R-P" combination has the lowest values of global mean irradiance. However, standard deviation is the highest in Malaga, which highlights a greater oscillation of the estimated values (see Table 4.6).

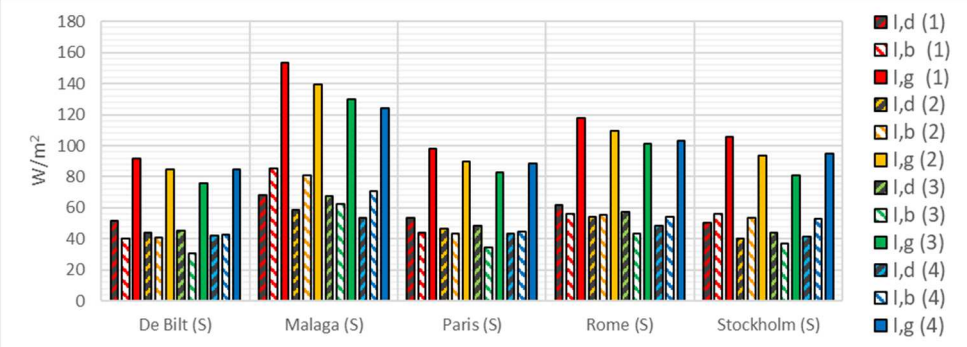

Figure 4.6 Diffuse, direct and global mean annual irradiance on a south-oriented vertical surface. (1) Perez 1991 + Perez 1990, (2) Boland and Ridley 2007 + Liu and Jordan 1960, (3) Erbs 1982 + Perez 1990, (4) Reindl 1990 + Perez 1990.

Table 4.6 Standard deviation of diffuse, direct and global irradiance on a south-facing vertical surface (W/m^2).

Tilt surface		Perez 1991 + Perez 1990			Boland 2007+ Liu 1960			Erbs 1982 + Perez 1990			Reindl 1990 + Perez 1990		
		I,d	I,b	**I,g**	I,d	I,b	**I,g**	I,d	I,b	**I,g**	I,d	I,b	**I,g**
S	De Bilt	76,4	104,5	**163,7**	63,8	102,3	**144,9**	65,2	74,5	**130,2**	62,2	106,6	**150,8**
	Malaga	87,2	157,2	**224,4**	76,1	150,4	**201,1**	82,0	109,7	**180,1**	71,5	140,4	**194,7**
	Paris	79,6	112,7	**172,7**	67,4	108,3	**153,4**	68,9	80,6	**139,4**	63,9	109,7	**155,8**
	Rome	83,9	127,1	**189,9**	73,5	124,3	**171,6**	75,1	91,4	**154,6**	65,7	119,6	**168,8**
	Stockholm	74,7	128,9	**187,2**	59,3	124,2	**163,1**	64,8	84,5	**140,7**	60,9	119,8	**167,9**

On east-exposed surfaces "P-P" combination shows again the highest irradiance values and "R-P" combination has again the lowest mean global irradiance values, while "B-L" and "E-P" tend to get intermediate values (see Figure 4.7). This trend recurs on all locations except for Stockholm; such city has also the highest standard deviation for direct and global irradiances (see Table 4.7).

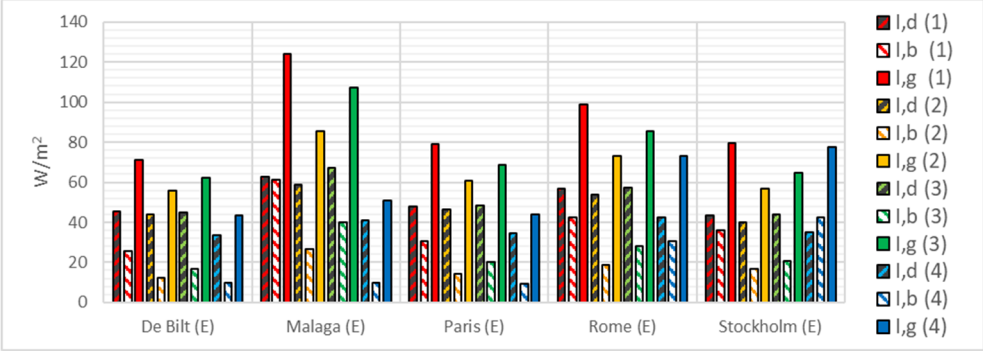

Figure 4.7 Diffuse, direct and global mean annual irradiance on a east-oriented vertical surface. (1) Perez 1991 + Perez 1990, (2) Boland and Ridley 2007 + Liu and Jordan 1960, (3) Erbs 1982 + Perez 1990, (4) Reindl 1990 + Perez 1990.

Table 4.7 Standard deviation of diffuse, direct and global irradiance on an east-facing vertical surface (W/m^2).

Tilt surface		Perez 1991 + Perez 1990			Boland 2007+ Liu 1960			Erbs 1982 + Perez 1990			Reindl 1990 + Perez 1990		
		I,d	I,b	**I,g**	I,d	I,b	**I,g**	I,d	I,b	**I,g**	I,d	I,b	**I,g**
E	De Bilt	65,0	93,6	**137,9**	63,8	48,2	**94,2**	65,2	56,3	**104,1**	50,2	41,1	**81,8**
	Malaga	78,7	142,9	**200,0**	76,1	69,4	**128,2**	82,0	92,0	**151,2**	57,4	29,7	**81,5**
	Paris	68,2	104,6	**150,3**	67,4	53,7	**101,5**	68,9	63,4	**113,4**	51,1	37,9	**80,1**
	Rome	74,7	121,2	**172,6**	73,5	60,6	**114,4**	75,1	77,0	**131,2**	58,0	89,3	**134,3**
	Stockholm	62,2	113,4	**156,0**	59,3	59,3	**100,4**	64,8	61,9	**109,5**	50,1	124,7	**158,9**

On west-oriented surfaces, mean global irradiances calculated by "B-L" and "R-P" combinations for De Bilt, Malaga and Paris tend to be equivalent, while the "E-P" combination gets the lowest values of global irradiance for all the cities due to the underestimation of direct irradiance (see Figure 4.8).

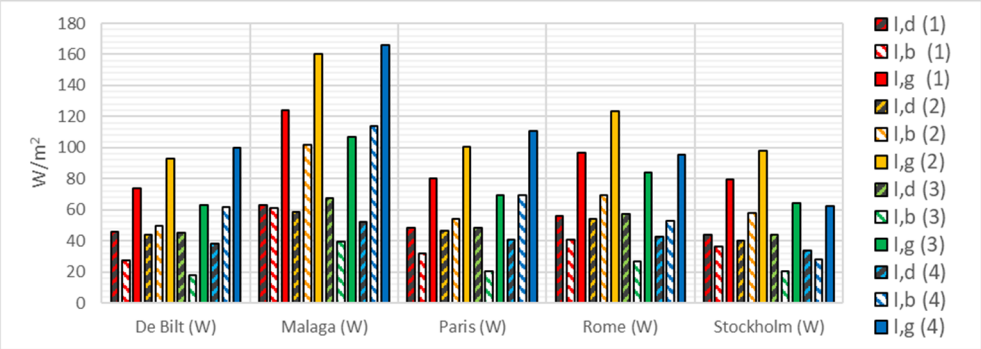

Figure 4.8 Diffuse, direct and global mean annual irradiance on a west-oriented vertical surface. (1) Perez 1991 + Perez 1990, (2) Boland and Ridley 2007 + Liu and Jordan 1960, (3) Erbs 1982 + Perez 1990, (4) Reindl 1990 + Perez 1990

Table 4.8 Standard deviation of diffuse, direct and global irradiance on a west-facing vertical surface (W/m^2).

Tilt surface		Perez 1991 + Perez 1990			Boland 2007+ Liu 1960			Erbs 1982 + Perez 1990			Reindl 1990 + Perez 1990		
		I,d	I,b	**I,g**	I,d	I,b	**I,g**	I,d	I,b	**I,g**	I,d	I,b	**I,g**
W	De Bilt	65,8	94,8	**140,5**	63,8	146,6	**169,5**	65,2	55,7	**103,9**	53,6	164,4	**192,7**
	Malaga	78,5	143,9	**199,7**	76,1	220,1	**244,0**	82,0	91,1	**150,2**	71,2	221,0	**272,9**
	Paris	69,	104,	**151,**	67,	158,	**182,**	68,	62,	**112,**	57,	176,	**209,**

Rome	173,8	120,4	**169,8**	73,5	183,5	**206,9**	75,1	73,4	**127,5**	55,1	148,9	**180,8**
Stockholm	62,9	111,1	**154,5**	59,3	159,5	**179,9**	64,8	59,8	**107,3**	49,2	87,8	**125,3**

As for north-exposed surfaces, the "B-L" and "E-P" combinations tend to have equivalent mean value and standard deviation, while the "R-P" combination underestimates global and diffuse irradiances on all five locations (see Figure 4.9).

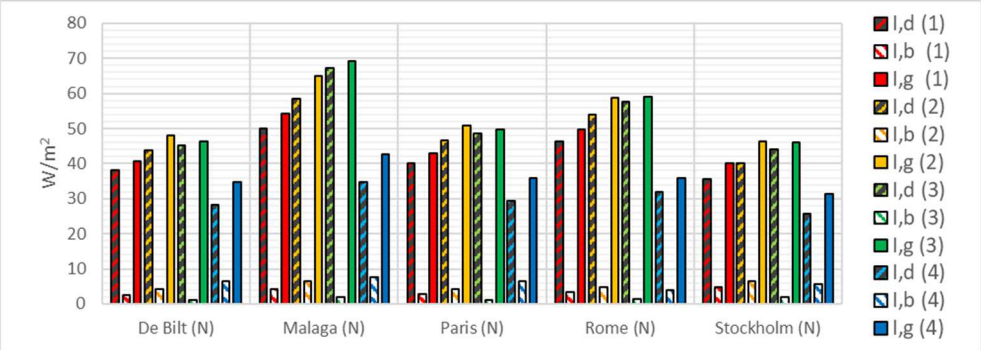

Figure 4.9 – Diffuse, direct and global mean annual irradiance on a north-oriented vertical surface. (1) Perez 1991 + Perez 1990, (2) Boland and Ridley 2007 + Liu and Jordan 1960, (3) Erbs 1982 + Perez 1990, (4) Reindl 1990 + Perez 1990.

Table 4.9 Standard deviation of diffuse, direct and global irradiance on a north-facing vertical surface (W/m^2).

Tilt surface		Perez 1991 + Perez 1990			Boland 2007+ Liu 1960			Erbs 1982 + Perez 1990			Reindl 1990 + Perez 1990		
		I,d	I,b	**I,g**	I,d	I,b	**I,g**	I,d	I,b	**I,g**	I,d	I,b	**I,g**
N	De Bilt	52.7	16.4	**56.8**	63.8	28.8	**69.4**	65.2	6.4	**65.9**	39.0	37.3	**54.7**
	Malaga	61.5	19.1	**66.5**	76.1	33.7	**82.0**	82.0	8.0	**83.2**	43.9	37.0	**60.5**
	Paris	55.4	17.0	**59.5**	67.4	28.4	**72.5**	68.9	6.7	**69.6**	40.2	37.8	**56.6**
	Rome	59.6	18.1	**63.8**	73.5	28.8	**77.9**	75.1	7.2	**75.9**	40.7	23.2	**47.8**
	Stockholm	49.3	24.6	**52.1**	59.3	37.4	**69.3**	64.8	9.2	**66.0**	34.8	30.5	**49.3**

As previously, Trnsys was assumed as the baseline and the results were compared by considering the following three metrics: percentage error between maximum irradiance peaks, mean bias error (MBE%) and root mean square error (RMSE%).As shown in Appendix B.2, the algorithm proposed in Paragraph 4.2, i.e. combination of Boland & Ridley 2007 and Liu & Jordan 1960, best matches Trnsys' results for all orientations for De Bilt, Malaga and Paris. The irradiance for Rome is well approximated with the following combinations: (i) Boland et al.-Liu et al. for south-oriented surfaces, (ii) Perez 1991-Perez

1990 for west- and north-oriented surfaces, (iii) Reindl 1990-Perez 1990 for east-oriented surfaces. Lastly, for Stockholm the combination of Perez 1991-Perez 1990 best matches Trnsys' results for all orientations.

In order to confirm the data presented in Appendix B2, the trends of diffuse irradiance on vertical and oriented surfaces of two standard days (21 January and 21 July) are shown in Appendix B1.

Summing up the estimated irradiances of each algorithm (see Table 4.10), it is evident that the results obtained with EN ISO 52010-1:2017 are distant, in terms of kWh/m^2 year, from the mean value of the other three considered procedures.

In fact, by averaging the percentage errors for all cities and for all vertical surfaces, the E-P model contained in EN ISO 52010-1:2017: (i) overestimates the annual diffuse irradiance by +3.3% (south), +10.8% (west), +14.3% (east) and +30.0% (north), (iii) underestimates the annual direct irradiance by -24.2% (south), -55.9% (west), -0.9% (east) and -69.4% (north) and (iv) shows a deviation of the global annual irradiance of -14.8% (south), -28.5% (west), +1.4% (east) and +7.9% (north).

The underestimation of direct and global irradiances, mainly on south- and west-oriented surfaces, necessarily leads to a decrease in solar gains, which results, under the same conditions, in a lower energy consumption during summer and a higher energy consumption during winter.

Table 4.10 Annual sum of the irradiances estimate with: Perez 1991+Perez 1990 (P-P), Boland/Ridley 2007+Liu/Jordan 1960 (B-L), Reindl 1990+Perez 1990 (R-P) and Erbs 1982+Perez 1990 (E-P). Aver. is the average of the "P-P", "B-L" and "R-P" models.
Δ(%)= [(E-P)-Aver.]/Aver.

kWh/m² year		Gsol,g	Gsol,d	Gsol,b	I,g (S)	I,d (S)	I,b (S)	I,g (W)	I,d (W)	I,b (W)	I,g (E)	I,d (E)	I,b (E)	I,g (N)	I,d (N)	I,b (N)
De Bilt	P-P	991	579	412	806	454	352	647	404	243	624	398	226	356	333	23
	B-L	991	569	422	742	384	359	816	384	432	490	384	106	420	384	37
	R-P	991	588	401	843	370	374	975	337	539	477	293	86	403	248	56
	Aver.	991	578	412	797	402	362	812	375	405	530	358	139	393	322	39
	E-P	991	854	137	665	396	270	551	396	156	544	396	148	406	396	10
	Δ(%)	**0,0 %**	**47,7 %**	**-66,8 %**	**-16,5 %**	**-1,7 %**	**-25,4 %**	**-32,2 %**	**5,5 %**	**-61,6 %**	**2,5 %**	**10,5 %**	**6,3 %**	**3,1 %**	**23,0 %**	**-74,5 %**
Malaga	P-P	1829	649	1180	1344	598	746	1089	551	538	1087	550	536	476	439	37
	B-L	1829	660	1168	1219	513	706	1403	513	890	748	513	235	569	513	56
	R-P	1829	802	940	1262	468	620	1631	459	998	621	361	86	547	305	68

	Aver.	1829	704	1096	1275	526	691	1374	508	809	818	475	286	531	419	54
	E-P	1829	1269	559	1137	590	547	937	590	347	938	590	348	606	590	16
	Δ(%)	**0,00 %**	**80,4 %**	**-49,0 %**	**-10,9 %**	**12,0 %**	**-20,8 %**	**-31,8 %**	**16,1 %**	**-57,1 %**	**14,6 %**	**24,2 %**	**22,0 %**	**14,2 %**	**40,8 %**	**-69,6 %**
Paris	P-P	1102	604	498	857	472	385	702	425	277	691	421	270	377	352	25
	B-L	1102	595	507	789	408	381	881	408	473	531	408	123	446	408	38
	R-P	1102	623	469	883	382	392	1077	358	610	492	301	82	425	258	58
	Aver.	1102	608	492	843	420	386	887	397	453	571	377	158	416	339	40
	E-P	1102	920	183	725	425	300	605	425	180	600	425	175	436	425	11
	Δ(%)	**0,00 %**	**51,4 %**	**-62,9 %**	**-14,0 %**	**1,2 %**	**-22,4 %**	**-31,8 %**	**7,1 %**	**-60,3 %**	**5,1 %**	**12,9 %**	**10,6 %**	**4,9 %**	**25,4 %**	**-73,6 %**
Rome	P-P	1403	671	732	1033	543	491	848	491	358	868	496	372	435	405	30
	B-L	1403	666	737	959	474	486	1082	474	609	640	474	166	515	474	41
	R-P	1403	692	712	1043	427	476	975	372	463	782	373	270	454	280	34
	Aver.	1403	676	727	1012	481	484	969	445	476	763	447	269	468	386	35
	E-P	1403	1082	321	886	504	382	738	504	234	751	504	247	517	504	13
	Δ(%)	**0,00 %**	**60,0 %**	**-55,9 %**	**-12,4 %**	**4,8 %**	**-21,1 %**	**-23,9 %**	**13,1 %**	**-50,9 %**	**-1,6 %**	**12,6 %**	**-8,2 %**	**10,4 %**	**30,5 %**	**-63,4 %**
Stockholm	P-P	975	492	483	929	439	489	699	383	316	697	380	317	352	310	42
	B-L	975	507	468	819	351	468	858	351	507	496	351	146	407	351	56
	R-P	975	514	461	927	364	466	642	296	248	776	307	372	371	225	48
	Aver.	975	504	471	892	385	474	733	343	357	656	346	278	377	296	49
	E-P	975	854	121	711	385	326	565	385	180	566	385	180	402	385	17
	Δ(%)	**0,00 %**	**69,4 %**	**-74,3 %**	**-20,3 %**	**0,1 %**	**-31,4 %**	**-22,9 %**	**12,3 %**	**-49,7 %**	**-13,8 %**	**11,5 %**	**-35,1 %**	**6,7 %**	**30,4 %**	**-65,8 %**

4.4 Conclusion

In the present work we proposed a novel methodology for the calculation of direct and diffuse irradiation on every surface, which represents an improvement of the Annex A of the national UNI 10349-1:2016. The methodology may be considered as an alternative to EN ISO 52010-1:2017. Furthermore, we performed a comparative analysis of four procedures for five European cities characterized by different climatic conditions (Stockholm, De Bilt, Paris, Rome and Malaga), in order to test performance and limits of the four different calculation algorithms.

Results show that the Erbs 1982 model, implemented in EN ISO 52010-1:2017, most overestimates the diffuse solar irradiance on horizontal plane for all the considered locations. By considering Reindl 1990 model, implemented in Trnsys, as our baseline, Perez 1991, Boland and Ridley 2007 and Erbs 1982 models respectively reach a MBE of -6.2%, -6.1% and 54.8% and a RMSE of 47.3%, 37.9% e 119.8%.

For what concerns direct, diffuse and global irradiance on south-, east- and west-exposed vertical surfaces, the proposed calculation method, which implements Boland and Ridley 2007/Liu and Jordan 1960 combination, obtains values that are the closest to Trnsys' algorithm. Instead, for north-oriented surfaces the most precise estimation is shown by Perez 1991/Perez 1990 combination. It is relevant to note how percentage values for north-oriented surface, shown in table B.1 to B.5, are calculated on low irradiance values; therefore, small numerical difference among models brings to high percentage errors. Moreover, mean differences on north diffuse irradiances are 12.0 W/m^2, 18.6 W/ m^2 and 22.5 W/ m^2 for Perez 1991/ Perez 1990, Boland et al 2007/Liu et al1960, and Erbs 1982/Perez 1990 respectively, with respect to the reference model (Reindl 1990-Perez 1990).

Adding up the hourly irradiances over a period of one year, the EN ISO 52010-1:2017 algorithm shows values of diffuse irradiance on vertical surfaces similar to the other models, although the diffuse solar irradiance on horizontal plane is overestimated by approximately 61.8% (382 kWh/ m^2 year). Moreover the EN ISO 52010-1:2017 algorithm underestimates annual direct irradiance on south-exposed surfaces of about -24.2% (115 kWh/ m^2 year), on west-exposed of about -55.9% (281 kWh/ m^2 year), on-east exposed of about -0.9% (6 kWh/ m^2 year) and on north-exposed of about -69.4% (30 kWh/ m^2 year).

The proposed calculation algorithm to estimate solar direct and diffuse irradiance on horizontal and tilted surfaces appears to be a valid alternative to the models currently used by European and Italian regulations.

In future work, we plan to extend the evaluation of the considered calculation procedures by considering a larger number of cities. We also intend to verify how the splitting models of direct and diffuse irradiance analyzed in this work affect the solar gains and energy needs of buildings calculated with EN ISO 52016-1:2017.

Chapter 5.
Artificial intelligence and energy efficiency: The case of ventilated facades

5.1 Ventilated facades in Literature

In order to promote energy efficiency, a promising construction technique is represented by Ventilated façades (VFs), which have been recently proposed and tested as an alternative to standard façades, typically featuring external thermal insulation composite systems.
The VF is a building element that is fixed to the external surface of a building with mechanical anchors. A VF consists mainly of three layers: the wall adjacent to the inner side of the building, an exposed outer skin and a ventilated air space (also referred to as cavity) separating the previous layers. The ventilated air space has openings at the bottom and top through which outside air can enter and flow [137][138].
As known in literature, the use of ventilated façades can significantly reduce winter and summer energy consumption of buildings [139][140][141][142] as well as guarantee greater durability of the cladding. In fact, the ventilation behind the support allows for a faster evaporation of the water absorbed by the porous coatings with the result of a significant humidity reduction [143][144][145].
Although these issues are important, it is difficult to determine the optimum airflow velocities in the ventilated cavity for different types of external cladding and climatic conditions. Some studies tried to determine the best configuration by using empirical approaches [146][147] but testing several configurations in situ is usually costly and time-consuming.
For this reason, there are many studies in the literature that use theoretical calculations [148][149], numerical analysis [150] and especially Computational Fluid Dynamics (CFD) simulations [151][152][153][154]. As highlighted by Rahiminejad et al. [155], each of these methods show some criticalities: (i) theoretical calculations have limited accuracy, need extra measurements and do not give information about parameters distribution; (ii) numerical analysis gives information about the distribution of the parameters but has low accuracy, while (iii) the CFD approach, although accurate, is very onerous, extremely dependent on the knowledge and experience of the user and requires extra measurements for validation.
Therefore, there is the need for an alternative method that may combine the advantage of a realistic measurement (as in an in situ experimentation) with the possibility of varying the boundary conditions (in our case, the air velocity in the cavity) as in a CFD simulation.
In this paper, a comparative analysis is conducted on three types of VFs, with emphasis on a novel design variant that couples the benefits of (i) replacing multi-layer assemblies with a monolayer structure that uses cement-bonded wood fiber blocks' air gaps as ventilated

cavities and (ii) easy-to-implement and cost-saving design, notably regarding the details of the metallic support. The novel design variant is compared with two heavyweight, multi-layered designs, already investigated elsewhere[139], that differ in the position of the massive layer with respect to the ventilated cavity.
In this study, a thermo-physical analysis is performed on each design variant under equal boundary conditions and under the influence of mechanically-controlled cavity ventilation, to delve into the dynamic response of envelope and indoors with regards to outdoor forcing, in-cavity forcing and wall typology. An experimental dataset was built-up by varying the operating parameters during a month-long monitoring campaign on a test-room with all VF variants aligned on the same wall. The data were used to build machine learning models to predict temperatures and heat fluxes under different boundary conditions and hence propose a novel approach for the study of VFs that may be able to solve the above-mentioned issues. Compared to other research lines on VFs, this study is unique in four main aspects: (i) the thermo-dynamic analysis is experimental and comparative, on account of different thermal mass, position of the cavity and geometry; (ii) the VFs are mated with a controlled ventilation system, used to parameterize the thermodynamic behavior under stepwise variations of the air inflow; (iii) temperatures and heat fluxes are predicted by means of machine learning models; (iv) the best configuration is determined through simulations performed by means of the above-mentioned machine learning models, without the need of onerous in situ experimentations.

5.2 Materials and Methods

5.2.1 Case study building and VF variants

The experimental study was conducted in Agugliano (Central Italy, latitude: 43.54°, longitude: 13.37°, altitude: 137 m a.s.l.). Owing to its warm and temperate climate, Agugliano falls into the Cfa class, according to the upgraded Köppen-Geiger classification [156]. Agugliano has an average temperature of 15°C and an average annual rainfall of 681mm. The hottest month on average is July with 25.1°C, while the coldest is January with an average temperature of 6.2°C. The monitoring campaign lasted 1 month during the hottest time of the year (August 8, 2019 - September 8, 2019) to verify the performance of the VFs in summertime, under intense solar exposure (see Figure 5.1 and Tab. 5.1).

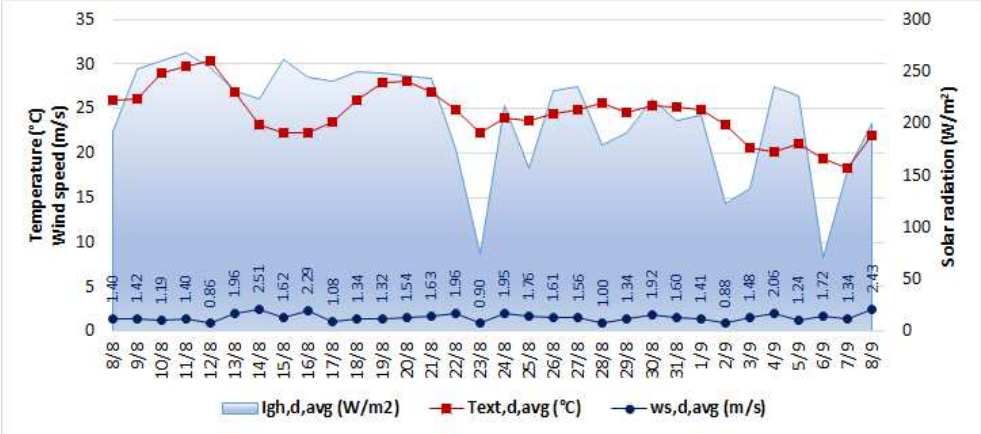

Figure 5.1. Climate data of the monitored period (8 August -8 September)

Table 5.1. Average, maximum and minimum values of the climatic parameters of the experimental campaign

	External temperature (°C)	**Relative humidity (%)**	**Pressure (hPa)**	**Wind speed (m/s)**	**Global horizontal radiation (W/m²)**
average	24.2	63.7	999.4	1.3	67.3
max	27.1	73.9	1000.2	5.5	248.3
min	22.1	49.4	998.6	0.0	0.1

The test-room (see Figure 5.2) is a windowless, uninhabited space especially engineered for research purposes. The design is carefully conceived to minimize the disturbance of chaotic phenomena and the interaction between competing phenomena (e.g. internal gains, solar gains), thus allowing to isolate the contribution of individual thermo-physical parameters. The reader is referred to [157] for an exemplary study taking advantage of the unique design features. With a net area of 12.54 m^2 and a volume equal to 36.10 m^3 the room is highly sensitive to indoor perturbations, while thanks to its hyper-insulation (U-value = 0.196 W/ m^2K) it attenuates the oscillations caused by outdoor variations. The bearing structure relies on cross laminated timber panels and is suspended at 0.4 m above the ground to minimize the heat transfer with the ground. The walls are perfectly aligned with cardinal directions and are composed by different layers as detailed in Table 5.2.

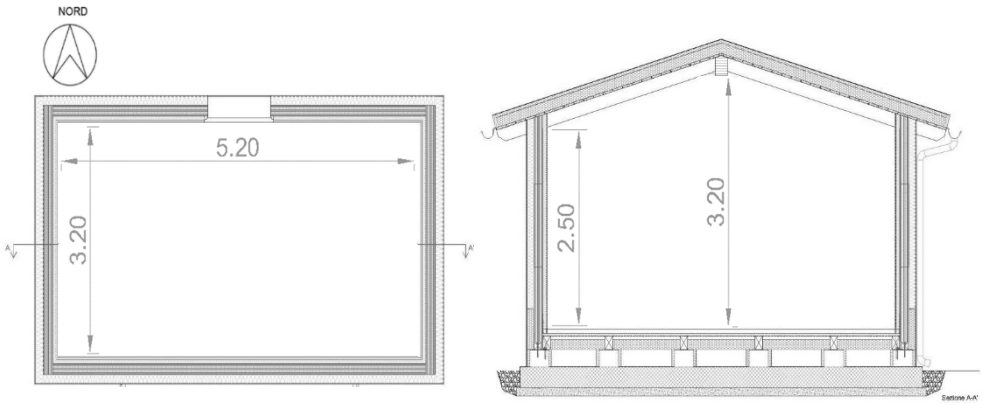

Figure 5.2. Test-room plan and section.

Table 5.2. Composition of the structure and Ventilated Skin prototypes

External mass (EM)	**Internal mass (IM)**	**Internal-External mass (IEM)**
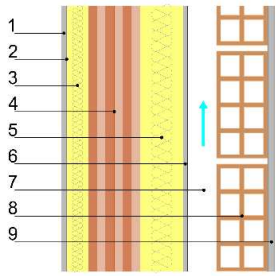	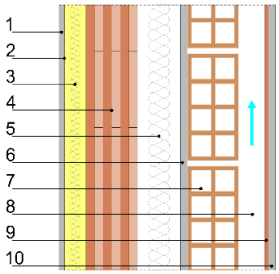	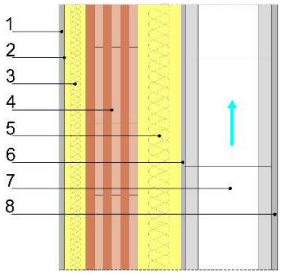
Common wall layers		
1. Internal Plasterboard 2. Vapor barrier 3. Internal insulation 4. Cross laminated timber 5. External insulation 6. Cement mortar		
VF layers		
7. Air cavity 8. Hollow brick 9. External plaster	7. Hollow brick 8. Air cavity 9. OSB panel 10. External plaster	7. Wood-concrete block with air gap 8. External plaster

The most-irradiated façade (due west) was equipped with the three ventilated skins raised from the ground by 0.3m: two massive variants of 0.8 m width and 2.3 m height and one wood-concrete blocks variant of 1 m width and 2.3 m height, built one next to the other. Two massive variants (hereinafter named EM and IM) were compared, having external and internal thermal mass with respect to the 6-cm ventilated cavity, respectively (see Table 5.2). The cavity in EM was bounded by the hollow bricks layer and the external plaster (layers 8-9 in Table 5.2), whereas that in IM was bounded by the oriented strand board (OSB) panel and the external plaster (layers 9-10 in Table 5.2). The third variant was a monolayer structure, with two 3cm-thick shells of cement-bonded wood fiber enclosing four 14-cm ventilated cavities. Having both internal and external thermal mass, this variant is hereinafter referred to as IEM. This system permits the construction of a VF on new buildings reducing drastically the economic impact compared to traditional technologies. This is possible because the IEM ventilated façade is built parallel to the supporting structure with prefabricated materials (see Figure 5.3) (wood-concrete block and fixing system certified according to DIN EN 845-1 [158]).

Figure 5.3. Wood-concrete block and fixing system (IEM VF).

For each VF, the external finishing was white plasterboard, exhibiting 0.9 emissivity and 0.6 solar reflectivity. Each VFs' side was air-tightened and sealed with XPS.
The thermal properties are collected in Table 3, following standardized calculation methods, as detailed in ISO 6946:2008[159]and ISO 13786:2008[160] and assuming strongly ventilated air cavities. As such, the U-value, the surface mass, the decrement factor, the time lag, and the periodic thermal transmittance were computed by excluding the thermal resistance of the air gap and all the following outer layers.

Table 5.3. Ventilated skins steady state and dynamic thermal parameters.

Thermal Properties	Wall Typology		
	EM	**IM**	**IEM**
Thermal Transmittance U (W/ m^2K) [a, b]	0.196	0.184	0.185
Surface mass Ms (kg/ m^2) [b]	116	206	131
Decrement Factor f [b]	0.096	0.053	0.072
Time Lag t (h) [b]	12.43	16.77	15.04
Periodic Thermal Transmittance Y12 (W/ m^2K) [b]	0.019	0.010	0.013

[a] Calculated according to ISO 6946:2008[159] U < 0.26 W/m^2K according to the Italian regulation on energy efficiency (D.M. 2015)[161].
[b] Calculated according to EN ISO 13786:2008[160], considering a well-ventilated facade by disregarding the outer layer.

5.2.2 Mechanical ventilation and sensing equipment

During the campaign, different ventilation magnitudes were tested. To exert full control on the ventilation inside the cavity, an array of 13 high-speed, PWR-controlled fans was mounted on top of each VF's cavity. By changing the applied voltage within 0-10 V, the airflow could be incremented up to 67 m^3/h and the air velocity in the gap could be modulated. A variety of sensors was deployed across the ventilated walls, indoors, and outdoors to monitor the thermodynamic variations, their impacts and their drivers. The network is displayed in Figures 5.4 and 5.5 and includes:

- a meteorological station, located 3 m away from the western façade and measuring dry-bulb temperature, relative humidity, global solar irradiation, wind speed and wind direction;
- 12 wall-plate RTDs to measure the surface temperature of each external finishing, at mid-position (115 cm above the ground), and of each internal surface overlooking the air cavity at three different heights (60 cm, 115 cm and 168 cm) on account of vertical gradients;
- wall-plate thermo-fluxmeters, on the innermost side of the ventilated cavity at 115 cm height to measure the incoming (positive) and outgoing (negative) heat fluxes. One extra flux meter was used to measure the heat transfer between the IEM VF and the existing wall;
- 3 hot-sphere anemometers placed inside the cavities at mid-height (115 cm) to track the kinetic energy of the airflow blown inside each VF.

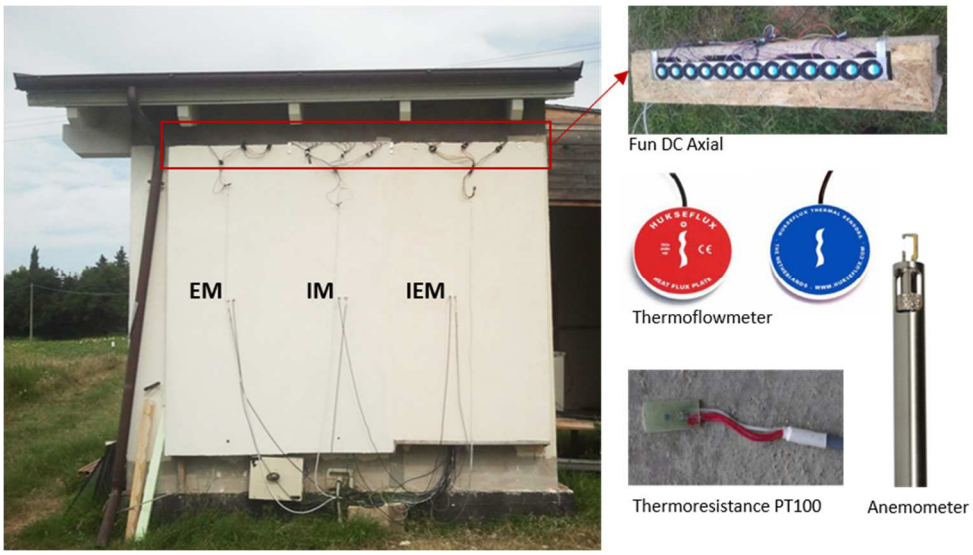

Figure 5.4. Sensors used in the experimentation.

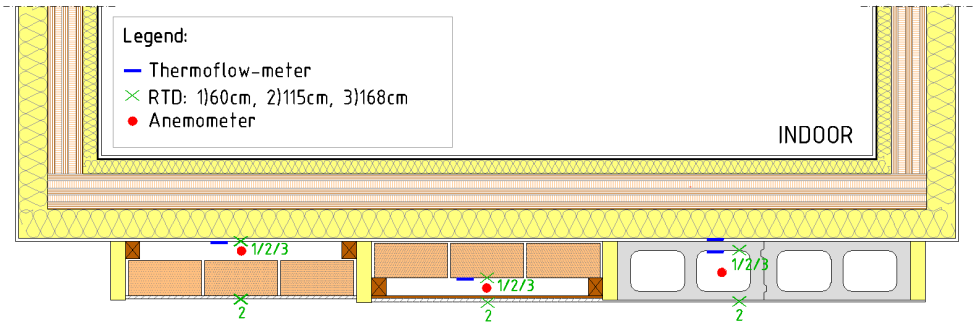

Figure 5.5. Distribution of anemometers, RTD and thermoflow-meters.

Details on manufacturers, models, accuracies, ranges and time constants of the above sensors are summarized in Table 5.4.

Table 5.4. Information about sensors used in the experimental study

Measure	Sensor type	Model	Range	Accuracy
Meteorological station				
Air temperature	Thermo hygrometer	DMA875	-30°C to +70°C	0.05°C
Relative humidity	Thermo hygrometer	DMA876	0 to 100%	0.25%
Atmospheric pressure	Piezoelettric	DQA	800 to 1100 hPa	0.5 hPa

Wind velocity	Anemometer	WMT700	0 to 75 m/s	/
Wind direction	Anemometer	WMT700	0 to 270°	/
Solar radiation	Radiometer	DPA153	0 to 2000 W/m^2	<5%
Wall sensors				
Surface temperature	Platinum resistor	PT 100	-40°C to +80°C	0.05°C
Heat flux	Heat flow meter	HFP01	-2000 to +2000 W/m²	2%
Air velocity	Anemometer	ESV107	0,01÷20 m/s	0.03 m/s

The analog (input and output) signals were digitalized via sensor-specific NI-DAQ acquisition modules and processed through a Virtual Instrument coded in LabVIEW. The sampling frequency was set at the maximum (0.1 Hz). As a first trial, we aimed at imposing a PID feedback control on the air velocity inside the cavities by modulating the voltage to the arrays of fans, individually. The dynamicity of the process turned out to exceed the sampling frequency, thus resulting in untimely and offsetted control actions. It was therefore decided to apply a daily voltage variation (from 0 to 10V) (see Figure 5.6) to collect a parameterized dataset, refined enough to conduct multivariate regression analysis. With meteorological data and air velocity in the cavity as predictive variables, we aimed at forecasting all surface temperatures and thermal fluxes for the three VFs in object.

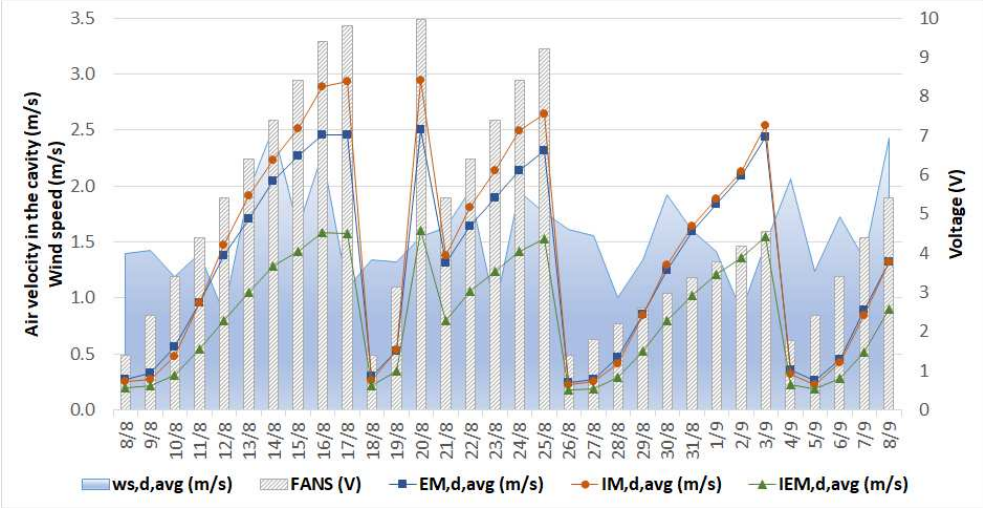

Figure 5.6. Average daily air speed in the cavity as a function of the selected voltage and average daily wind speed.

5.3 Experiments

The present Paragraph is aimed at discussing the results of the experimentation. The main goals of the experiments were the evaluation of several predictive models for temperatures and fluxes and the use of such models for the analysis of correlations between air velocity and the above-mentioned physical quantities.

5.3.1 Experiments setup

The dataset collected in the experimentation consists of 283072 samples corresponding to measurements performed in the interval August 8, 2019 - September 8, 2019 with a sampling rate of 0.1 Hz. Each sample contains measurements related to all three considered VFs in terms of:

- meteorological measurements (common to all VFs): environmental temperature, humidity, pression, irradiance, wind speed and direction
- VF-specific measurements: air velocity, surface temperature at three different heights (0.60, 1.15 and 1.68 m), external temperature and heat flux;
- timestamp of the measurement

We evaluated some regression algorithms in order to predict surface temperatures and thermal fluxes for the three VFs.
We considered two traditional machine learning algorithms and a deep learning algorithm. In particular, for what concerns the former category of algorithms, we evaluated the Regression Tree (RT) [162] and the Support Vector Regression (SVR) [163] algorithms, which respectively represent variants of Decision Tree [164] and Support Vector Machine [165] for continuous target variables. We used the versions of RT and SVM implemented in Rapidminer [116]. With respect to the latter category, we considered the Long Short-Term Memory (LSTM) algorithm [166], which is a recurrent neural network that can learn long-term dependencies among sequential data. LSTM was implemented using the Keras framework [167], which offers high-level Application Programming Interfaces (APIs) for designing deep learning algorithms in Python.
We built a different regression model for each target variable of each VF:

- VF1 (EM): T1_60, T1_115, T1_168, T1_ext, Flux1
- VF2 (IM): T2_60, T2_115, T2_168, T2_ext, Flux2
- VF3 (IEM): T3_60, T3_115, T3_168, T3_ext, T3_int, Flux3, Flux4

where the target variable Tn_y represents the temperature measured in the n-th VF at height y, Tn_ext is the external temperature and Fluxn is the heat flux measured in the n-th VF respectively. As already mentioned in Paragraph 5.2.2, we considered two different heat fluxes for VF3; we also considered the internal temperature for VF3.

We considered as features for our regression models all the other measurements: meteorological measurements, air velocity and timestamp.
We evaluated the performance of regression models by means of the root-mean-square error (RMSE), which is defined as $RMSE = \sqrt{\frac{\sum_{i=1}^{N}(y_i - x_i)^2}{N}}$, where xi is the predicted value and yi is the true (i.e., measured) value.
The generalizability of discovered models was evaluated by performing a 10-fold cross validation; the results we report in the next subsection are the averages of the 10 folds. We used a grid search in order to tune algorithms by testing different parameters' values and then we chose the values that gave the best result, namely minimal average RMSE. In particular, the ranges for each algorithm were as follows:

- RT: we considered trees with a maximal depth d ∈ [1,15] and a minimum number of samples for each node (i.e., leaf size) l ∈ [1, 10000] with 16 linear steps. Each experiment was repeated both in presence and absence of pruning techniques (p ∈ [true, false]), with the aim of evaluating the effects of pruning in reducing overfitting;
- SVR: we set the dot kernel and we trained the algorithm for a maximum number of iterations i ∈ [20, 20000] with 10 linear steps, by also varying the cost parameter C ∈ [0, 5] with 10 linear steps and the maximum error ε∈ [0.00001, 4] with 10 steps;
- LSTM: we considered single-layer architectures and we varied the number of units n ∈ {5, 10, 20, 50, 70, 100}; we trained the networks for a variable number of epochs e ∈ {5, 10, 20, 50, 100, 200, 500 }

We performed a total of 17 (target variables) x 1917 (different configurations of algorithms) x 10 (folds) = 325890 experiments, whose results are reported in the next subsection.

5.3.2 Models Evaluation

The goal of the first part of the experimentation was twofold: we were interested in both building an accurate regression model for each target variable and assessing the impact of the variation of each feature on the performance of regression models, i.e., the relative feature weights.
For what concerns the first goal, in Table 5.5 we report results of the best regression model for each target variable and regression algorithm. The value of the pruning parameter of the RT and the maximum number of iterations of the SVR are omitted, since they are constant among all the best models and are respectively equal to true and 8012.
It can be noticed that surface temperatures are better predicted by Regression Tree, while LSTM performs better on heat fluxes. In no case SVR models result to be the best predictors. As a general consideration, surface temperatures seem to be predicted more accurately than

fluxes: it may be explained by the most dynamic nature of heat fluxes, which values may be altered by turbulences.

Table 5.5. RMSE of the best regression model for each target variable (parameter values are indicated in round brackets under the RMSE).

Variable	RT	SVR	LSTM	Variable	RT	SVR	LSTM
T1_60	0.272 (d=14, l=1)	1.186 (C=0, ε=1)	0.486 (n=5, e=500)	**T3_115**	0.234 (d=15, l=1)	1.273 (C=0, ε=1)	0.469 (n=5, e=500)
T1_115	0.269 (d=15, l=1)	1.277 (C=0, ε=1)	0.502 (n=10, e=500)	**T3_168**	0.232 (d=15, l=1)	1.068 (C=0, ε=1)	0.459 (n=5, e=500)
T1_168	0.229 (d=15, l=1)	1.334 (C=0, ε=1)	0.431 (n=5, e=500)	**T3_ext**	0.724 (d=15, l=1)	3.858 (C=0, ε=2.5)	1.164 (n=20, e=500)
T1_ext	0.579 (d=15, l=1)	3.161 (C=0, ε=2.125)	1.804 (n=20, e=500)	**T3_int**	0.235 (d=15, l=1)	1.167 (C=0, ε=0.001)	0.396 (n=20, e=500)
T2_60	0.198 (d=15, l=1)	1.297 (C=0, ε=1)	0.411 (n=5, e=500)	**Flux1**	0.929 (d=13, l=650)	2.448 (C=0, ε=2.875)	0.206 (n=5, e=500)
T2_115	0.189 (d=15, l=1)	1.462 (C=0, ε=1)	0.428 (n=5, e=500)	**Flux2**	3.814 (d=14, l=1)	36.512 (C=0, ε=1)	2.586 (n=5, e=500)
T2_168	0.196 (d=15, l=1)	1.503 (C=0, ε=1)	0.394 (n=5, e=500)	**Flux3**	2.277 (d=12, l=1)	33.029 (C=0, ε=1.375)	1.426 (n=5, e=500)
T2_ext	0.707 (d=15, l=1)	4.063 (C=0, ε=2.215)	0.946 (n=5, e=500)	**Flux4**	1.055 (d=9, l=1)	13.871 (C=0, ε=2.5)	0.322 (n=20, e=500)
T3_60	0.226 (d=15, l=1)	1.032 (C=0, ε=1)	0.421 (n=10, e=500)				

It can also be noticed that the prediction of external surface temperatures is less accurate than that of the other surface temperatures, as RMSE is usually higher.

Small differences can be appreciated among VFs: in particular, regression models for VF2 have the minimum prediction error for what concerns surface temperatures, even if differences with other VFs are really small (<0.1°C).

On the contrary, models for VF2 show the worst performance in predicting heat fluxes, with RMSE 12 times higher than that of VF1. For what concerns LSTM models, it can be observed

that models with a high number of epochs and a small number of units have the best performance.
Regression models for surface temperatures are affected by low prediction errors (RMSE <0.272°C), while errors for heat fluxes are too high if we consider the range of measured values. Hence, the proposed machine learning techniques seem to be able to accurately model the physical phenomenon only in case of temperatures.
As second goal of the experimentation, we evaluated feature weights for each target variable. In particular, since we obtained the best performance in the prediction of surface temperatures, we focused on determining the physical quantities that are mostly related to their prediction. To this end, we used the best models obtained by RT. Indeed, this algorithm allows for an explicit analysis of feature weights. In particular, at each iteration the feature that minimizes the sum of squares between the actual value and the mean in each of its children nodes is selected (least squares criterion). The improvement due to each feature is used to compute its weight.
Relative weights, normalized in the range [0, 1], are reported in Table 5.6. In case of T1_ext, T2_ext and T3_ext we did not consider the air velocity inside the cavity of the VFs, since it is not related to such measurements.

Table 5.6. Relative weights for each target variable of Air Velocity (AV) inside the cavity, Air Temperature (AT), Relative Humidity (RH), Solar Irradiance (SI), Atmospheric Pressure (AP), Wind Direction (WD) and Wind Speed (WS).

Variable	AV	AT	RH	SI	AP	WD	WS
T1_60	0.249	0.227	0.140	0.125	0.093	0.082	0.082
T1_115	0.260	0.228	0.139	0.119	0.098	0.071	0.083
T1_168	0.235	0.357	0.146	0.093	0.072	0.041	0.055
T1_ext	==	0.474	0.184	0.107	0.101	0.053	0.081
T2_60	0.225	0.359	0.138	0.098	0.077	0.044	0.060
T2_115	0.227	0.378	0.127	0.102	0.069	0.039	0.056
T2_168	0.245	0.350	0.143	0.101	0.071	0.040	0.048
T2_ext	==	0.377	0.194	0.145	0.103	0.080	0.099
T3_60	0.244	0.261	0.145	0.118	0.091	0.062	0.079
T3_115	0.231	0.365	0.138	0.092	0.073	0.042	0.058
T3_168	0.242	0.361	0.140	0.086	0.074	0.040	0.055
T3_ext	==	0.417	0.194	0.130	0.101	0.072	0.085
T3_int	0.227	0.389	0.131	0.091	0.073	0.039	0.049

Generally speaking, the variation of air velocity, the temperature and the air humidity seem to have higher impact on the prediction of surface temperatures with respect to other physical

quantities. As expected, temperature usually plays a major role (weights: 0.227 ÷ 0.474) while wind direction and speed add minimal contributions (<0.1).

5.3.3 Analysis of energetic performance of VFs

As already discussed in Paragraph 5.2.2, air velocity inside the cavity cannot be kept constant through PID-controlled fans due to the high dynamicity of the process. For this reason, we used the regression models described in the previous paragraph to predict surface temperatures of the cavity by using meteorological data and constant, predefined values for air velocity in the cavity as inputs. In particular, we varied air velocity in the interval [0, 4] m/s with step 0.2 m/s and we performed an experiment for each combination of air velocity, VF and surface temperature. The goal was to find the lowest average surface temperatures for each VF.
By analyzing the obtained results, we observed that the inducted models are able to accurately forecast temperatures only for air velocity values which appear in at least 2000 samples of the initial dataset. On the basis of such hypothesis, we conducted a frequency analysis in order to evaluate acceptable values for each VF. As shown in Figure 5.7, we only considered velocities in [0.2, 2.8] m/s for EM, in [0.2, 3.2] m/s for IM and [0.2, 1.8] m/s for IEM.

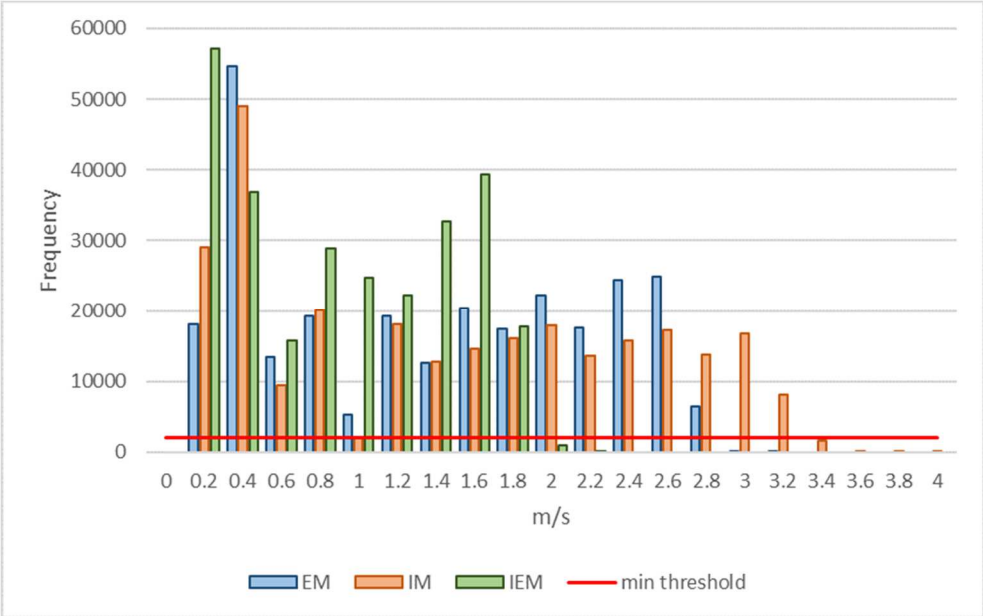

Figure 5.7. Frequency analysis of air velocities in the three VFs.

The results of the experimentation are reported in Figures 5.8, 5.9 and 5.10.

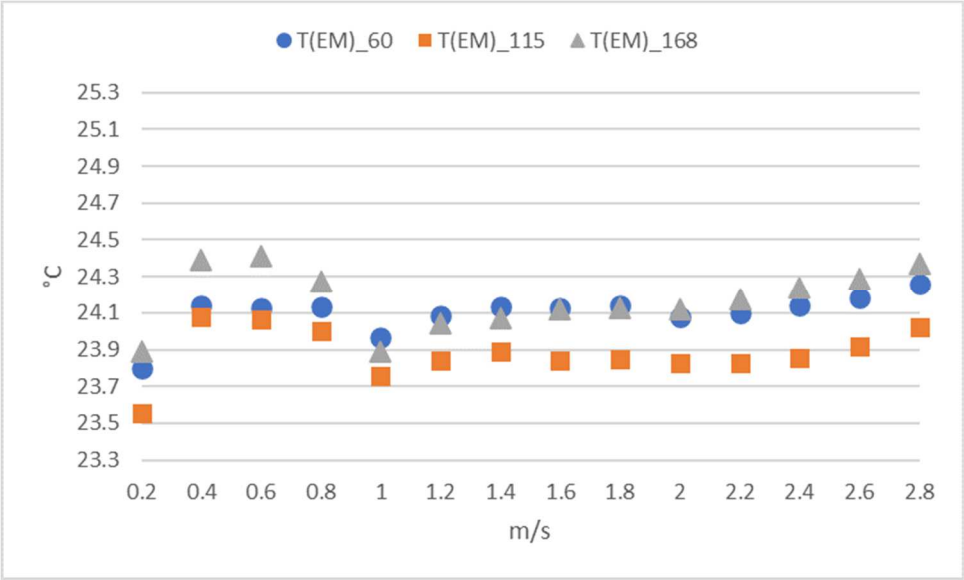

Figure 5.8. Predictions of surface temperatures for the EM wall as a function of air velocity.

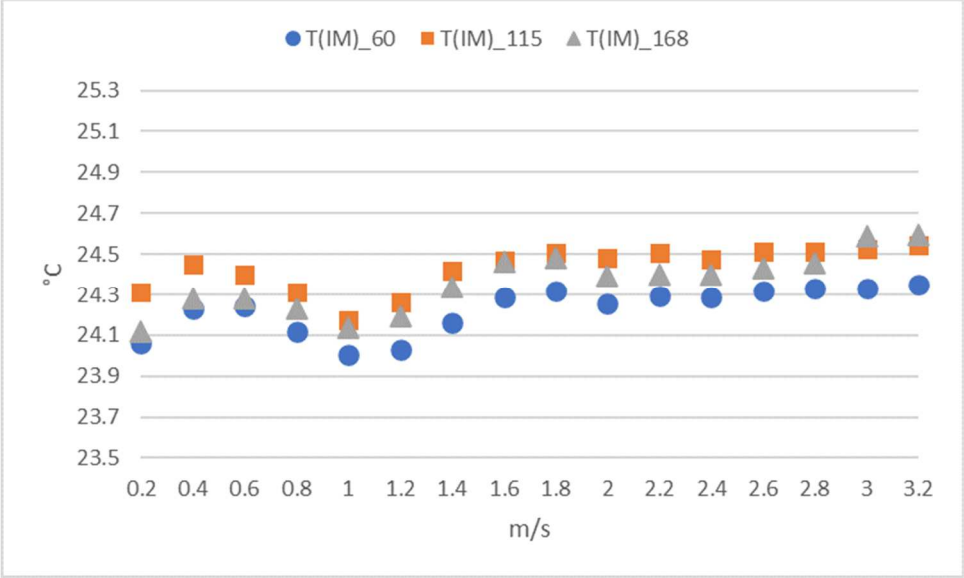

Figure 5.9. Predictions of surface temperatures for the IM wall as a function of air velocity.

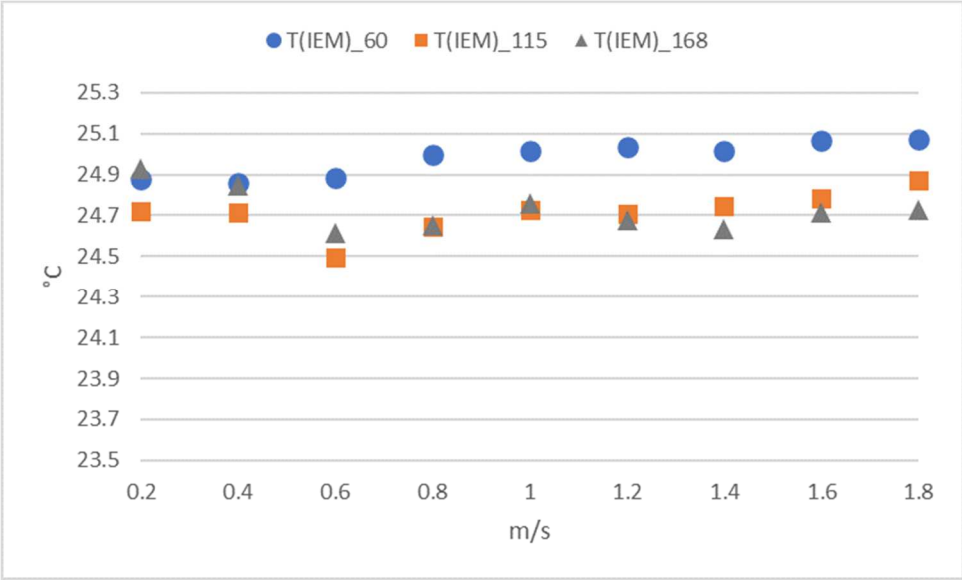

Figure 5.10. Predictions of surface temperatures for the EM wall as a function of air velocity.

In Figures 5.8 and 5.9, the VFs EM and IM show a similar trend as air velocity in the cavity varies. In fact, both have low temperature values at 0.2 m/s, probably due to the increase in thermal resistance caused by the almost stationary air layer. Such hypothesis is supported by the fact that cavities usually used in buildings typically add a thermal resistance of 0.16 m^2K/W in case of cover floors and 0.18 m^2K/W in case of façades [168]. Also in both VFs, an air velocity equals to 0.4 m/s leads to an increase in temperature of about 0.5°C for the EM façade and of 0.2°C for the IM façade, most likely caused by the intake of warm external air in the cavity (increased heat exchange by conduction) and a low convective heat exchange.

If we exclude the air velocity of 0.2 m/s, the velocity of 1 m/s seems to be the one that minimizes the surface temperatures for both the EM and IM façades. This velocity seems to represent a good compromise between convective and conductive heat exchange. Above 1 m/s, temperatures start to rise again as the air in a highly ventilated cavity is at about the same temperature as the external air [168].

Unlike the two previous façades, the IEM appears to have its absolute minimum in terms of surface temperature at a speed of 0.6 m/s (see Figure 10). In general, the air velocities reached inside this cavity are lower than the others due to both the greater roughness of the surfaces that delimit the cavity, and the greater thickness of the cavity itself (16 cm). It can also be noted that in the IEM wall the vertical temperature gradient is more important than in the two previous walls. In absolute terms, the lowest surface temperature value is the one predicted at 115cm for the VF EM (23.6°C at 0.2 m/s), while the IEM at 60 cm reaches the highest value (25.1°C at 1.8 m/s).

From the analysis of the experimental results, it can be concluded that the increase in air velocity in VFs' cavities does not necessarily lead to an advantage in terms of surface temperatures (and hence of heat fluxes). Instead, there are minima at specific velocities: 1 m/s for the VF EM and IM and 0.6 m/s for the IEM. It is also evident that the IEM wall is the least performing from an energy perspective, while the EM is the best.

5.4 Conclusion

The main goals of this work were to introduce three design variants for ventilated façades (i.e. EM, IM and IEM) and to define a new economic approach for the evaluation of the best design variant. The novelty of the approach lies in the use of a data-driven approach based on machine learning techniques for the simulation of VF temperatures and heat fluxes under different air velocities in the cavity. In particular, three different regression algorithms (i.e. regression tree, Support Vector Machine for Regression and Long Short-Term Memory) were evaluated and it was found that the regression tree has the best prediction performance in the case of temperatures, while heat fluxes are best predicted by Long Short-Term Memory networks. In general, the predictive models obtained have a high accuracy in predicting temperatures, while the accuracies are lower in the case of predicting heat fluxes. The weight of each feature of the predictive models was also studied in order to determine the most relevant thermophysical parameters. Finally, the best design variant (i.e. EM) and the optimal air velocity in the cavity were determined.
As a future direction of research, it will be interesting to evaluate further regression algorithms, in particular for the prediction of heat fluxes.

Chapter 6.
Passive solar systems and hyper-insulated buildings: Investigation of the benefits of heat recovery through controlled mechanical ventilation.

6.1 Passive solar systems in Literature

The nearly zero energy building (nZEB) paradigm has been encouraged via national plans, drawing on a variety of technical solutions. Passive solar systems proved to be a fairly effective means of achieving the target, as long as appropriately designed. Among them are the bioclimatic sunspaces.

Their twofold nature of buffer zones and solar heat collectors may lead to sizeable energy saving in the adjacent conditioned spaces [169,170].

Key element is the glazed surface, to be properly selected and oriented so as to capture the highest and longest lasting solar power while preserving the stored heat. Yet, many other parameters contribute to define the efficiency of the system, namely geometry, thermal inertia, occupancy patterns, surrounding greenery and obstacles, local weather phenomena.

Notably, tree shading, over-massing and insufficient insulation may threat the actual performance and lead to under-heating, as found in [171].

Extensive literature exists on design criteria [172–181], but when it comes to hyper-insulated buildings the energy benefit is remarkably dependent on the operating mode too.

Generally, sunspaces behave receptively and rely on radiative processes: the stored heat is transferred through the partition wall to the surface, and, from here, is gradually irradiated towards the indoor conditioned space, thus positively contributing to the wintry energy budget.

Nonetheless, when sunspaces work purely radiatively, they may lack the necessary responsiveness to promptly match the need for heat inside the building and the availability of heat inside the sunspace.

This limitation is particularly exacerbated in nZEB-type buildings, where level of insulation and thermal mass are meticulously matched with the year-round energy budget. The insertion of a bioclimatic sunspace may be ineffective or even counterproductive (higher overheating

risk) if its operation is not controllable and the heat transfer is not adjustable. Perspectives, casuistries and criticalities related to the use of sunspaces in today's construction industry are broadly discussed in [157].

The experimental study here presented was conceived to investigate the integration of a mechanically controlled ventilation system (VMC) on the partition, to complement the heat transfer with a forced convective airflow whenever convenient. A smart, automatic controller managed the air mix to avert overheating at peak hours and excessive discharge overnight.

A very limited literature exists on such a technical solution [182]: ventilation is widely, but almost solely, mentioned as a summer overheating countermeasure, operating between the sunspace and the outdoors [177–179,183]. Besides, to the best of the authors' knowledge, the VMC control optimization has never been addressed.

The investigation was conducted on a small-scale, single-room, hyper-insulated test building and the attached sunspace, whose design came out of a previous simulation-based study [184]: 132 EnergyPlus simulations were assessed, to build the most appropriate basic configuration (in terms of exposure, depth in plan, number and typology of window panes, glazed surface percentage).

The simulated energy consumption hit a low when the glazed surface percentage over the total perimeter area was between 30 % and 50 % (equal to the 55 % and the 95 % of the whole sun-exposed wall). Accordingly, the first experimentation [184] focused on the 30 % configuration and compared the purely radiative with the combined radiative-convective behaviour.

The VMC operated through an inlet hole, located close to the ceiling (at 2.5 m), and an outlet hole close to the floor (0.2 m): the control logic prioritized the activation of the fans, over the heating terminals (electric radiators), whenever the sunspace temperature (measured at the inlet height) exceeded the temperature inside the conditioned space by 2 °C.

The energy saving achieved by integrating the VMC exceeded 27 %.

Nonetheless, substantial air stratification occurred inside the conditioned space causing potentially uncomfortable vertical gradients. Also, sporadic and temporary overheating took place over consecutive sunny days. This happened because, with a fixed 2 °C threshold, the convective airflow could not be gently administered: overabundant heat was transferred indoors and stayed trapped within the very low thermal transmittance walls (0.188 W/(m^{2}K)) of the test building [185,186]. A finer control logic could have bypassed such inefficacies without eroding the energy performance.

Therefore, a second monitoring campaign was rigged up to check on both the 50 % configuration and the optimization of the VMC controller.

In the next paragraph, the experimental rig and the sensor network are thoroughly described.

6.2 Material and Method

The study was based on experimental data. Indeed, a mere simulation-based approach would have affected the reliability of the results, as spotted in even recent peer-reviewed papers [187] which claim that the deviation between simulated performances could surpass 30 % by just changing the source of the typical meteorological year in input.
The monitoring campaign took place in Central Italy (latitude 43,54°, longitude 13,37°, elevation a.s.l. 137 m, Cfa climatic conditions according to Köppen–Geiger classification [188]). The test building was constructed in an isolated position in the countryside, with unobstructed sky view around the clock.
The experienced boundary conditions ranged from cold snaps (Buran, the Siberian wind chill that hit Italy from the night of the 25th of February to the 3rd of March 2018) to mild, vernal temperatures: therefore, the sunspace behavior could be characterized under a wide range of weather conditions. The different configurations could be compared by introducing proper normalizations and performance metrics.
In the next paragraphs, the characteristics of the case study (composed by mock-up and sunspace) as well as the experimental setup are introduced and described.

6.2.1 Experimental rig

The single-room, windowless, hyper-insulated nZEB prototype thoroughly described in [157] served as case study. Its peculiar characteristics (no fenestration, double-shuttered, air-tight entry door, walls perfectly aligned with the cardinal points, meticulous treatment of thermal bridges) were meant to simplify the thermodynamics of the domain, reduce the noise detected by the sensors and isolate the contribution of the components under test.
The U-values ranged from 0.188 W/(m^2K) for the walls to 0.228 W/(m^2K) for the floor.
Heating was provided by three identical electric radiators symmetrically arranged along the east-west axis to guarantee homogeneous thermal conditions. The aggregated power was close to 1200 W.
On the south wall, opposite to the entry side, was the attached sunspace. It was built for experimental purposes, thus the construction details were designed to ease rapid modification. The balloon framing components were nailed together and to the load bearing structure, while the double-glazed façade was mechanically mounted on a wooden frame. In this way, the substitution of matte components with transparent panels was effortlessly implementable. All surfaces were waterproofed, gap-infilled with PU foam and insulating tape, and both internally and externally insulated.
The U-values ranged from 0.575 W/(m^2K) for the floor to 0.671 W/(m^2K) for the walls. The Ug-value was 1.600 W/(m^2K).

Mock-up and sunspace directly communicated via the VMC holes on the partition wall. The fans (Vortice M100/4'') required 18 W each.
Plan and elevation view of the 50 % glazed configuration are portrayed in Fig 6.1.

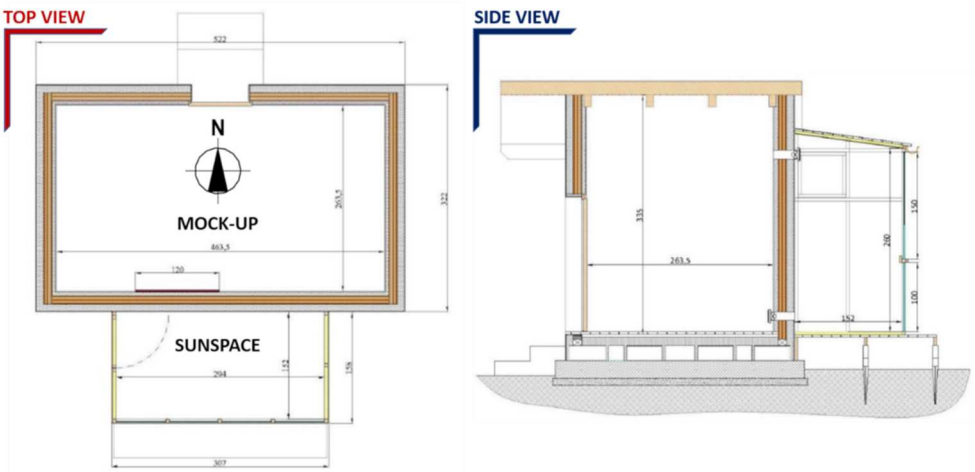

Figure 6.1. Top view (on the left side) and side view (on the right side) of the experimental rig.

6.2.2 Sense-and-Act architecture

The sensor network was designed to track the heat transfer processes occurring either outside and inside the test-rig. It comprised three main sub-sets:

- meteorological station, that measured air temperature, relative humidity, global solar radiation, wind speed and direction. The probes were connected to a dataTaker DT85. Such parameters deeply influenced the thermal balance of the coupled mock-up+sunspace system and were thus used to strike causal links and normalize the performance parameters. The station was located approximately 10 m away from the building in an undisturbed location, to truthfully depict the local climate;
- sunspace microclimate station, namely a web of surface RTDs mounted on the walls (both internally and externally) and a triplet of air RTDs hanged on the ceiling to map the air stratification at 0.6 m, 1.2 m and 1.9 m above floor level. Among them, the 1.9 m probe was used as control variable for the fans activation, given the representativeness of the convective hot updraft and the proximity to the upper hole. The probes were connected to a datalogger Elog by LSI Lastem. Reflective tape was used to shield the sensing elements from direct solar radiation.
- mock-up microclimate station, composed by a Pt100 and a hygrometer, centrally located and connected to the DT85 to monitor the comfort level inside the

conditioned area in an equally distant location with respect to the three electric radiators.

Additionally, the heating and ventilating devices were managed by means of a digital output module (NI USB 6008 by National Instruments), a static relay, a safety overheat thermostat and a power meter on the feeding line to the radiators, plus two mechanical relays utilized to switch on/off the fans and open/close the ventilation ducts.

All the probes were compliant with UNI EN ISO 7726 [189]. The technical specifications are summarized in Table 6.1.

The two dataloggers and the output module were USB-wired to a central PC were a Virtual Instrument, platformed in LabVIEW (National Instruments test and measurement software) managed the dataflow, chartered the time trends and processed the control logic. The workstation was provided with Internet connection for remote access (via TeamViewer).

Table 6.1 Sensor network general data

Measure	Sensor type	Model	Acquisition system	Rating	Position	Range	Accuracy
Mock-up microclimate station							
Air temp.	Platinum resistor	PT100	Datataker	1 min	Centre of the room - H 1.10 m	-40 °C÷ +80 °C	0.05 °C
Relative humidity	Thermo hygrometer	DME775	Datataker	1 min	Centre of the room - H 1.10 m	-30 °C÷ +70 °C	0.2 °C
Power meter	Wattmeter	S500	Datataker	1 min	Centre of the room - H 0.10 m	230-415 V	±0.5 %
Sunspace microclimate station							
Air temp.	Platinum resistor	PT100	Elog	1 min	Centre of the Sunspace - H 1.90 m	-40 °C÷ +80 °C	0.05 °C
Air temp.	Platinum resistor	PT100	Elog	1 min	Centre of the Sunspace - H 1.20 m	-40 °C÷ +80 °C	0.05 °C
Air temp.	Platinum resistor	PT100	Elog	1 min	Centre of the Sunspace - H 0.60 m	-40 °C÷ +80 °C	0.05 °C
Surface temp.	Platinum resistor	PT100	Elog	1 min	South, glazed wall (external side) - H 1.20 m	-40 °C÷ +80 °C	0.05 °C
Surface temp.	Platinum resistor	PT100	Elog	1 min	West exposed wall (external side) - H 0.80 m	-40 °C÷ +80 °C	0.05 °C
Surface temp.	Platinum resistor	PT100	Elog	1 min	South, glazed wall (internal	-40 °C÷ +80 °C	0.05 °C

					side) - H 0.50 m		
Surface temp.	Platinum resistor	PT100	Elog	1 min	South, glazed wall (internal side) - H 1.20 m	-40 °C÷ +80 °C	0.05 °C
Surface temp.	Platinum resistor	PT100	Elog	1 min	East exposed wall (internal side) - H 0.50 m	-40 °C÷ +80 °C	0.05 °C
Meteorological station							
Air temp.	Thermo hygrometer	DMA875	Datataker	1 min	Weather station	-30 °C÷ +70 °C	0,2 °C
Relative humidity	Thermo hygrometer	DMA875	Datataker	1 min	Weather station	0 ÷ 100 %	±0,25
Atmospheric pressure	Piezoelectric	DQA801	Datataker	1 min	Weather station	800÷1100 hPA	0,5 hPa
	Piezoelectric	DQA801	Datataker	1 min	Weather station	800÷1100 hPA	0,5 hPa
Wind velocity	Anemometer	WMT700	Datataker	1 min	Weather station	0 ÷ 75 m/s	/
Wind direction	Anemometer	WMT700	Datataker	1 min	Weather station	0 ÷ 270 °	/
Solar radiation	Radiometer	DPA153	Datataker	1 min	Weather station	0 - 2000 W/m^2	< 5 %

6.2.3 Phases

The VMC control was progressively refined by tuning the temperature threshold over which upper and lower fans were activated: it was halved on each occasion until incipient discomfort conditions were detected.

Indeed, the following setups were sequentially analyzed:

1 **C50_off:** 50 % glazed sunspace, with the sole heating system responsible for tracking the comfort setpoint. VMC disabled. This case served as baseline to quantify the energy saving bound to the convective heat transfer;
2 **C50_2:** 50 % glazed sunspace, setpoint tracking mandated to both the heating system and the VMC. Activation threshold set to 2 °C;
3 **C50_1**: same as case #2 with the activation threshold narrowed down to 1 °C;
4 **C50_0.5**: same as case #2 with activation threshold further decremented to 0.5 °C.

During the monitoring activity, the setpoint (SP) was adjusted to respond to sharp weather variations: it was first fixed at 20 °C in compliance with the Italian legislation [190], then, as the outdoor temperature increased by over +20 °C after the cold snap, it was incremented to observe a quite similar stress on the technical systems. However, all the tested VMC configurations worked and were compared on an equal basis (SP set to 23 °C).

We preserved the contraposition with the purely radiative setup to display some interesting secondary results, but direct comparison should not be fully trusted. Nonetheless, we collected valuable comparative information in two ways:

- by focusing on general trends and behavioral patterns (for instance the responsiveness to solar radiation swings) which do not strongly depend on the slight difference between the setpoints.
- by computing normalized consumptions and energy signatures, which are system-specific metrics, suitable to check on optimal design.

This strategy allowed to rank all the four alternatives and compare the 50% and the 30 % glazed configuration monitored in [184] too.
A process diagram is schematized in Fig 6.2.

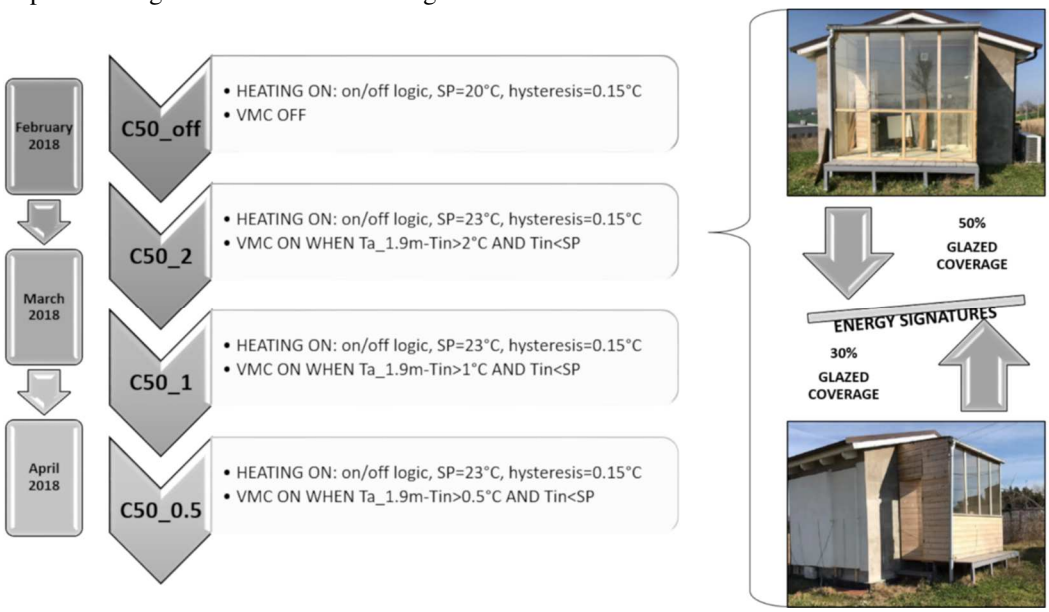

Figure 6.2. Sequence of monitoring campaigns and comparative analyses. Refer to the nomenclature and subscripts sections for codification.

6.3 Monitoring activity and comparative analysis

The monitoring campaign took place between February and April 2018. A representative period of 5 continuous days per each tested configuration was selected for comparison.
In this paragraph, the trend lines of the major parameters driving or reflecting the characteristic thermal behavior of the tested ensemble are chartered and discussed.

6.3.1 Sunspace thermal characterization

The comparative assessment was first conducted on the thermal conditions inside the sunspace at any given setup and weather combination.
This was performed by looking at:

- the heat penetration into the sunspace: solar radiation and outdoor temperature were plotted against the surface temperature of the glass (at 1.2 m above floor level) on the external and the internal side, and the air temperature at the same height, in mid-plan position. In this way it was virtually possible to follow the heat transfer across the external, glazed wall (Fig 6.3).
- the driving forces: the gap between the upper (1.9 m) and lower (0.6 m) air probes with respect to the central one (1.2 m) was plotted to represent the vertical stratification inside the sunspace and to check on the potential for up and downdrafts. Alongside, the difference between the indoor (both mock-up and sunspace) and the outdoor temperature was reported (Fig 6.4). All the thermal triggers were thus agglomerated.

By looking at the temperature profiles reported in Fig 6.3, some general considerations on the characteristic behavior of the sunspace could be drawn:

- prerequisite to operate close to full storage capacity (peak temperatures) was a very steep, yet smooth, solar radiation trend over late morning hours; conversely, intensely fluctuating morning sun (irrespectively of the daily mean irradiation) produced drastic air temperature reductions and hampered the achievement of high internal temperatures throughout the day. These oscillations were not observed in the C50_OFF configuration. This might be explained by considering that, on each convective transfer, the sunspace heat storing capacity was partially restored as the temperature dropped, enhancing the reactiveness to solar radiation swings.
- The reduction of the VMC threshold mostly impinged on the responsiveness to outdoor temperature, at equal solar radiation: with a greater thermal gap between the indoors and the outdoors (and so higher transmission losses) and a narrower thermal offset to initiate the ventilation, the sunspace experienced more frequent thermal oscillations and recharged less promptly.
- The air and the internal side of the glazed façade stayed on almost an equal thermal level. The glass just exhibited sharper peaks, being more receptive to solar radiation. The external side of the glass stabilized at an intermediate temperature between that of the inward facing side and the outdoors.
- In terms of thermal layering, a quite unexpected result was recorded: the air stratification obeyed to a positive vertical gradient (warmer air on top of the colder mass) only when no mechanical ventilation was in place. The VMC operation reversed the process. The electric radiators managed the heat supply in the morning, when the sunspace was charging at low solar angles. As long as the sunspace was

not warm enough to initiate the ventilation, the air homogenized. As the thermal gap surpassed the activation threshold around midday, the hot air was sucked by the upper fan, while the directly sunlit and more massive floor materials kept the lower air layers heated up. As a rule of thumb, the gap between 1.9 m and 1.2 m outweighed that between 0.6 m and 1.2 m, suggesting that the thermal dynamics in the upper portion of the sunspace air volume were emphasized due to the proximity to the inlet fan and the greater responsiveness to the outdoor conditions close to the ceiling.

- The snow played a role on passive solar heat collection. Indeed, the sunspace exerted a quite useless function on very overcast (solar radiation in the range 0-200 W/m^2), wintry days with temperatures approaching 0 °C, but as soon as a considerable amount of fresh snow layered on the ground (from the afternoon of February 26), the scattering properties of the surrounding materials (ground, grass, …) dramatically changed. Consequently, on the 27th, although both temperature and solar radiation went further down, the sunspace internal temperature rose above 40 °C. This is justifiably the effect on the shortwave radiation budget of the high albedo of fresh, candid snow which usually exceeds 80 % [191–193]. Snow albedo considerably decrements in case of old dirty snow - because of soot and particulate matter absorbance [194–196] - and even more with white ice since the length of the photon's travel path increases and the chances to scatter out of the snowpack slump [197]. This might explain why, on March 1, although similar boundary conditions to those of February 27 occurred, the sunspace temperature stayed below 20 °C. All things considered, this demonstrates that sunspaces may still work efficiently over snowy conditions, albeit a substantial performance uncertainty exists due to the temporal variability of snow and ice surface properties.

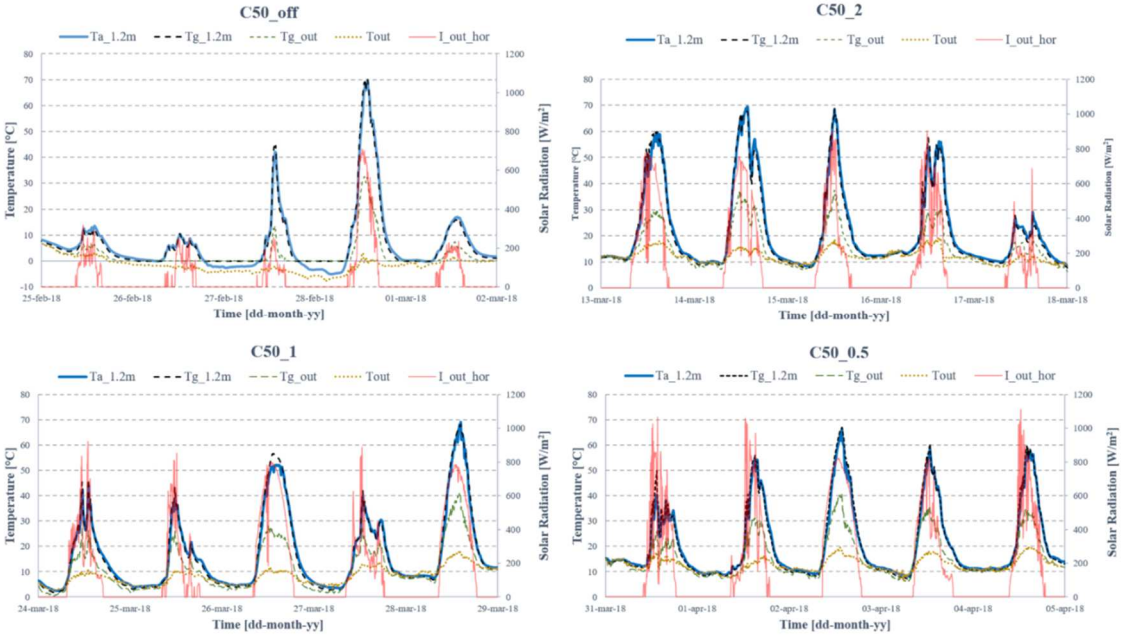

Figure 6.3. Sunspace temperature distribution against outdoor conditions.

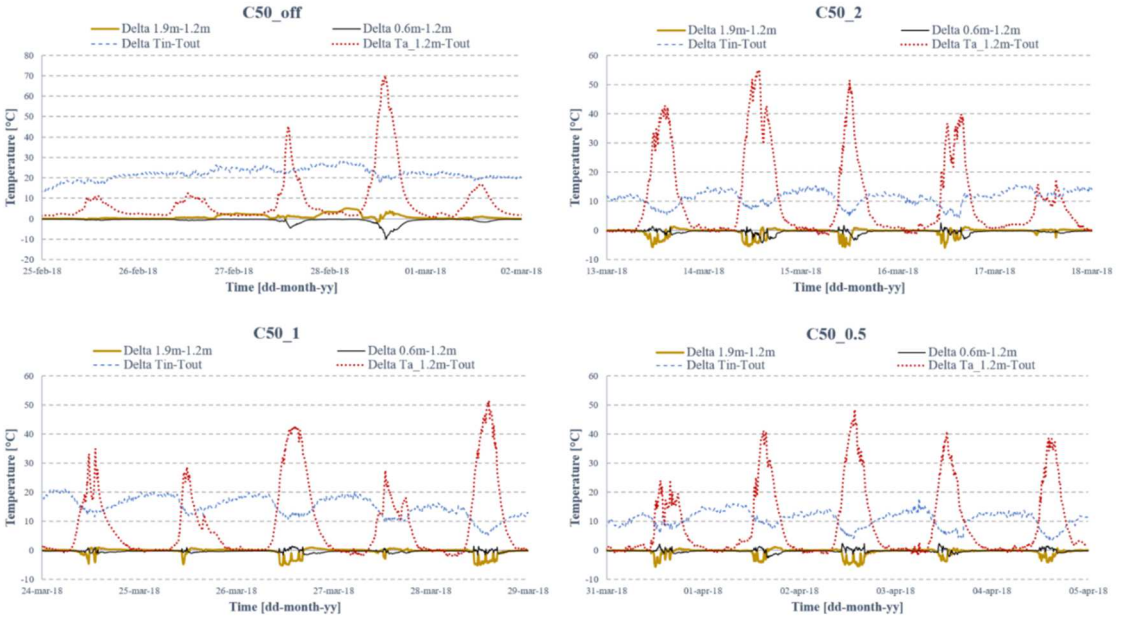

Figure 6.4. Temperature gradients that trigger the heat transfer mechanisms at stake.

6.3.2 Energy consumption

The output of the power meter was integrated over time to get the energy consumption under each tested configuration.
In view of the unequal climate conditions experienced during the four experimental runs, the comparative assessment was conducted by means of normalized parameters. Accordingly, the kWh usage was calculated and plotted against the daily average temperature difference between indoors and outdoors (termed DTm) and to the daily average solar irradiation (termed Im). The resulting charts represent the energy signatures of the mock-up+sunspace+radiators combined system (Fig 5). The trendline for each configuration is reported: given the greater order of magnitude of the DTm versus the Im angular coefficients, further investigation was conducted over the two days of maximum and minimum DTm normalized energy consumption, by looking at the radiators utilization pattern in relation to the outdoor conditions and the offset between indoor temperature and setpoint value (Fig 6). The following remarks emerged:

- under C50_off configuration (February 25 - March 1), the daily energy consumption ranged between 6.6 kWh/d and 12.1 kWh/d. The minimum was recorded over the day of lower DTm (18.4 °C on February 25) while the maximum was recorded for a combination of high DTm (22.7 °C) and low Im (147 W/m^2) on February 26. The lowest DTm and Im normalized energy consumption (0.29 kWh/°C and 0.018 kWh·m^2/W respectively) were recorded on the 28th of February: on that sunny day, the electric radiators received sparse and short calls from around 11am to 7pm, despite the very low outdoor temperatures. Conversely, on February 26, day of maximum DTm normalized energy consumption (0.53 kWh/°C), the sunspace exerted a very limited action and the radiators provided an almost continuous heat supply over the day, since the outdoor temperature steadily decreased and solar radiation barely surpassed 200 W/m^2.
- under C50_2 configuration (March 14 - March 18), the daily energy consumption ranged between 1.9 kWh/d and 3.9 kWh/d. The minimum was recorded over the day of lowest DTm (9.9 °C on March 16) while the maximum was again and expectedly recorded in concomitance with the highest DTm (13.8 °C) and lowest Im (160 W/m^2) on March 18: the electric radiators worked quite constantly at 15-minute-lasting, 3-hour-stepped duty cycles and, more importantly, the VMC never met the activation condition. Consequently, the normalized consumption peaked at 0.28 kWh/°C and 0.024 kWh·m^2/W. Conversely, on the 14th of March, the DTm normalized consumption reached a minimum of 0.19 kWh/°C: the VMC operated, almost continuously, from 10am to 3pm keeping a very stable indoor temperature, basically overlapped to the SP line. The radiators switched off around 9am and did not receive any call for heating until 8pm: thereby, between 3pm and 8pm the hyper

insulated, inertial mock-up preserved comfortable conditions by solely drawing on the heat stored in the sunspace.

- under C50_1 configuration (March 24 - March 28), the daily energy consumption ranged between 2.5 kWh/d and 5.0 kWh/d. Again, the minimum was recorded over the day of lowest DTm (11.3 °C on March 28), on which also the normalized daily energy consumptions hit their low (0.22 kWh/°C and 0.004 kWh·m^2/W), while the maximum was recorded for a combination of high DTm (15.9 °C) and – unexpectedly - high Im (519 W/m^2) on March 26, which is the day of highest DTm normalized consumption too (0.32 kWh/°C). In fact, by comparing Fig. 6 profiles over those days, it is apparent that, despite very similar solar radiation curves, the activation patterns differed because of the outdoor temperature that stayed 6/7 °C higher on the 28th. This strongly substantiated the role of outdoor temperature, which increasingly impacted on the energy efficiency of the tested ensemble with decreasing VMC activation threshold.
- under C50_0.5 configuration (March 30 - April 3), the daily energy consumption ranged between 1.2 kWh/d and 2.4 kWh/d. The minimum was recorded in presence of low DTm (10.2 °C) and medium irradiation levels (434 W/m^2) on March 31 while the maximum was recorded on the day of highest DTm (12.4 °C) and lowest Im (389 W/m^2), namely April 1. The normalized versions stayed very low and within narrow ranges (0.13-0.19 kWh/°C and 0.003-0.006 kWh·m^2/W). This happened because with such a small VMC activation threshold, the frequency of air mixing between sunspace and mock-up soared: de facto, any time a slight positive combination was detected it was immediately made available. In this way, even if the solar radiation was much more fluctuating during the day, the conditioned indoor temperature plateaued on the setpoint value almost all the day with very sporadic calls to the electric radiators.

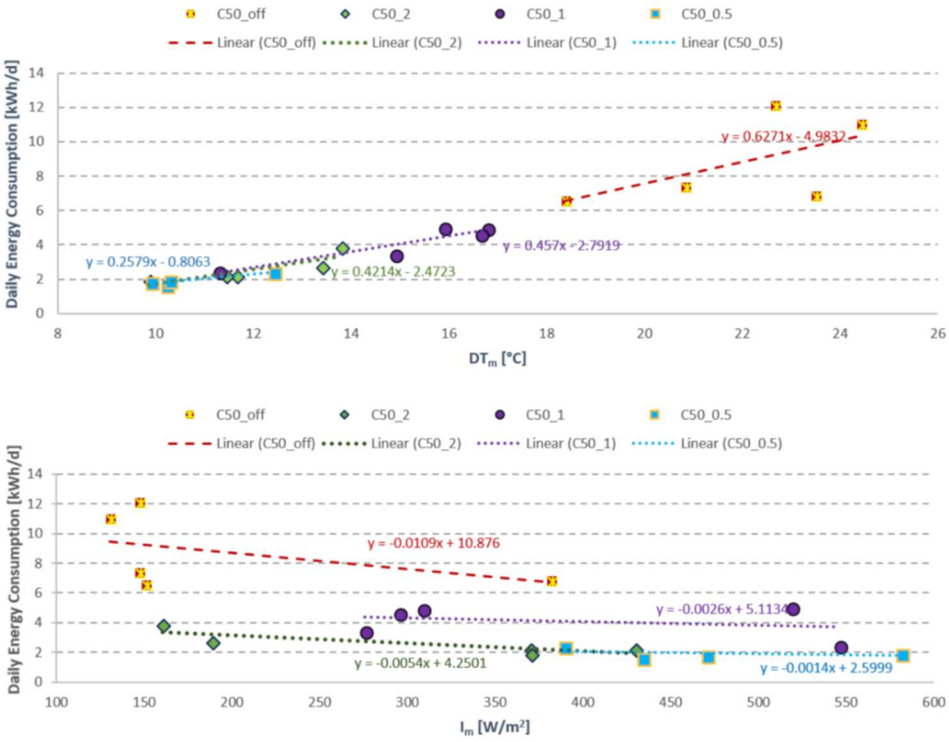

Figure 6.5. Energy signatures for the 50 % glazed sunspace

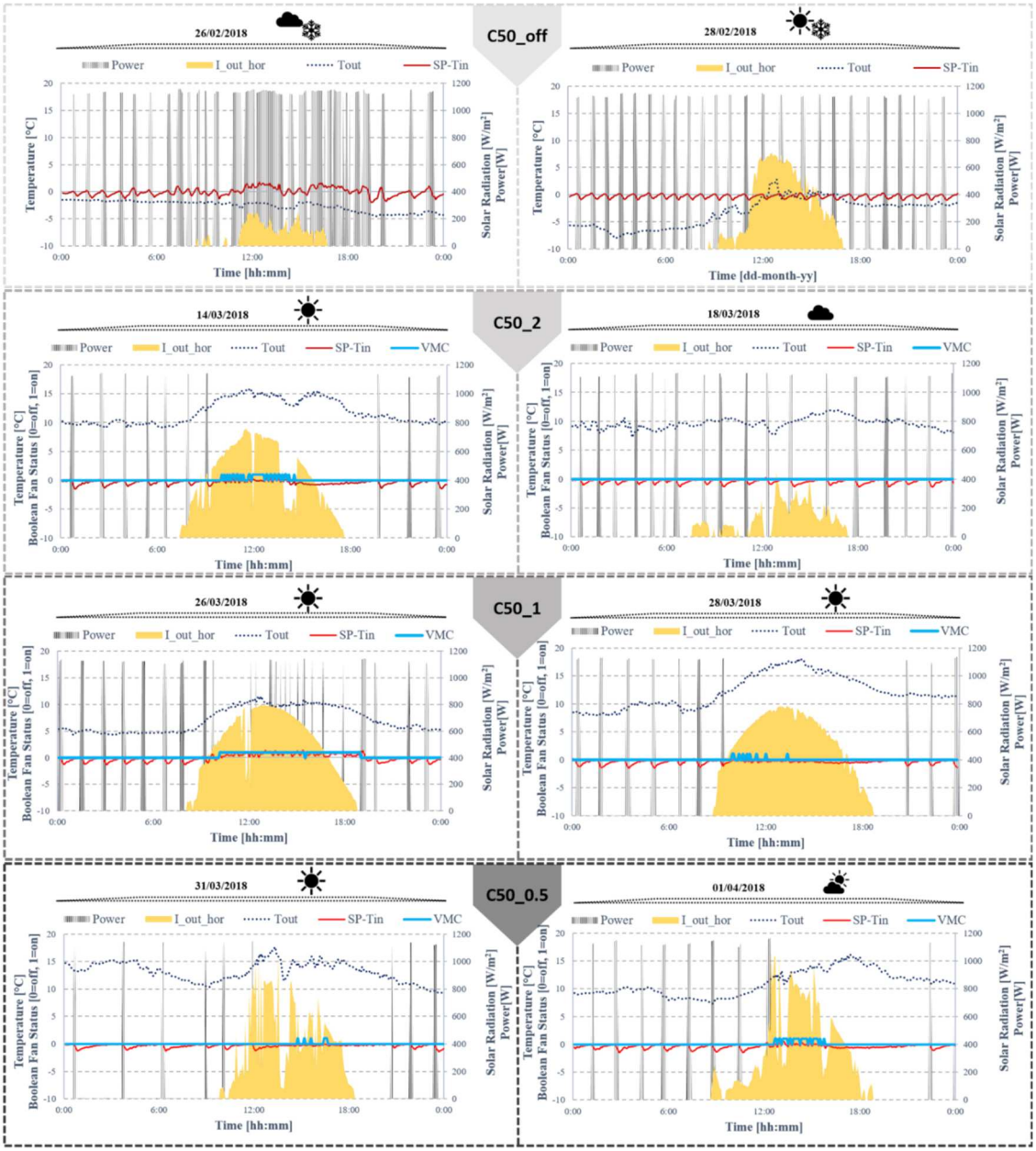

Figure 6.6. Heating and ventilating patterns over representative days in terms of energy consumption

By looking at the energy signatures some overarching conclusions on the VMC setups could be drawn:

- when the VMC threshold was halved from 2 °C to 1 °C, the dependency on the outdoor temperature did not show any sizeable inflection. Sensitivity significantly decremented only when the activation value was once more halved;
- the energy expenditure was pretty much insensitive to solar irradiation over a certain value (Im approximately 300 W/m^2) when VMC was activated. Significant differences occurred only under overcast conditions.

The DTm energy signature methodology was also used to compare the C50_2 configuration with the previously monitored C30_2 configuration [157] (glazed percentage of 30 % over the total perimeter area and 2 °C VMC threshold). The Im energy signature was excluded because of the relatively narrow solar radiation range experienced with the C30 setup.
Looking at Fig. 6.7, the energy saving attained by extending the glazed percentage was substantial: the trend line slope plummeted from 1.74 to 0.42. This demonstrated that the performance increment due to the enhanced heat storage outweighed the performance decrement related to the higher transmission losses.
Overall, the C50_0.5 was found to be the best practice.

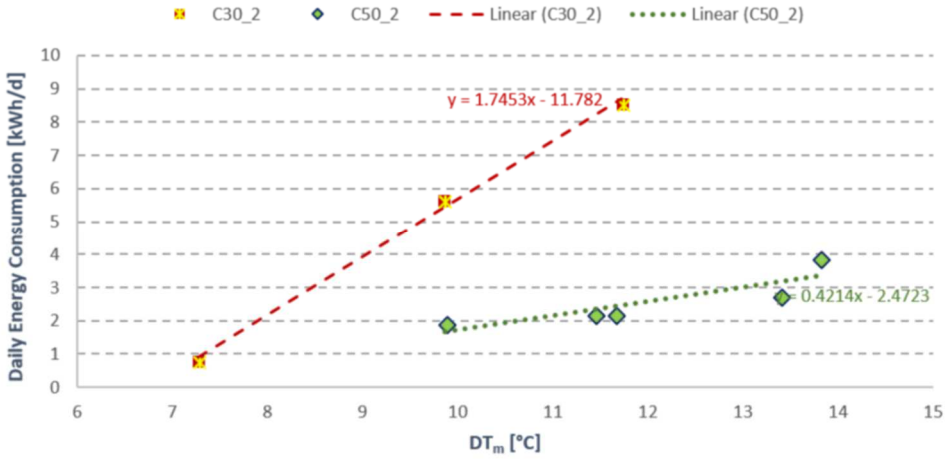

Figure 6.7. Energy signatures for the 50 % and 30 % glazed sunspace, with VMC on.

6.3.3 Indoor thermal comfort

In order to complement the energy analysis with the comfort implications, the statistical distribution of the indoor temperature around the setpoint value (SP) was assessed to verify whether the application of small activation thresholds could be counterproductive in terms of thermal overshooting.

The histograms in Fig 6.8 represent the frequency (occurrences) with which the mid-point, dry-bulb temperature in the conditioned space fell within progressively wider ranges of the setpoint. They show that:

- When the VMC complied with the 2 °C activation threshold, the 99th percentile of the offset from the SP was 1.41 °C, 0.52 °C higher than the 90th percentile. The median was 0.34 °C with an IQR of 0.47 °C. 66.1 % of the temperature records fell within the ±0.5 °C range and 2.08 % were outliers.
- When the VMC operated under 1 °C activation threshold, the 99th percentile of the SP offset narrowed down to 1.26 °C, the 90th percentile to 0.9 °C and the median to 0.23 °C. The IQR, instead, increased to 0.56 °C, while only the 63.5 % of the temperature records fell within the ±0.5 °C range with 3.06 % outliers.
- When the VMC activation threshold was 0.5 °C, the 99th percentile of the SP offset rebounded to 1.33 °C, 0.49 °C higher than the 90th percentile. The median was almost equal to that of C50_2 (0.33 °C), while the IQR was the lowest (0.44 °C). 61.3 % of the temperature records fell within the ±0.5 °C range and only 1.61 % were outliers.

Therefore, the C50_2 configuration outperformed the other setups in terms of ergonomics, since no discomfort arose both globally and locally. It should be stressed here that a more uniform distribution of the VMC holes could have achieved a better result even with stricter thresholds. A fluid dynamic study on the optimal positioning of the inlet and outlet holes should be carried out to further refine the design.

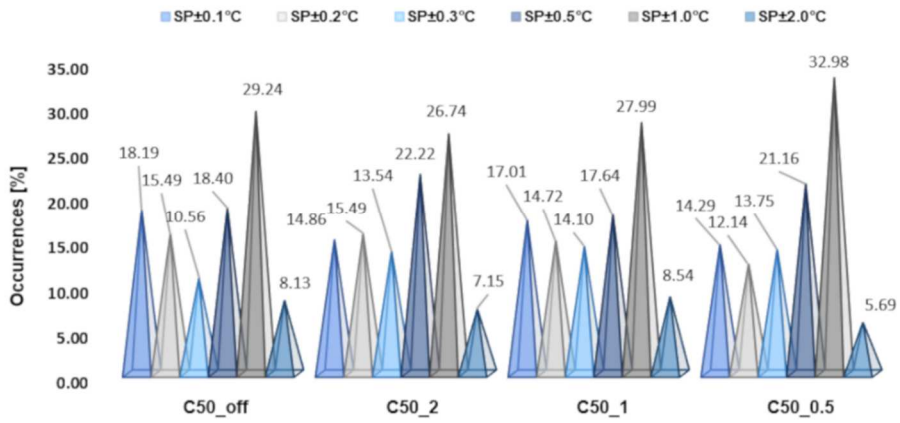

Figure 6.8. Indoor temperature distribution around the setpoint value

6.4 Conclusions

An experimental study was carried out to characterize the energy and comfort implications of coupling a hyper-insulated mock-up with a sunspace via controlled mechanical ventilation enabled between the two indoor air volumes on the basis of the reciprocal temperature difference (the activation threshold). Such value was tuned from a maximum of 2 °C to a minimum of 0.5 °C to check on the optimal setup.
The role of the glazed percentage of the sun-exposed façade was additionally investigated by merging the results from a previous monitoring campaign on the same case study [184]: 50 % and 30% configurations were compared (percentages referred to the total perimeter area). The monitoring campaign was arranged between February and April 2018 and relied on a web of meteorological and microclimatic probes distributed both outdoors and indoors and a power meter in line with the active heating system, composed by three electrical radiators. The assessment was conducted over 5 continuous days per each tested configuration.
The main results can be summarized as follows:

- in terms of energy, the 50 %, 0.5 °C activation threshold setup outperformed the other variants by achieving the lowest normalized energy consumption, with either the temperature difference between indoors and outdoors and the solar radiation as normalization terms. On average, the temperature-normalized energy consumption decreased by 36 % compared to the 1 °C threshold configuration, while the radiation-normalized energy consumption dropped by 66 %. Besides, the daily energy consumption was much less sensitive to the weather variability. The difference among 1 °C and 2 °C was relatively negligible;
- in terms of glazed percentage, the 50 % configuration substantially increased the energy saving compared to the 30 % counterpart (at equal ventilation settings) with the temperature-normalized daily consumption more than halved on average.
- in terms of comfort, the 2 °C threshold was beneficial, while narrower trigger values emphasized the tendency to overshooting. Also, the skewer distribution of the ventilation holes compared to the more uniform heat supply of the electric radiators (that were much more utilized with higher VMC thresholds) played a role. A refinement of the ventilation design could overcome the issue;
- the sunspace efficiently worked under a variety of boundary conditions: although high solar radiation was precondition to the full exploitation of the storage capacity and high outdoor temperature favored a longer lasting heat collection, a substantial rise in the sunspace temperature was recorded even on snowy days. It could be inferred that the albedo of the surrounding materials might overcome many of the applicability limits of such a passive solar system.

All things considered, this paper addresses a novel sunspace configuration, enriched with inter-communication with the indoors via thermally driven VMC.

The benefits we experimentally verified are sound and there is still room for improvement. Further research will address the VMC holes layout and the development of an alternative logic to the simple on/off logic. Given the results by [198–201] a fuzzy controller might represent the next upgrade as it proved to be a time-saving and successful control strategy in case of chaotic and/or partially subjective targets, like thermal comfort (compared to PID and bang-bang alternatives). Indeed, this approximated, mathematical-model-free logic mimics human reasoning by embracing a virtually limitless number of parameters in the decision-making process (Multiple-Input-Multiple-Output controller) through a customized set of rules. It is thus expected to better integrate all relevant parameters in the administration of the proper dosage of convective heat.

Chapter 7.
Impact of climate change on nZEBs' energy and comfort performance

7.1 Climate change in Literature

In order to limit the temperature increase to 2 °C compared to pre-industrial levels, the Fifth Assessment Report (AR5) by the Intergovernmental Panel on Climate Change (IPCC) considers four different future scenarios (RCP – Representative Concentration Pathways) which show how climate will likely change by 2100, depending on different levels of counteraction [10]. When bold mitigation strategies are taken into consideration the greenhouse gas emissions could be halved by 2050 with a maximum temperature increase of 2 °C, while, with a "business-as-usual" approach, the CO^2 in the atmosphere would increase fourfold compared to pre-industrial levels with temperature differences exceeding 4 °C. The corresponding change in global and local climatic conditions will impact the energy needs of the existing building stock and, consequently, the primary energy demand.

Speaking of buildings, two aspects are of utmost relevance: (i) the assessment of the repercussions in different geographical areas and for different uses of the built space and (ii) the development of a broad spectrum of techniques to enhance buildings' resilience and thus mitigate the energy penalty associated with climate change.

Regarding the first point, many studies in literature report on the major impact of climate change on buildings. For instance, Ciancio et al [202] compared the current energy needs of a residential building in the context of 19 different European cities, with those expected in 2080. Results show an increase in energy needs for cooling up to 272 % in Mediterranean cities, and a decrease in energy needs for heating up to 45 % in Northern European countries. In the same vein, Olonscheck et al [203] used projections of the regional statistical climate model STAR II and demonstrated that the energy demand for air conditioning in a residential building in Germany will decrease during winter, while remaining almost constant during summer for the next 40 years.

In Chile, Verichev et al [204] described how a temperature increase of 0.68 °C (under RCP2.6) and 1.51°C (under RCP8.5) will lead to a decrease of annual heating degree-days of about 72% and 92% by 2065, respectively. Moreover, Angeles et al [205] predicted an increase in energy demand of 9.6 and 23 kWh/month per person in Southern Greater Antilles and the inland of South America, which will lead to an increase of cooling loads of 7.57 GW (under RCP2.6) and 8.15 GW (under RCP8.5) by the end of the XXI century.

In general, those buildings which have extensive glass surfaces and are dominated by internal gains, i.e. offices and schools, will suffer most from the effects of climate change. According

to Frank T. [206], the cooling energy demand will soar by up to 1050% considering the RCP8.5 scenario.
In order to contribute to climate change mitigation and, at the same time, tackle the increase in primary energy demand, new buildings are expected to implement not just appropriate envelope designs [207], but also energy production systems from renewable sources, thermal and/or electrical storage systems [208] or passive solar systems [17]. Differently, several strategies will need to be introduced for existing buildings, such as: (i) installation of more efficient heating, ventilation and air conditioning (HVAC) systems [209][210], (ii) installation of adequate solar shading [206] and/or (iii) proper night ventilation [211].
At the normative level, the need to reduce global energy consumption and CO^2 emissions has induced the European Committee for Standardization (CEN) to provide an hourly dynamic calculation method that allows buildings' consumption to be assessed in a more realistic and detailed evaluation, especially during the summer season[94]. This method, described in EN ISO 52016-1:2017[5] replaces the one described in ISO 13790:2008[26] by introducing a new methodology to calculate energy needs for heating and cooling both on an hourly and monthly basis.
This study aims at assessing the impact of climate change on (i) the heating and cooling consumption of an nZEB multi-family house, located in Rome and designed according to the most recent Italian regulations [11], and (ii) the level of comfort achieved indoors.
To this purpose, hourly dynamic simulations were performed in TRNSYS according to the following procedure: (i) production of current and 2050 meteorological input files, (ii) simulations and evaluation of the year-round energy consumption assuming an infinite power system for heating and cooling, (iii) simulations and evaluation of the free-floating operative temperature assuming no heating/cooling systems, (iv) application of the adaptive comfort [12] theory to rate the quality of the indoor environments and (v) evaluation of long-term thermal comfort [13].
As such, the proposed analysis contributes to:

- a better understanding of the most effective energy retrofit strategies for existing nZEB buildings in Mediterranean climate to guide future legislative amendments;
- the identification of which mitigation policies will be most appropriate for new buildings to limit both CO^2 production and global energy consumption.

7.2 Methods

In this work, the dynamic simulation software TRNSYS [7] was chosen to assess the thermal behavior of a building located in Rome (classified as nearly zero energy building (nZEB) according to the Italian regulation in force) on hourly basis. The focus is on the effects of the expected climate change and urban heat island exacerbation by 2050, both in terms of energy needs and comfort.

7.2.1 Climate and geographical data

The hourly climate data of the typical year adopted in this study refer to both the current climate conditions and those in 2050. About future scenarios, two Representative Concentration Pathways (RCPs) were analyzed, which refer to climate change projections developed in the AR5 report by IPCC.
The two future projections (RCP8.5 and RCP4.5) compute the expected temperature rise as a function of different greenhouse gases emissions produced by both human activities and different mitigation activities implemented by local policies:

- RCP8.5 represents a 'business-as-usual' approach, which considers that atmospheric concentrations of CO^2 will triple or quadruple by 2100 compared to pre-industrial levels, thus increasing the air temperature by about 4°C.
- RCP4.5 contemplates control measure to curtail the greenhouse emissions, assuming a trend reversal (decrease below current levels) by 2070. Consequently, the atmospheric concentrations of CO^2 will be about twice as high as pre-industrial levels by 2100. The increase in air temperature will be capped at 2°C.

Therefore, three typical annual weather data were retrieved from Meteonorm 7.3 [8]: (i) current climate conditions, (ii) 2050 - RCP8.5 climate conditions , (iii) 2050 - RCP4.5 climate conditions.
The current climatic data are developed on a data set of temperatures and solar irradiances measured between 2000-2009 and 1991-2009, respectively; while future scenarios are simulated through ERA-Interim / UrbClim [14]. This model shows that Rome is the location with the highest temperature increase in Italy, as a consequence of the climate change and the urban heat island effect; therefore, this city was chosen as case study for the present study.
In order to perform simulations through TRNSYS, the following input data were considered: (i) latitude, (ii) dry-bulb external temperature, (iii) relative humidity, and (iv) solar global irradiance on the horizontal plane. Data were provided by the WMO weather station #162390 located in Rome/Ciampino. At 41.8°N (latitude), 12.58°E (longitude) and 131 m above sea level (altitude), the location features a temperature climate, specifically Csa (Mediterranean hot summer climate) in accordance with the Köppen–Geiger climate classification system.

7.2.2 Trnsys' model simulation

TRNSYS is a well-established building dynamic simulation software worldwide, capable of fine assessments of both energy and comfort levels [212].
Outdoor air temperature, relative humidity and global solar irradiance on the horizontal plane for each of the three different scenarios described in Paragraph 7.2.1 were provided as inputs

through TRNSYS' component Type 9. Then, these data were transferred to Type 16c, a solar radiation processor which implements Reindl and Perez 1990 models to obtain beam and diffuse solar irradiances on horizontal and tilted surfaces, respectively. The virtual model of the nZEB case-study was designed through a SketchUp plugin for creating the multi-zone building envelope (TRNSYS3d) [213], and then, provided as input in TRNSYS [214]. An interface for the detailed TRNSYS multi-zone building (TRNBuild/Type56) was used for modelling walls, gains and ventilation profiles. In order to comply with the Italian regulation for nZEBs [11], overhangs were integrated to reduce solar gains, therefore, Type 34 was used. The results in terms of energy needs and indoor operative temperatures were plotted via Type 65. Figure 7.1 displays the flowchart.

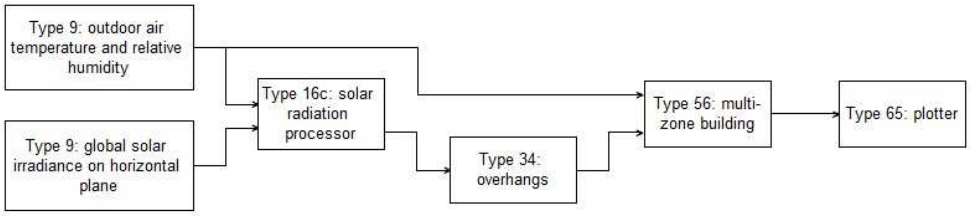

Figure 7.1. TRNSYS simulation model flowchart

7.2.3 Case-study

The studied building is a new 3-floor residential nZEB, composed by two apartments per floor. Each apartment has an open space that combines kitchen and living room, a double bedroom, a single bedroom and a bathroom, as shown in Figure 7.2. Table 7.1 summarizes geometrical features of each apartment.

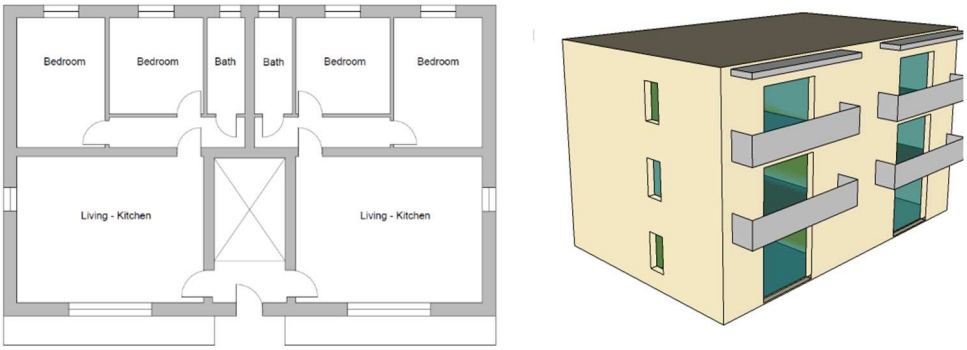

Figure 7.2. Analyzed building: building plan (1:200) and South-West view.

Table 7.1. Geometrical features of the apartment.

	Unit	Value
Net floor area	m^2	63.73
Net height	m	2.70
Net volume	m^3	172.07
Window-to-wall ratio	%	15

In order to comply with the Italian nZEB requirements the building envelope is made of 2 cm of external plaster, 35 cm of pored bricks, 4 cm of external insulation, and 1 cm of internal render. The 24 cm hollow-core concrete slab of the flat and non-walkable roof is well insulated with 10 cm of expanded polystyrene. The stairwell wall is made of two layers of 12 cm hollow bricks separated by 6 cm of insulation and external plaster, while the partition wall between the two apartments is a cavity wall with two layers of 12 cm of hollow bricks and external plaster. Windows are double glazed with low emissivity glass. Horizontal overhangs on south-exposed facades and proper shading devices on all the windows are modelled in order to provide sufficient sunlight control and reduction of solar gains. The thermo-physical parameters of the main building envelope elements, previously described, are given in Table 7.2 while in Table 7.3 the nZEB requirements for the Italian territory are described.

Table 7.2. Thermo-physical parameters of building envelope elements.

	Termophysical parameter	Unit	Value
External wall	Thermal transmittance (U)	W m-2K-1	0.30
	Internal areal heat capacity (k1)	kJ m-2K-1	41.70
	External areal heat capacity (k2)	kJ m-2K-1	19.00
	Periodic thermal transmittance (Yie)	W m-2K-1	0.013
	Time shift (Δt)	h	17.72
Stairwell wall	Thermal transmittance (U)	W m-2K-1	0.30
	Internal areal heat capacity (k1)	kJ m-2K-1	44.90
	External areal heat capacity (k2)	kJ m-2K-1	44.90

	Periodic thermal transmittance (Yie)	W m-2K-1	0.048
	Time shift (Δt)	h	13.48
Separating wall between two apartments	Thermal transmittance (U)	W m-2K-1	0.59
	Internal areal heat capacity (k1)	kJ m-2K-1	45.00
	External areal heat capacity (k2)	kJ m-2K-1	45.00
	Periodic thermal transmittance (Yie)	W m-2K-1	0.148
	Time shift (Δt)	h	11.58
Roof	Thermal transmittance (U)	W m-2K-1	0.27
	Internal areal heat capacity (k1)	kJ m-2K-1	65.70
	External areal heat capacity (k2)	kJ m-2K-1	7.40
	Periodic thermal transmittance (Yie)	W m-2K-1	0.037
	Time shift (Δt)	h	11.53
Window	Thermal transmittance (U)	W m-2K-1	1.80
	Solar heat gain coefficient (SHGC)	-	0.71

Table 7.3. Standard nZEBs energy assessment for the considered case studies

	Unit	
Energy performance indicator for heating (EPH,nd)	[kWh/m^2]	5.32
Energy performance indicator for cooling (EPC,nd)	[kWh/m^2]	28.60
Global average heat transfer coefficent (H't)	[Wm^2/K]	0.37
Equivalent solar area/Floor area (Asol,est/Asup,utile)	-	0.013

According to the Italian technical specifications in UNI/TS 11300 [215], the following assumptions were made: usage profiles 24/24h, internal heat gains rate at 5.72 W/m^2 and ventilation rate at 0.5 h-1.
Two different models of the building were created:

- the first one equipped with an infinite power system for heating and cooling, to evaluate the energy consumption. In this case, the operative temperature, used to control the system, was set to 20°C in winter and 26°C in summer, in accordance with the type of building and categories identified in UNI EN 16798-1 - Annex A [12], assuming category II as reference.
- the second one equipped without any heating and cooling system, to allow free-floating operative temperature for the assessment of thermal comfort. The level of thermal comfort was analysed through two different approaches. Firstly, we applied the adaptive method, according to which the operative temperatures are compared to the indoor operative temperature ranges defined in UNI EN 16798-1 - Annex A [12] for buildings without mechanical cooling systems to identify different comfort levels as a function of the outdoor running mean temperature, calculated as follows:

$$\boldsymbol{\theta_{rm} = (1 - \alpha) \cdot \{\theta_{ed-1} + \alpha \cdot \theta_{ed-2} + \alpha^2 \theta_{ed-3}\}} \quad (7.1)$$

In Eq. 7.1, α is a constant between 0 and 1 (recommended value is 0.8) and θed-i is the daily mean outdoor air temperature on the i-th previous day.
Secondly, we calculated a newly proposed long-term comfort index (Eq. 7.2). It outperformed other six types of existing indices (23 total) found in standards and five types of new indices (36 total) for comfort assessments in the long run in a recent comparative study [13] . The correlation with the long-term thermal satisfaction of building occupants was based on continuous thermal comfort measurements and post-occupancy evaluation surveys, yet in air-conditioned office buildings. Despite the different casuistry, this combined index proved to better take into account the triggers behind long-term comfort, namely pronounced excursions beyond some acceptable temperature range and large variations in daily temperature than the average experience over time [13]. As such, it is worth investigating its expected variation in future scenarios. This combined, normalized percent index is calculated as follows:

$$\boldsymbol{index} = \left(\frac{\%\text{ To outside specified ranges} + \%\text{To daily range} > \text{a threshold}}{2}\right) \quad (7.2)$$

In this study, the hourly operative temperature range was set between 20°C and 26°C, in accordance with the type of building and categories identified in UNI EN 16798-1 - Annex A [12], assuming category II as reference, and the daily threshold was set to the 80th percentile of the entire simulated database.

7.3 Results

In this paragraph the modelling results are illustrated and discussed. They refer to the two apartments at the second floor of the building described in Paragraph 7.2.3. Considering the dispersing surface of the roof, the second floor is the most responsive to external climatic variations.

7.3.1 Simulations to assess the energy consumption

Based on dynamic hourly simulations, the average annual increase in outdoor temperatures (+3.4°C under RCP4.5 and +3.9°C under RCP8.5) was found to enhance the global energy consumption from 5079 kWh*year (in 2020) to 6196 kWh*year (+18.0%) and 6248 kWh*year (+18.7%) by 2050, respectively. The breakdown in heating and cooling needs revealed a divergent trend (see Table 7.4): the heating energy needs showed a decrease in the order of 129.5% (RCP4.5) and 185.8% (RCP8.5), whereas the cooling energy needs increased by 47.8% (RCP4.5) and 50.3% (RCP8.5).
This trend was reflected in terms of maximum hourly peak power too: that of the heating system dropped from 2.5 kW to 1.9 kW, while that of the cooling system rose from 3.0 kW to 4.0 kW (RCP8.5).

Table7.4. Air temperature (Tair), relative humidity (UR), horizontal global solar irradiance (Ig,H), heating energy needs (φh,tot), cooling energy needs (φc,tot), peak power for heating (φh,max) and peak power for cooling (φc,max) for the three analyzed scenarios.

Year	Tair (°C)	UR (%)	Ig,H (kWh/m^2)	φh,tot (kWh)	φc,tot (kWh)	φh,max (kW)	φc,max (kW)
2020	15,8	74,4	160,3	2390,7	2688,4	2,5	3,0
2050 (RCP4.5)	19,2	70,1	188,7	1041,8	5153,8	2,0	3,8
2050 (RCP8.5)	19,7	69,0	188,8	836,4	5411,9	1,9	4,0

By performing a frequency distribution analysis of hourly energy demand (see Figure7.3), an increase of about 6% was showed for the 1÷2 (light blue) kWh and 2÷3 kWh (blue) cooling ranges for both future scenarios; while a decrease of about 8% was showed for the 1÷2 kWh (orange) heating range. Moreover, for both future scenarios the 2÷3 kWh (red) heating range disappeared, the 3÷4 kWh (black) cooling range was introduced and the 0÷1 kWh (yellow) heating range remained unchanged.
In addition to the increase in cooling energy demand, the number of hours over which the cooling system was active incremented too: from 3033 h in 2020 to 3983 h (+23.8%) and

4022 h (+24.6%) under RCP4.5 and RCP8.5 scenarios, respectively. Indeed, the length of the cooling season (calculated from the first to the last day the system was on) varied for the different scenarios: 174 days in 2020, 224 in 2050 (RCP4.5) and 208 in 2050 (RCP8.5). At the same time, the percentage of hours over which the conditioning system stayed off was found to be higher under RCP4.5 rather than RCP8.5 (25.9 % and 19.5 %, respectively).

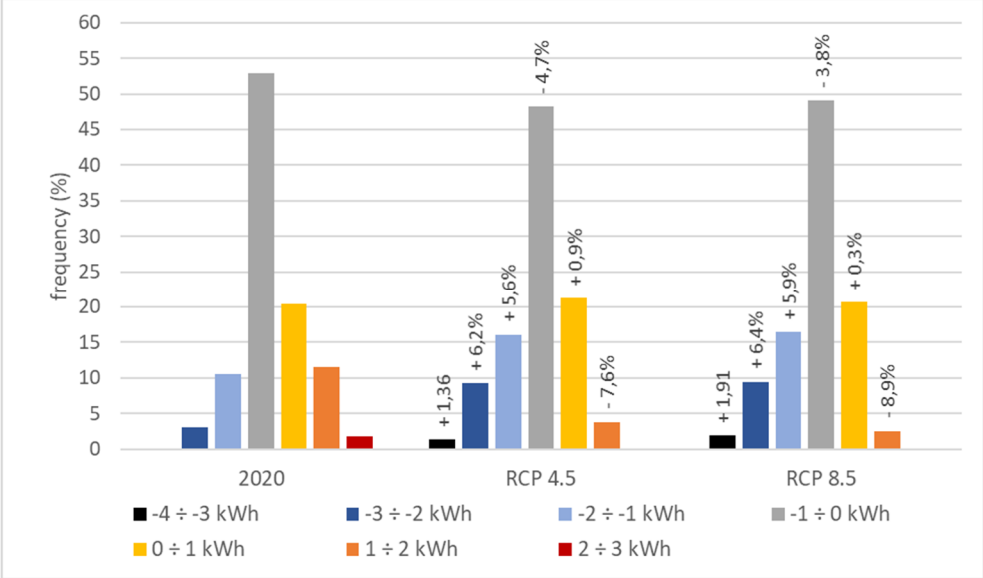

Figure 7.3. Frequency distribution of energy needs for heating and cooling. Negative ranges refer to cooling, positive to heating.

In addition to the increase in temperature, the model ERA-Interim/UrbClim [14] provides also an increase in global solar irradiance on the horizontal plane (Ig,H), thus, on tilted and oriented surfaces. As shown in Figure 7.4, an evident increase in global solar irradiance was observed for both future scenarios compared to 2020, resulting in an increase in solar gains, especially during the months of October, November and December given that the presence of movable shading devices was considered during summer months only as per year-round nZEB requirements [11].

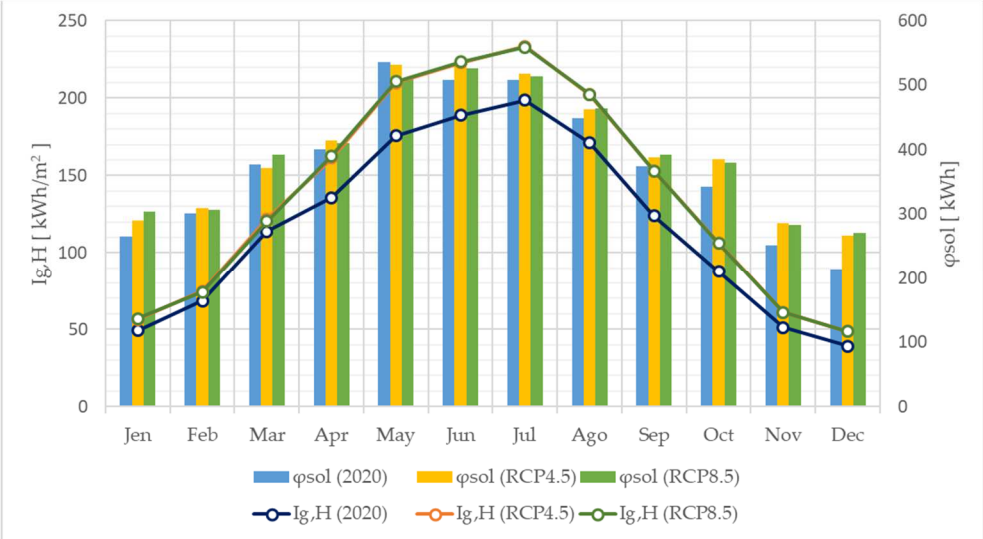

Figure 7.4. Monthly sum of solar gains (φsol) and solar global irradiance on the horizontal plane (Ig,H) for 2020, 2050 (RCP4.5) and 2050 (RCP8.5).

The average annual percentage of global solar irradiance on the horizontal plane was found to increase (see Table 7.5) by about 19.7% and 15.5% for the cooling period (May - October) and the heating period (November - April), respectively, for both future scenarios. Figure 4 and Table 7.5 show that the average monthly solar gains did not increase in summer between 2020 and 2050, due to movable shading devices operating in summertime only. Assuming equal internal gains and ventilation rates, the increase in average summer energy consumption accounting for 249.3% (+2463.4 kWh) and 293.5% (+2723.5 kWh) under RCP4.5 and RCP8.5, respectively, was ascribable to the corresponding average temperature increase (2.7 °C and 3.2°C). Likewise, the decrease in average winter consumption accounting for 70.3% (-1350.9 kWh) and 77.0% (-1554.3 kWh) under RCP4.5 and RCP8.5, respectively, was associated to the average temperature increase (2.1°C and 2.5°C).

Table 7.5. Monthly percentage variation of the main input and output values between 2020 and RCP4.5 and RCP8.5 (2050) scenarios.

2020 vs 2050 (RCP4.5)						2020 vs 2050 (RCP8.5)					
mtly	**Tair**	**Ig,H**	**φsol**	**φh**	**φc**	**mtly**	**Tair**	**Ig,H**	**φsol**	**φh**	**φc**
Jen	54%	14%	9%	-54%	-	**Jen**	59%	16%	15%	-59%	-
Feb	38%	9%	3%	-48%	-	**Feb**	46%	8%	2%	-58%	-
Mar	24%	7%	-1%	-68%	-	**Mar**	28%	6%	4%	-78%	-
Apr	26%	19%	4%	-100%	-	**Apr**	27%	20%	2%	-100%	-
May	15%	20%	-1%	-	161%	**May**	16%	20%	-5%	-	157%
Jun	15%	18%	5%	-	70%	**Jun**	17%	18%	4%	-	75%
Jul	20%	18%	2%	-	64%	**Jul**	22%	17%	1%	-	72%
Ago	21%	18%	3%	-	75%	**Ago**	24%	18%	3%	-	85%
Sep	20%	23%	4%	-	161%	**Sep**	23%	24%	5%	-	184%
Oct	15%	21%	12%	-	965%	**Oct**	19%	21%	11%	-	1188%
Nov	21%	20%	14%	-96%	-	**Nov**	25%	20%	13%	-100%	-
Dec	33%	24%	24%	-55%	-	**Dec**	39%	24%	26%	-67%	-

By performing a correlation analysis between daily heating/cooling needs and outdoor air temperatures (see Figure 7.5), we observed how future distributions gradually shift towards higher temperatures and consumptions: from a maximum cooling demand of 40.4kWh/day in 2020 to 64.3kWh/day under RCP4.5 and 68.0kWh/day under RCP8.5. Precisely for this reason, the distribution in graphs b and c of Figure 7.5 loses symmetry and the density of the points in the left side (heating needs) decreases. Figure 7.5 also shows that the minima (φh/c = 0) of the trendlines for future scenarios (graph b and c) narrow down and get slightly shifted towards higher temperatures (to 16.0°C and 16.5°C respectively), compared to the current scenario (graph a) where 0 φh/c conditions occur between 14.5°C and 16.6°C.

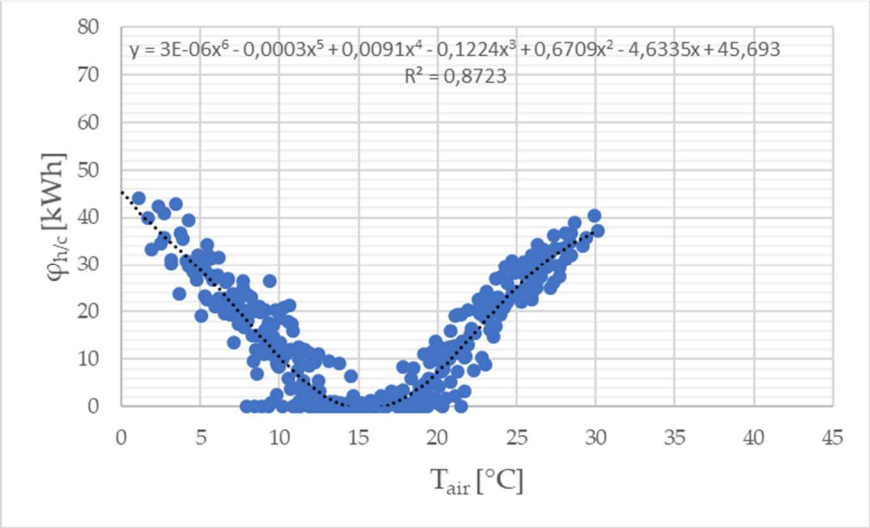
y = 3E-06x⁶ - 0,0003x⁵ + 0,0091x⁴ - 0,1224x³ + 0,6709x² - 4,6335x + 45,693
R² = 0,8723
φh/c [kWh]
Tair [°C]
0
10
20
30
40
50
60
70
80
0
5
10
15
20
25
30
35
40
45

(a)

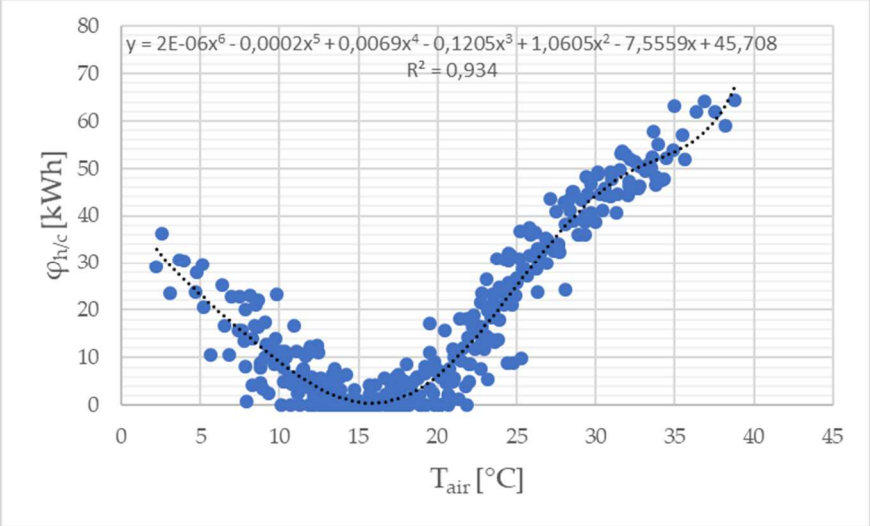
y = 2E-06x⁶ - 0,0002x⁵ + 0,0069x⁴ - 0,1205x³ + 1,0605x² - 7,5559x + 45,708
R² = 0,934
φh/c [kWh]
Tair [°C]
0
10
20
30
40
50
60
70
80
0
5
10
15
20
25
30
35
40
45

(b)

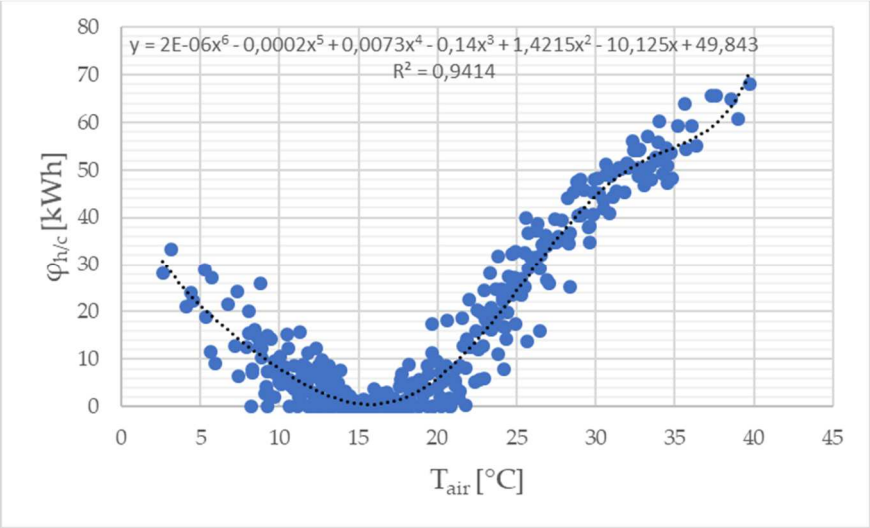

(c)

Figure 7.5. Correlation between daily energy demand of the building and outdoor air temperature: (a) 2020 current scenario, (b) future scenario 2050 RCP4.5 and (c) future scenario 2050 RCP8.5. Trendlines, respective polynomial equations and R-squared are reported on each graph.

7.3.2 Simulations to assess thermal comfort

In this paragraph the two approaches followed for the assessment of indoor thermal comfort are sequentially presented: (i) adaptive method and (ii) combined long-term index proposed by Li et al. [13].

The assessment of adaptive comfort can be performed only on buildings used mainly for human occupancy engaged in sedentary activities (e.g. residential buildings and offices), where thermal conditions can be regulated by occupants through accessing operable windows and adapting their behavior. On the other hand, the new combined index considers the long-term thermal satisfaction in response to pronounced excursions and daily variability.

The analysis was performed for two rooms (see Figure 7.6): one due south-east (living room) and one due north-west (double bedroom) to account for different exposures and thus different solar gains. The evaluation focused on the cooling periods as identified in Paragraph 7.3.1: 174 days in 2020, 224 in 2050 (RCP4.5) and 208 in 2050 (RCP8.5), therefore, the assessment of thermal comfort is performed for each climate scenario over different periods, assuming the absence of cooling systems.

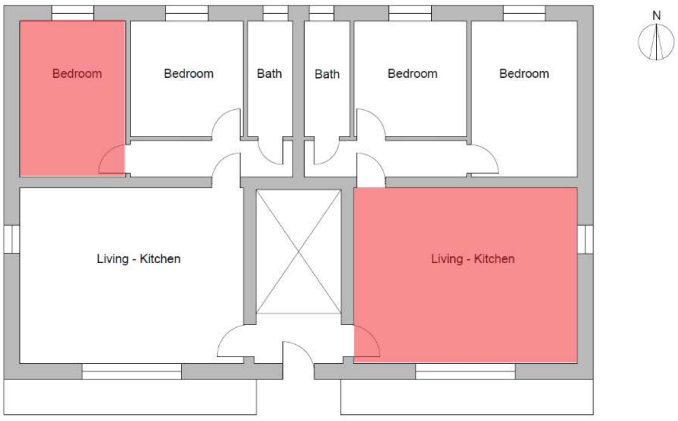

Figure 7.6. Representative rooms for adaptive comfort assessment: south-east living room and north-west double bedroom.

Regarding adaptive method, as shown in Table 7.6, the living room provided comfort conditions (operative temperature cooling set point of 26°C) for shorter time periods than the double bedroom, regardless of the scenario. Assuming category II as reference, the percent decrease between 2020 and 2050 RCP4.5 reached 4.1% and 3.7% for the two considered rooms, against 9.0% for both rooms under RCP8.5.

Table 7.6. Adaptive comfort assessment for the two analysed rooms under different climate scenarios: comfort hours and percentages over the relevant cooling periods.

Year	Cooling period			Room	Cat. I		Cat. II		Cat. III	
	data	days	h		h	%	h	%	h	%
2020	May 6th - Oct 26th	174	4176	Living room	681	16,3%	1091	26,1%	1566	37,5%
				Bedroom	1266	30,3%	1883	45,1%	2169	51,9%
2050 (RCP4,5)	Apr 6th - Nov 15th	224	5376	Living room	733	13,6%	1186	22,1%	1788	33,3%
				Bedroom	1840	34,2%	2223	41,4%	2422	45,1%
2050 (RCP8,5)	Apr 6th - Oct 30st	208	4992	Living room	513	10,3%	855	17,1%	1299	26,0%
				Bedroom	1184	23,7%	1800	36,1%	2035	40,8%

Results for the combined index are shown in Table 7.7. The double bedroom experienced a percent increase of discomfort events of 0.9% and 3.6% between 2020 and 2050 RCP4.5 and RCP8.5, respectively. In contrast, for the living room the variation stayed below 1 % under both the considered scenarios.

Table 7.7. Combined index assessment for the two analysed rooms under different climatic scenarios: percentages over the relevant cooling periods.

Year	Cooling period			Room	Combined discomfort index
	data	days	h		%
2020	May 6th - Oct 26th	174	4176	Living room	56.1%
				Bedroom	47.9%
2050 (RCP4,5)	Apr 6th - Nov 15th	224	5376	Living room	55.0%
				Bedroom	48.8%
2050 (RCP8,5)	Apr 6th - Oct 30st	208	4992	Living room	55.9%
				Bedroom	51.5%

7.4 Discussion and conclusions

Achieving a long-lasting nZEB performance represents one of the greatest opportunities to save energy and reduce greenhouse gases emission in the building sector. For this reason, every EU Member State has defined a long-term strategy to support the retrofitting and construction of new residential and non-residential buildings, to achieve a decarbonised and highly energy efficient building stock by 2050 [216]. However, in the meantime, the global climate is undergoing major upheavals, posing a serious risk of premature obsolescence on current nZEB paradigms. In Italy, according to the ERA-Interim/UrbClim model [14], the city which will undergo the greatest temperature increase by 2050 is Rome: a rise of 3.4°C and 3.9°C by 2050 is predicted under RCP4.5 e RCP8.5 scenarios respectively,. In order to assess the impact of climate change on heating and cooling energy needs and on comfort in nZEBs in Rome, a multi-family building, designed in compliance with the Italian regulations in force, was challenged on the basis of the afore mentioned future projections. Simulation results of the building equipped with both heating and cooling systems, show a decrease of the heating needs in the order of 129.5% (-1349 kWh) and 185.8% (-1555 kWh), and an increase of the cooling needs of about 47.8% (+2466 kWh) and 50.3% (+2724 kWh) under RCP4.5 e RCP8.5 assumptions, respectively, compared to current values. Cumulatively and as a result of the different lengths of the cooling and heating seasons, the annual energy needs will increase by +18.0% and +18.7%. Indeed, for both future scenarios the increase in cooling needs will outweigh that in heating needs, owing to (i) the higher number of hours over which the air conditioning system is turned on (+23.8% and +24.6%) and (ii) the higher peak power demand. The concomitance of these two aspects inevitably translates into a substantial increase in the electric energy demand for powering the cooling systems, therefore, in an increase in greenhouse gas levels in countries that still largely rely

on fossil fuels, Italy included. Peak electricity demand is especially worrisome since it is usually covered by low-efficiency power plants, yet it is strongly associated with typical nZEB paradigms. In fact, while air conditioning is only a fraction of all building energy uses, it is the primary driver of peak electricity demand [217]. Efficiently curbing the air conditioning needs by targeting a resilient nZEB design will be key in the future.

According to the ERA-Interim/UrbClim model, by 2050 not just temperatures will rise, but a 19.7% increase in global solar irradiance on the horizontal plane is also to be expected during summer months, thus, triggering higher solar gains. This study considers the presence of movable shading devices during summer, which are necessary to comply with national nZEB regulations. In the considered case study, these systems appear rather effective since the increase in solar gains is negligible in summer, but becomes evident in winter. By performing simulations in the absence of cooling systems, a 6.2% and 5.1% decrease in the hours of adaptive comfort is determined under RCP4.5 (2050) and RCP8.5 (2050) scenarios out of the concerted action of temperature and solar gains. Results for the newly proposed combined index for long-term comfort assessments revealed a milder future penalty. The index estimates how the level of occupant adaptation and sensitivity to variation would be affected in the future. It was demonstrated that the comfort implications of pronounced excursions and large variations in daily temperature will be marginal under both scenarios, with higher influence on north-west rather than south-east oriented thermal zones, likely owing to the combination of higher temperatures and higher solar irradiation in levelling out the daily swings.

This study adds to the current body of knowledge on the preservation of the nZEB performance in the future by performing hourly dynamic simulations on a reference building in Rome modelled in accordance to the latest legislations. It quantifies potential changes in terms of energy and comfort levels and provides useful recommendations to legislators on building standards both for the design of new nZEBs, e.g. the presence of solar shading devices, and for the renovation of the existing building stock. Further analysis may target climate dependencies and may include technological variants.

Chapter 8.
Concluding Remarks

In order to achieve a zero-carbon building stock by 2050 according to the Paris agreement, the European Commission's latest Energy Performance of Buildings Directive (EPBD) defines a list of actions to be followed by Member States in order to minimise energy consumption. These actions can be summarised in six points: (i) energy efficiency of the building envelope on new and existing buildings, (ii) use of innovative building materials and solutions, (iii) microclimate control, (iv) use of high-efficiency electric heat pumps or other carbon-free systems, (v) smart controls (home automation) and (vi) digitisation for a better energy efficiency policy.

The research activities conducted during the PhD and the topics developed in this thesis are mainly related to the topics listed in the first three points of the above-mentioned list.

Energy codes make it easy and economical to check the minimum requirements for energy performance of buildings defined by different countries in order to reduce energy consumption, limit dependence on fossil fuels and combat climate change. In Chapters 3 and 4, two calculation methods recently published in different standards by the European Committee for Standardization (CEN) are analysed: EN ISO 52016-1:2017 "Energy demand for heating and cooling, indoor temperatures and sensible and latent heat loads - Part 1: Calculation procedures" and EN ISO 52010-1:2017 "Outdoor climatic conditions - Part 1: Conversion of climatic data for energy calculations". Both standards, being of recent publication, are not well reflected in the literature in terms of validation, so a comprehensive analysis is performed in order to understand the potential and limitations of both.

EN ISO 52016-1:2017 while being a powerful tool for the prediction of hourly energy requirements, shows three important criticalities: the heat transfer model of opaque elements, the use of constant values of the thermal transmittance of transparent elements and the use of constant values of the solar transmittance coefficient. Two alternative models to that proposed by the standard are therefore introduced and tested: one concerning the discretisation of the opaque elements in which the number and position of the capacitive nodes and resistive layers varies according to the thermophysical characteristics of the real layers of the opaque component, and the other, concerning the calculation of the solar transmittance coefficient (ggl) which varies from hour to hour according to the angle of incidence of direct solar radiation. Both proposed methods lead to an improvement of the standard, in particular the one concerning ggl. The new method for heat transfer of opaque

elements is found to have a slightly lower absolute error (RMSE) and relative error (CVRMSE), while the new method for calculating ggl improves the RMSE of summer solar loads by 46.7% compared to the method proposed in the standard. The improved estimation of solar loads allows for an improved calculation of summer demand.

EN ISO 52010-1:2017, directly linked to EN ISO 52016-1:2017, provides an hourly methodology for the calculation of direct and diffuse radiation on each surface starting from the global horizontal radiation. This standard was tested through a comparative analysis of four different calculation algorithms, including one proposed by the undersigned, on five European cities characterised by different climatic conditions (Stockholm, De Bilt, Paris, Rome and Malaga). Taking the Trnsys algorithm as a basis (Reindl 1990-Perez 1990), the results show that the direct and diffuse irradiance on oriented vertical surfaces calculated with the proposed method (Boland and Ridley 2007/Liu and Jordan 1960), obtains the closest values to Trnsys. The annual sum of the hourly irradiances also shows that the algorithm of EN ISO 52010-1:2017 (Erbs 1982/Perez 1990) while showing values of diffuse irradiance on vertical surfaces similar to the other models, underestimates the annual direct irradiance on south, west, east and north facing surfaces by -24.2% (115 kWh/ m2 year), -55.9% (281 kWh/ m2 year), -0.9% (6 kWh/ m2 year) and -69.4% (30 kWh/ m2 year) respectively. The proposed model is therefore a good alternative to the method of EN ISO 52010-1:2017.

In conclusion, by applying some improvements to the calculation codes recently published by CEN, it is possible to obtain very good results in terms of hourly prediction of the energy needs of buildings, with a lower computational cost compared to major simulation software such as Trnsys or Energy Plus. Such predictions are fundamental both in the design phase and in the verification of minimum requirements in order to minimise consumption, achieve NZEB performance and decarbonise the construction sector by 2050.

Another area where EPBD can intervene to reduce greenhouse gas emissions is the use of innovative building materials and solutions. For this reason, two experimental analyses are presented in chapters 5 and 6, one concerning the use of ventilated façades to reduce summer needs and electricity consumption, and the other concerning the use of bioclimatic spaces integrated with controlled mechanical ventilation to reduce winter needs and electricity and/or fossil fuel consumption. Both proposals can be applied to new and existing buildings.

Ventilated façades have been extensively studied in the literature and are an excellent solution in terms of energy savings, but through simple analysis of the data collected in the experimental phase it is difficult to understand which air velocity is most appropriate to optimise the system. For this reason, three different prototypes of ventilated façades integrated with a mechanical ventilation system were evaluated in the mock-up and a new approach for the evaluation of the best variant was defined using machine learning

techniques. In particular, three different regression algorithms (i.e. Regression Tree, Support Vector Machine for Regression and Long Short-Term Memory) were evaluated and it was found that the Regression Tree has the best prediction performance in the case of temperatures, while heat fluxes are better predicted by Long Short-Term Memory networks. In general, the predictive models obtained have a high accuracy in predicting temperatures, while the accuracies are lower in the case of predicting heat fluxes. By using the created predictive models, it was possible to identify the best variant and the optimal air velocity in the cavity.

Another innovative construction solution proposed is the experimental study where a sunspace with controlled mechanical ventilation was coupled to a hyper-insulated building. Having a very resistive building, the heat of the sunspace was transferred to the thermal zone through the movement of two volumes of air activated whenever the temperature difference of the two environments was 2°C, 1.5°C, 1°C or 0.5°C. The results show that the optimal configuration in terms of normalised consumption and energy saving of the system is the configuration where the glass surface of the sunspace is equal to 50% of the façade and the VMC is activated at 0.5°C. In terms of indoor comfort, the most advantageous activation threshold was 2°C, while narrower activation values emphasised the tendency to overshoot. This problem could be overcome by optimising the design of the ventilation system.

Finally, Chapter 7 assesses the impact of climate change on the heating and cooling energy demand and comfort of nZEBs built in compliance with current requirements. In Italy, according to the ERA-Interim/UrbClim model, Rome is the city that will suffer the highest temperature increments by 2050 with an increase of 3.4°C and 3.9°C respectively in the RCP4.5 and RCP8.5 scenarios and a 19.7% increase in global solar radiation on the horizontal plane during the summer months. The results obtained from the simulations carried out show a decrease in the heating demand in the order of 129.5% (-1349 kWh) and 185.8% (-1555 kWh), and an increase in the cooling demand of about 47.8% (+2466 kWh) and 50.3% (+2724 kWh) respectively under the RCP4.5 and RCP8.5 scenarios, compared to the current values. Overall, as a result of the different length of the cooling and heating seasons, annual energy demand will increase by +18.0% and +18.7%, with adaptive comfort hours decreasing by 6.2% and 5.1% under the RCP4.5 (2050) and RCP8.5 (2050) scenarios.

The studies reported in this thesis add to the current body of knowledge regarding calculation models and construction solutions to improve the energy efficiency of buildings and decarbonise the construction sector, today responsible for around 40% of global climate-altering gas emissions.

References

[1] United nations, Nationally determined contributions under the Paris Agreement, 2021.

[2] International Energy Agency (IEA), Net Zero by 2050, Paris, 2021. https://www.iea.org/reports/net-zero-by-2050.

[3] European Parliament, Council of the European Union, Directive (EU) 2018/844 of the European Parliament and of the Council of 30 May 2018 amending Directive 2010/31/EU on the energy performance of buildings and Directive 2012/27/EU on energy efficiency, Off. J. Eur. Union. 30 May (2018) 1–17.

[4] International Energy Agency (IEA), Building Envelopes, 2021. https://www.iea.org/reports/building-envelopes.

[5] International Organization for Standardization, ISO 52016-1:2017 - Energy performance of buildings - Energy needs for heating and cooling, internal temperatures and sensible and latent heat loads -- Part 1: Calculation procedures, 2017.

[6] International Organization for Standardization, ISO 52010-1:2017 Energy performance of buildings — External climatic conditions — Part 1: Conversion of climatic data for energy calculations, 2017.

[7] M.J. Duffy, M. Hiller, D.E. Bradley, J.W. Werner Keilholz, TRNSYS 17: A transient system simulation program, (2013). https://sel.me.wisc.edu/trnsys/features/features.html.

[8] Meteotest, Meteonorm 7 V7.3.3, (2018). https://meteonorm.com/en/.

[9] European Commission, Energy efficiency in building, (2020). https://ec.europa.eu/info/news/focus-energy-efficiency-buildings-2020-feb-17_en.

[10] R.K. Pachauri, L.A. Meyer, IPCC, 2014: Climate Change 2014: Synthesis Report. Contribution of Working Groups I, II and III to the Fifth Assessment Report of the Intergovernmental Panel on Climate Change, Geneva, Switzerland, 2014. https://doi.org/10.1017/CBO9781139177245.003.

[11] Ministero dello sviluppo economico, Italian iterministerial decree 26th June 2015: Application of calculation methods for energy performance and definition of minimum building requirements, Off. Gazzette Ital. Repub. N°39 15th July 2015. (2015) 1–8. https://www.mise.gov.it/images/stories/normativa/DM_requisiti_minimi.pdf.

[12] CEN European Commitee for Standardization, EN 16798-1:2019 Energy performance of buildings - Ventilation for buildings - Part 1: Indoor environmental input parameters for design and assessment of energy performance of buildings addressing indoor air quality, thermal environment, lighting and acous, 2019.

[13] P. Li, T. Parkinson, S. Schiavon, T.M. Froese, R. de Dear, A. Rysanek, S. Staub-French, Improved long-term thermal comfort indices for continuous monitoring, Energy Build. 224 (2020) 110270. https://doi.org/10.1016/j.enbuild.2020.110270.

[14] Flemish Research & Technology Organisation VITO., Urban Climate Service Centre, (n.d.). www.urban-climate.be.

[15] S. Summa, G. Remia, C. Di Perna, Comparative and Sensitivity Analysis of

Numerical Methods for the Discretization of Opaque Structures and Parameters of Glass Components for EN ISO 52016-1, Energies. 15 (2022). https://doi.org/10.3390/en15031030.
[16] S. Summa, L. Tarabelli, C. Di Perna, Evaluation of ISO 52010-1: 2017 and proposal for an alternative calculation procedure, Sol. Energy. 218 (2021) 262–281. https://doi.org/https://doi.org/10.1016/j.solener.2021.02.046.
[17] G. Ulpiani, S. Summa, C. di Perna, Sunspace coupling with hyper-insulated buildings: Investigation of the benefits of heat recovery via controlled mechanical ventilation, Sol. Energy. (2019). https://doi.org/10.1016/j.solener.2019.01.084.
[18] S. Summa, L. Tarabelli, G. Ulpiani, C. Di Perna, Impact of climate change on the energy and comfort performance of nzeb: A case study in Italy, Climate. 8 (2020) 1 – 16. https://doi.org/10.3390/cli8110125.
[19] European Commission, Council Directive 93/76/EEC (Save), 1993.
[20] United nations, Kyoto protocol to the united nations framework convention on climate change, 58 (2008). https://doi.org/10.51663/pnz.58.2.07.
[21] European Commission, Directive 2002/91/EC of the European Parliament and of the Council of 16 December 2002 on the energy performance of buildings, 2002. https://doi.org/10.5040/9781782258674.0021.
[22] European Parliament, Directive 2010/31/EU of the European Parliament and of the Council of 19 May 2010 on the energy performance of buildings (recast), Off. J. Eur. Union. (2010).
[23] European Commission, Directive 2012/27/EU of the European Parliament and of the Council of 25 October 2012 on energy efficiency (EED), 2012.
[24] CEN European Commitee for Standardization, EN 832:1998 - Thermal performance of buildings and building components, 1998.
[25] CEN European Commitee for Standardization, EN ISO 13790:2004 - Thermal performance of buildings - Calculation of energy use for space heating, 2004.
[26] CEN European Commitee for Standardization, EN ISO 13790: 2008 Energy performance of buildings - Calculation of energy use for space heating and cooling, (2008).
[27] S. Laurent, Il nuovo metodo orario dinamico per il calcolo dei fabbisogni dell'edificio nel nuovo pacchetto EPBD, Ingenio. (2019). https://www.ingenio-web.it/23568-il-nuovo-metodo-orario-dinamico-per-il-calcolo-dei-fabbisogni-delledificio-nel-nuovo-pacchetto-epbd.
[28] CEN European Commitee for Standardization, EN ISO 52000-1:2017 Energy performance of buildings — Overarching EPB assessment — Part 1: General framework and procedures, 2017.
[29] E. Arumagi, T. Kalamees, Design of the first net-zero energy buildings in Estonia, Sci. Technol. Built Environ. 22 (2016) 1039–1049.
[30] P.M. Congedo, C. Baglivo, D. D'Agostino, I. Zacà, Cost-optimal design for nearly zero energy office buildings located in warm climates, Energy. 91 (2015) 967–982.
[31] M.C. Falvo, F. Santi, R. Acri, E. Manzan, Sustainable airports and NZEB: The real case of Rome International Airport, in: 2015 IEEE 15th Int. Conf. Environ. Electr. Eng., 2015: pp. 1492–1497.
[32] M. Krarti, P. Ihm, Evaluation of net-zero energy residential buildings in the MENA region, Sustain. Cities Soc. 22 (2016) 116–125.

[33] Z. Zhou, L. Feng, S. Zhang, C. Wang, G. Chen, T. Du, Y. Li, J. Zuo, The operational performance of “net zero energy building”: A study in China, Appl. Energy. 177 (2016) 716–728.
[34] N. Bajenaru, A. Damian, R. Frunzulica, Evaluation of the energy performance for a nZEB office building under specific climatic conditions, Energy Procedia. 85 (2016) 26–34.
[35] N. Kampelis, K. Gobakis, V. Vagias, D. Kolokotsa, L. Standardi, D. Isidori, C. Cristalli, F.M. Montagnino, F. Paredes, P. Muratore, others, Evaluation of the performance gap in industrial, residential \& tertiary near-Zero energy buildings, Energy Build. 148 (2017) 58–73.
[36] E. Arumägi, T. Kalamees, Design of the first net-zero energy buildings in Estonia, Sci. Technol. Built Environ. 22 (2016) 1039–1049.
[37] J.P. González, C. Yousif, Prioritising energy efficiency measures to achieve a zero net-energy hotel on the island of Gozo in the central Mediterranean, Energy Procedia. 83 (2015) 50–59.
[38] A. Tejero-González, M. Andrés-Chicote, P. Garc\'\ia-Ibáñez, E. Velasco-Gómez, F.J. Rey-Mart\'\inez, Assessing the applicability of passive cooling and heating techniques through climate factors: An overview, Renew. Sustain. Energy Rev. 65 (2016) 727–742.
[39] S.B. Sadineni, S. Madala, R.F. Boehm, Passive building energy savings: A review of building envelope components, Renew. Sustain. Energy Rev. 15 (2011) 3617–3631.
[40] G. Murano, E. Primo, V. Corrado, The effect of glazing on nZEB performance, Energy Procedia. 148 (2018) 320–327.
[41] S.-G. Yong, J.-H. Kim, Y. Gim, J. Kim, J. Cho, H. Hong, Y.-J. Baik, J. Koo, Impacts of building envelope design factors upon energy loads and their optimization in US standard climate zones using experimental design, Energy Build. 141 (2017) 1–15.
[42] L. Moga, A. Bucur, Nano insulation materials for application in nZEB, Procedia Manuf. 22 (2018) 309–316.
[43] R. Baetens, B.P. Jelle, J.V. Thue, M.J. Tenpierik, S. Grynning, S. Uvsløkk, A. Gustavsen, Vacuum insulation panels for building applications: A review and beyond, Energy Build. 42 (2010) 147–172.
[44] L. Aditya, T.M.I. Mahlia, B. Rismanchi, H.M. Ng, M.H. Hasan, H.S.C. Metselaar, O. Muraza, H.B. Aditiya, A review on insulation materials for energy conservation in buildings, Renew. Sustain. Energy Rev. 73 (2017) 1352–1365.
[45] R. Baetens, High performance thermal insulation materials for buildings, in: Nanotechnol. Eco-Efficient Constr., Elsevier, 2013: pp. 188–206.
[46] J. Jovanovic, X. Sun, S. Stevovic, J. Chen, Energy-efficiency gain by combination of PV modules and Trombe wall in the low-energy building design, Energy Build. 152 (2017) 568–576.
[47] O. Saadatian, K. Sopian, C.H. Lim, N. Asim, M.Y. Sulaiman, Trombe walls: A review of opportunities and challenges in research and development, Renew. Sustain. Energy Rev. 16 (2012) 6340–6351.
[48] H. Zhang, H. Shu, A Comprehensive Evaluation on Energy, Economic and Environmental Performance of the Trombe Wall during the Heating Season, J.

Therm. Sci. 28 (2019) 1141–1149. https://doi.org/10.1007/s11630-019-1176-7.
[49] M. Bojić, K. Johannes, F. Kuznik, Optimizing energy and environmental performance of passive Trombe wall, Energy Build. 70 (2014) 279–286.
[50] J. Eshraghi, N. Narjabadifam, N. Mirkhani, S.S. Khosroshahi, M. Ashjaee, A comprehensive feasibility study of applying solar energy to design a zero energy building for a typical home in Tehran, Energy Build. 72 (2014) 329–339.
[51] N. Garrison, C. Horowitz, C.A. Lunghino, J. Devine, D.S. Beckman, Looking up: how green roofs and cool roofs can reduce energy use, address climate change, and protect water resources in Southern California, Natural Resources Defence Council, 2012.
[52] F. Ascione, N. Bianco, F. de'Rossi, G. Turni, G.P. Vanoli, Green roofs in European climates. Are effective solutions for the energy savings in air-conditioning?, Appl. Energy. 104 (2013) 845–859.
[53] B. Barozzi, A. Bellazzi, M.C. Pollastro, The energy impact in buildings of vegetative solutions for extensive green roofs in temperate climates, Buildings. 6 (2016) 33.
[54] W. Miller, G. Crompton, J. Bell, Analysis of cool roof coatings for residential demand side management in tropical Australia, Energies. 8 (2015) 5303–5318.
[55] A. Niachou, K. Papakonstantinou, M. Santamouris, A. Tsangrassoulis, G. Mihalakakou, Analysis of the green roof thermal properties and investigation of its energy performance, Energy Build. 33 (2001) 719–729.
[56] K.W. Oleson, G.B. Bonan, J. Feddema, Effects of white roofs on urban temperature in a global climate model, Geophys. Res. Lett. 37 (2010).
[57] W. Wu, H.M. Skye, Net-zero nation: HVAC and PV systems for residential net-zero energy buildings across the United States, Energy Convers. Manag. 177 (2018) 605–628.
[58] E. Fabrizio, F. Seguro, M. Filippi, Integrated HVAC and DHW production systems for Zero Energy Buildings, Renew. Sustain. Energy Rev. 40 (2014) 515–541.
[59] H. Tang, X.-H. Liu, H. Li, Y. Zhou, Y. Jiang, Study on the reduction of condensation risks on the radiant cooling ceiling with superhydrophobic treatment, Build. Environ. 100 (2016) 135–144.
[60] X. Pang, M.A. Piette, N. Zhou, Characterizing variations in variable air volume system controls, Energy Build. 135 (2017) 166–175.
[61] Y. Narukawa, J. Narita, T. Sakamoto, K. Deguchi, T. Yamada, T. Mukai, Ultra-high efficiency white light emitting diodes, Jpn. J. Appl. Phys. 45 (2006) L1084.
[62] Y. Huang, J. Niu, A review of the advance of HVAC technologies as witnessed in ENB publications in the period from 1987 to 2014, Energy Build. 130 (2016) 33–45.
[63] I. Sarbu, A. Dorca, Review on heat transfer analysis in thermal energy storage using latent heat storage systems and phase change materials, Int. J. Energy Res. 43 (2019) 29–64.
[64] L. Navarro, A. De Gracia, S. Colclough, M. Browne, S.J. McCormack, P. Griffiths, L.F. Cabeza, Thermal energy storage in building integrated thermal systems: A review. Part 1. active storage systems, Renew. Energy. 88 (2016) 526–547.
[65] J.F. Belmonte, P. Egu\'\ia, A.E. Molina, J.A. Almendros-Ibáñez, R. Salgado, A simplified method for modeling the thermal performance of storage tanks

containing PCMs, Appl. Therm. Eng. 95 (2016) 394–410.
[66] S. Guillén-Lambea, B. Rodr\'\iguez-Soria, J.M. Mar\'\in, Control strategies for Energy Recovery Ventilators in the South of Europe for residential nZEB—Quantitative analysis of the air conditioning demand, Energy Build. 146 (2017) 271–282.
[67] H.B. Madessa, Performance analysis of roof-mounted photovoltaic systems--The case of a Norwegian residential building, Energy Procedia. 83 (2015) 474–483.
[68] M. Gul, Y. Kotak, T. Muneer, Review on recent trend of solar photovoltaic technology, Energy Explor. \& Exploit. 34 (2016) 485–526.
[69] E. Rachoutis, D. Koubogiannis, Energy Payback Time of a Rooftop Photovoltaic System in Greece, in: IOP Conf. Ser. Mater. Sci. Eng., 2016: p. 12092.
[70] C. Babu, P. Ponnambalam, The role of thermoelectric generators in the hybrid PV/T systems: A review, Energy Convers. Manag. 151 (2017) 368–385.
[71] D. Bobrova, Building-integrated wind turbines in the aspect of architectural shaping, Procedia Eng. 117 (2015) 404–410.
[72] K.-Y. Lee, S.-H. Tsao, C.-W. Tzeng, H.-J. Lin, Influence of the vertical wind and wind direction on the power output of a small vertical-axis wind turbine installed on the rooftop of a building, Appl. Energy. 209 (2018) 383–391.
[73] S. Eriksson, H. Bernhoff, M. Leijon, Evaluation of different turbine concepts for wind power, Renew. Sustain. Energy Rev. 12 (2008) 1419–1434.
[74] P.K. Datta, P.S. Leung, W. Roynarin, The performances of a vertical Darrieus machine with modern high lift airfoils, in: Proc. from LMAREST Conf. MAREC, 2002.
[75] M. Song, S. Deng, C. Dang, N. Mao, Z. Wang, Review on improvement for air source heat pump units during frosting and defrosting, Appl. Energy. 211 (2018) 1150–1170.
[76] P. Bayer, D. Saner, S. Bolay, L. Rybach, P. Blum, Greenhouse gas emission savings of ground source heat pump systems in Europe: A review, Renew. Sustain. Energy Rev. 16 (2012) 1256–1267.
[77] L. Belussi, B. Barozzi, A. Bellazzi, L. Danza, A. Devitofrancesco, C. Fanciulli, M. Ghellere, G. Guazzi, I. Meroni, F. Salamone, F. Scamoni, C. Scrosati, A review of performance of zero energy buildings and energy efficiency solutions, J. Build. Eng. 25 (2019) 100772. https://doi.org/https://doi.org/10.1016/j.jobe.2019.100772.
[78] A. Rentizelas, A. Tolis, I. Tatsiopoulos, Biomass district energy trigeneration systems: emissions reduction and financial impact, Water, Air, \& Soil Pollut. Focus. 9 (2009) 139–150.
[79] J. Lizana, C. Ortiz, V.M. Soltero, R. Chacartegui, District heating systems based on low-carbon energy technologies in Mediterranean areas, Energy. 120 (2017) 397–416.
[80] I. Bartolozzi, F. Rizzi, M. Frey, Are district heating systems and renewable energy sources always an environmental win-win solution? A life cycle assessment case study in Tuscany, Italy, Renew. Sustain. Energy Rev. 80 (2017) 408–420.
[81] D. Kolokotsa, D. Rovas, E. Kosmatopoulos, K. and Kalaitzakis, A roadmap towards intelligent net zero-and positive-energy buildings, Sol. Energy. 85 (2011) 3067–3084.
[82] N. Aste, M. Manfren, G. Marenzi, Building Automation and Control Systems and

performance optimization: A framework for analysis, Renew. Sustain. Energy Rev. 75 (2017) 313–330.
[83] D. Lee, C.-C. Cheng, Energy savings by energy management systems: A review, Renew. Sustain. Energy Rev. 56 (2016) 760–777.
[84] A. De Paola, M. Ortolani, G. Lo Re, G. Anastasi, S.K. Das, Intelligent management systems for energy efficiency in buildings: A survey, ACM Comput. Surv. 47 (2014) 1–38.
[85] H. Mirinejad, K.C. Welch, L. Spicer, A review of intelligent control techniques in HVAC systems, in: 2012 IEEE Energytech, 2012: pp. 1–5.
[86] K. McGlinn, B. Yuce, H. Wicaksono, S. Howell, Y. Rezgui, Usability evaluation of a web-based tool for supporting holistic building energy management, Autom. Constr. 84 (2017) 154–165.
[87] N. Damayanti, Internet of Things: a vision, architectural elements, and future directons, Internet Things a Vision, Archit. Elem. Futur. Directons. (n.d.).
[88] F. Salamone, L. Belussi, L. Danza, M. Ghellere, I. Meroni, An open source "smart lamp" for the optimization of plant systems and thermal comfort of offices, Sensors. 16 (2016) 338.
[89] European Commission, A Roadmap for moving to a competitive low carbon economy in 2050, Eur. Comm. (2011).
[90] European Parliament, Energy. Topics: Energy Efficiency. Buildings, (2018).
[91] European Parliament, Directive (EU) 2018/844 of the European Parliament and of the Council of 30 May 2018 amending Directive 2010/31/EU on the energy performance of buildings and Directive 2012/27/EU on energy efficiency, Off. J. Eur. Union. (2018) 75–91. https://doi.org/10.1007/3-540-47891-4_10.
[92] CEN European Commitee for Standardization, EN ISO 52016-1:2017 - Energy performance of buildings — Energy needs for heating and cooling, internal temperatures and sensible and latent head loads — Part 1: Calculation procedures Performance, (2017).
[93] M. Bagarić, I. [Banjad Pečur], B. Milovanović, Hygrothermal performance of ventilated prefabricated sandwich wall panel from recycled construction and demolition waste – A case study, Energy Build. 206 (2020) 109573. https://doi.org/https://doi.org/10.1016/j.enbuild.2019.109573.
[94] E. Di Giuseppe, G. Ulpiani, S. Summa, L. Tarabelli, C. Di Perna, M. D'Orazio, Hourly dynamic and monthly semi-stationary calculation methods applied to nZEBs: Impacts on energy and comfort, IOP Conf. Ser. Mater. Sci. Eng. 609 (2019) 1–8. https://doi.org/10.1088/1757-899X/609/7/072008.
[95] P.M. Congedo, C. Baglivo, G. Centonze, Walls comparative evaluation for the thermal performance improvement of low-rise residential buildings in warm Mediterranean climate, J. Build. Eng. 28 (2020) 101059. https://doi.org/https://doi.org/10.1016/j.jobe.2019.101059.
[96] I. Ballarini, A. Costantino, E. Fabrizio, V. Corrado, A Methodology to Investigate the Deviations between Simple and Detailed Dynamic Methods for the Building Energy Performance Assessment, Energies. 13 (2020). https://doi.org/10.3390/en13236217.
[97] T. Zakula, M. Bagaric, N. Ferdelji, B. Milovanovic, S. Mudrinic, K. Ritosa, L. Mazzarella, R. Scoccia, P. Colombo, M. Motta, Comparison of dynamic

simulations and the ISO 52016 standard for the assessment of building energy performance, Appl. Energy. 210 (2019) 113553. https://doi.org/https://doi.org/10.1016/j.apenergy.2019.113553.
[98] T. Zakula, N. Badun, N. Ferdelji, I. Ugrina, Framework for the ISO 52016 standard accuracy prediction based on the in-depth sensitivity analysis, Appl. Energy. 298 (2021) 117089. https://doi.org/10.1016/j.apenergy.2021.117089.
[99] L. Mazzarella, R. Scoccia, P. Colombo, M. Motta, Improvement to EN ISO 52016-1:2017 hourly heat transfer through a wall assessment: the Italian National Annex, Energy Build. 210 (2020) 109758. https://doi.org/https://doi.org/10.1016/j.enbuild.2020.109758.
[100] CEN European Commitee for Standardization, EN 15251 Indoor environmental input parameters for design and assessment of energy performance of buildings addressing indoor air quality, thermal environment, lighting and acoustics, CEN, Brussels, Belgium, 2007.
[101] T. Bergman, F. Incropera, D. DeWitt, A. Lavine, Fundamentals of heat and mass transfer, Seventh, 2011.
[102] J. Karlsson, A. Roos, Modelling the angular behaviour of the total solar energy transmittance of windows, Sol. Energy. 69 (2000) 321–329. https://doi.org/10.1016/S0038-092X(00)00083-9.
[103] M. Shin, J.S. Haberl, Thermal zoning for building HVAC design and energy simulation: A literature review, Energy Build. 203 (2019). https://doi.org/10.1016/j.enbuild.2019.109429.
[104] Ministro dello sviluppo economico., Italian Ministerial Decree of 5th July 1975: Modification to the ministerial instructions dated 20th June 1896 concerning the minimal height and the main hygienic-sanitary requirements in housing units, 1975 (1975) 18–20.
[105] UNI- Ente Nazionale Italiano di Unificazione, UNI 10840:2007 - Light and lighting - School rooms - General criteria for the artificial and natural lighting, (2007).
[106] Presidente della Repubblica, DECRETO DEL PRESIDENTE DELLA REPUBBLICA 26 agosto 1993, n. 412, Italy, 1993.
[107] UNI- Ente Nazionale Italiano di Unificazione, UNI/TS 11300-1:2014 - Energy performance of buildings - Part 1: Evaluation of energy need for space heating and cooling, Italy, 2014. http://store.uni.com/catalogo/norme/root-categorie-tc/uni/uni-ct-202/uni-ts-11300-1-2014?___store=en&___from_store=it.
[108] ASHRAE Guideline 14, Measurement of Energy, Demand, and Water Savings, 2014. www.ashrae.org.
[109] R.G. Pontius, O. Thontteh, H. Chen, Components of information for multiple resolution comparison between maps that share a real variable, Environ. Ecol. Stat. 15 (2008) 111–142. https://doi.org/10.1007/s10651-007-0043-y.
[110] C.J. Willmott, K. Matsuura, On the use of dimensioned measures of error to evaluate the performance of spatial interpolators, Int. J. Geogr. Inf. Sci. 20 (2006) 89–102. https://doi.org/10.1080/13658810500286976.
[111] M.D. Moldovan, I. Visa, M. Neagoe, B.G. Burduhos, Solar heating & cooling energy mixes to transform low energy buildings in nearly zero energy buildings, Energy Procedia. 48 (2014) 924–937. https://doi.org/10.1016/j.egypro.2014.02.106.
[112] Z.D. Arsan, Identification of the building parameters that influence heating and

cooling energy loads for apartment buildings in hot-humid climates, Energy. 36 (2011) 4287–4296.
[113] H. Li, S. Wang, H. Cheung, Sensitivity analysis of design parameters and optimal design for zero/low energy buildings in subtropical regions, Appl. Energy. 228 (2018) 1280–1291. https://doi.org/https://doi.org/10.1016/j.apenergy.2018.07.023.
[114] M. Zhao, H.M. Künzel, F. Antretter, Parameters influencing the energy performance of residential buildings in different Chinese climate zones, Energy Build. 96 (2015) 64–75. https://doi.org/https://doi.org/10.1016/j.enbuild.2015.03.007.
[115] H.E. Mechri, A. Capozzoli, V. Corrado, USE of the ANOVA approach for sensitive building energy design, Appl. Energy. 87 (2010) 3073–3083. https://doi.org/https://doi.org/10.1016/j.apenergy.2010.04.001.
[116] Rapidminer, https://rapidminer.com, (n.d.).
[117] M.A.A.E.D.A. Sayed, M.A. Fikry, Impact of glass facades on internal environment of buildings in hot arid zone, Alexandria Eng. J. 58 (2019) 1063–1075. https://doi.org/10.1016/j.aej.2019.09.009.
[118] A.A.-W. Hawila, A. Merabtine, N. Troussier, R. Bennacer, Combined use of dynamic building simulation and metamodeling to optimize glass facades for thermal comfort, Build. Environ. 157 (2019) 47–63. https://doi.org/https://doi.org/10.1016/j.buildenv.2019.04.027.
[119] G. [Kiran Kumar, S. Saboor, T.P. [Ashok Babu], Investigation of various wall and window glass material buildings in different climatic zones of India for energy efficient building construction, Mater. Today Proc. 5 (2018) 23224–23234. https://doi.org/https://doi.org/10.1016/j.matpr.2018.11.054.
[120] G. KiranKumar, S. Saboor, T.P. [Ashok Babu], Investigation of Various Low Emissivity Glass Materials for Green Energy Building Construction in Indian Climatic Zones, Mater. Today Proc. 4 (2017) 8052–8058. https://doi.org/https://doi.org/10.1016/j.matpr.2017.07.144.
[121] J. Potočnik, M. Košir, Influence of commercial glazing and wall colours on the resulting non-visual daylight conditions of an office, Build. Environ. 171 (2020) 106627. https://doi.org/https://doi.org/10.1016/j.buildenv.2019.106627.
[122] K. Mehaoued, B. Lartigue, Influence of a reflective glass façade on surrounding microclimate and building cooling load: Case of an office building in Algiers, Sustain. Cities Soc. 46 (2019) 101443. https://doi.org/https://doi.org/10.1016/j.scs.2019.101443.
[123] H. Demirhan, Z. Renwick, Missing value imputation for short to mid-term horizontal solar irradiance data, Appl. Energy. 225 (2018) 998–1012. https://doi.org/https://doi.org/10.1016/j.apenergy.2018.05.054.
[124] UNI - Ente Italiano di Normazione, UNI 10349-1:2016 Riscaldamento e raffrescamento degli edifici - Dati climatici - Parte 1: Medie mensili per la valutazione della prestazione termo-energetica dell'edificio e metodi per ripartire l'irradianza solare nella frazione diretta e diffusa e per c, 2016.
[125] J.W. Spencer, Fourier Series Representation of the Position of the Sun, 2 (1971) 172. http://www.mail-archive.com/sundial@uni-koeln.de/msg01050.html.
[126] J. Boland, B. Ridley, B. Brown, Models of diffuse solar radiation, Renew. Energy. 33 (2008) 575–584. https://doi.org/10.1016/j.renene.2007.04.012.

[127] F. Kasten, A.T. Young, Revised optical air mass tables and approximation formula, Appl. Opt. 28 (1989) 4735–4738. https://doi.org/10.1364/AO.28.004735.
[128] F. Kasten, A Simple Parameterization of the Pyrheliometric Formula for Determining the Linke Turbidity Factor, Meteorol. Rundschau. 33 (1980) 124–127.
[129] F. Kasten, The linke turbidity factor based on improved values of the integral Rayleigh optical thickness, Sol. Energy. 56 (1996) 239–244. https://doi.org/https://doi.org/10.1016/0038-092X(95)00114-7.
[130] B.D. Hunn, D.O. Calafell, Determination of average ground reflectivity for solar collectors, Sol. Energy. 19 (1977) 87–89. https://doi.org/https://doi.org/10.1016/0038-092X(77)90092-5.
[131] B.Y.H. Liu, R.C. Jordan, The interrelationship and characteristic distribution of direct, diffuse and total solar radiation, Sol. Energy. 4 (1960) 1–19. https://doi.org/10.1016/0038-092X(60)90062-1.
[132] R.S. and A.Z. Perez, R., P. Ineichen, E. Maxwell, Dynamic Models for hourly global-to-direct irradiance conversion., Solar World Congress 1991., 1991.
[133] D.T. Reindl, W.A. Beckman, J.A. Duffie, Evaluation of hourly tilted surface radiation models, Sol. Energy. 45 (1990) 9–17. https://doi.org/10.1016/0038-092X(90)90061-G.
[134] D.G. Erbs, S.A. Klein, J.A. Duffie, Estimation of the diffuse radiation fraction for hourly, daily and monthly-average global radiation, Sol. Energy. 28 (1982) 293–302. https://doi.org/10.1016/0038-092X(82)90302-4.
[135] R. Perez, P. Ineichen, R. Seals, J. Michalsky, R. Stewart, Modeling daylight availability and irradiance components from direct and global irradiance, Sol. Energy. 44 (1990) 271–289. https://doi.org/https://doi.org/10.1016/0038-092X(90)90055-H.
[136] D.T. Reindl, W.A. Beckman, J.A. Duffie, Diffuse fraction correlations, Sol. Energy. 45 (1990) 1–7. https://doi.org/10.1016/0038-092X(90)90060-P.
[137] M. Ibañez-Puy, M. Vidaurre-Arbizu, J.A. Sacristán-Fernández, C. Martín-Gómez, Opaque Ventilated Façades: Thermal and energy performance review, Renew. Sustain. Energy Rev. 79 (2017) 180–191. https://doi.org/10.1016/j.rser.2017.05.059.
[138] D. Bikas, K. Tsikaloudaki, K.J. Kontoleon, C. Giarma, S. Tsoka, D. Tsirigoti, Ventilated Facades: Requirements and Specifications Across Europe, Procedia Environ. Sci. 38 (2017) 148–154. https://doi.org/10.1016/j.proenv.2017.03.096.
[139] F. Stazi, G. Ulpiani, M. Pergolini, C. Di Perna, M. D'Orazio, The role of wall layers properties on the thermal performance of ventilated facades: Experimental investigation on narrow-cavity design, Energy Build. 209 (2020) 109622. https://doi.org/10.1016/j.enbuild.2019.109622.
[140] L.E. Aelenei, A.M. Rodrigues, U.T. de Lisboa, Thermal performance of naturally ventilated cavity walls, 2005.
[141] M. Ciampi, F. Leccese, G. Tuoni, Ventilated facades energy performance in summer cooling of buildings, Sol. Energy. 75 (2003) 491–502. https://doi.org/https://doi.org/10.1016/j.solener.2003.09.010.
[142] C. Marinosci, G. Semprini, G.L. Morini, Experimental analysis of the summer thermal performances of a naturally ventilated rainscreen façade building, Energy Build. 72 (2014) 280–287.

https://doi.org/https://doi.org/10.1016/j.enbuild.2013.12.044.
[143] J. Straube, G. Finch, Ventilated Wall Claddings: Review, Field Performance, and Hygrothermal Modeling, in: 2007.
[144] J. Falk, K. Sandin, Ventilated rainscreen cladding: A study of the ventilation drying process, Build. Environ. 60 (2013) 173–184. https://doi.org/https://doi.org/10.1016/j.buildenv.2012.11.015.
[145] M. Vanpachtenbeke, J. Langmans, J. Van den Bulcke, J. Van Acker, S. Roels, On the drying potential of cavity ventilation behind brick veneer cladding: A detailed field study, Build. Environ. 123 (2017) 133–145. https://doi.org/https://doi.org/10.1016/j.buildenv.2017.06.047.
[146] M.R. Bassett, S. McNeil, Drained and Vented Cavity Walls: Measured Ventilation Rates, in: IRHACE Conf., BRANZ, 2005.
[147] J. Falk, K. Sandin, Ventilated rainscreen cladding: Measurements of cavity air velocities, estimation of air change rates and evaluation of driving forces, Build. Environ. 59 (2013) 164–176. https://doi.org/10.1016/j.buildenv.2012.08.017.
[148] R. Van Straaten, J. Straube, T. Trainor, A. Habellion, Wind washing effects on mineral wool insulated sheathings, Proc. Build. XIII. (2016).
[149] E. Lorente, S ; Mattias, Protection against Solar over Heatings Using High Aspect Ratio Open Vertical Cavities, in: World Renew. Energy Congr., Florence, 1998: pp. 20–25.
[150] V.M.S. Francés, E.J.S. Escriva, J.M.P. Ojer, E. Bannier, V.C. Soler, G.S. Moreno, Modeling of ventilated façades for energy building simulation software, Energy Build. 65 (2013) 419–428.
[151] A. Gagliano, F. Nocera, S. Aneli, Thermodynamic analysis of ventilated façades under different wind conditions in summer period, Energy Build. 122 (2016) 131–139. https://doi.org/https://doi.org/10.1016/j.enbuild.2016.04.035.
[152] A. Gagliano, S. Aneli, Analysis of the energy performance of an Opaque Ventilated Façade under winter and summer weather conditions, Sol. Energy. 205 (2020) 531–544. https://doi.org/https://doi.org/10.1016/j.solener.2020.05.078.
[153] F. Patania, A. Gagliano, F. Nocera, A. Ferlito, A. Galesi, Thermofluid-dynamic analysis of ventilated facades, Energy Build. 42 (2010) 1148–1155. https://doi.org/https://doi.org/10.1016/j.enbuild.2010.02.006.
[154] J.P. Piñon, E.F.P. Burnett, D. Davidovic, J. Srebric, The airflow characteristics of ventilated cavities in screen-Type enclosure wall systems (RP-1091), Therm. Perform. Exter. Envel. Whole Build. (2004).
[155] M. Rahiminejad, D. Khovalyg, Review on ventilation rates in the ventilated air-spaces behind common wall assemblies with external cladding, Build. Environ. 190 (2021) 107538. https://doi.org/10.1016/j.buildenv.2020.107538.
[156] M.C. Peel, B.L. Finlayson, T.A. McMahon, Updated world map of the Köppen-Geiger climate classification, Hydrol. Earth Syst. Sci. Discuss. 4 (2007) 439–473.
[157] G. Ulpiani, D. Giuliani, A. Romagnoli, C. di Perna, Experimental monitoring of a sunspace applied to a NZEB mock-up: Assessing and comparing the energy benefits of different configurations, Energy Build. 152 (2017). https://doi.org/10.1016/j.enbuild.2017.04.034.
[158] Deutsches Institut für Normung, DIN EN 845-1 Specification for ancillary components for masonry - Part 1: Wall ties, tension straps, hangers and brackets,

2016.
[159] International Organization for Standardization, ISO 6946:2008 Building components and building elements - Thermal resistance and thermal transmittance - Calculation method, 2008.
[160] International Organization for Standardization, ISO 13786:2008 Thermal performance of building components - Dynamic thermal characteristics - Calculation methods, 2008.
[161] M. of I. E. Development, Interministerial Decree of 26 June 2015 - Application of calculation methods for energy performance and definition of minimum building requirements., Gazz. Uff. (2015).
[162] L. Breiman, J. Friedman, R. Olshen, C.J. Stone, Classification and regression trees, Brooks/Cole Publishing, Monterey, 1983.
[163] H. Drucker, C.J. Burges, L. Kaufman, A. Smola, V. Vapnik, Support vector regression machines, Adv. Neural Inf. Process. Syst. 9 (1997) 155–161.
[164] S. R. Safavian, D. Landgrebe, A survey of decision tree classi er methodology, IEEE Trans. Syst. Man. Cybern. 21 (1991) 660–674.
[165] C. Cortes, V. Vapnik, Support-vector networks, Mach. Learn. 20 (1995) 273–297.
[166] S. Hochreiter, J. Schmidhuber, Long short-term memory, Neural Comput. 9 (1997) 1735–1780.
[167] Keras, https://keras.io, (n.d.).
[168] Cened, Concetti di base: fisica delle pareti, in: Man. CENED+ - Vers. 1.2, 2011.
[169] A.G. Hestnes, Building integration of solar energy systems, Sol. Energy. 67 (2000) 181–187.
[170] C. Zappone, La serra solare – criteri di progettazione e risparmio energetico,architettura, funzionamento, materiali, aspetti normativi., S.l. Archit. Esselibri S.p.A. (2009).
[171] M. Baker, R. Lorenzen, Oregon monitored solar building study., Eugene OR Sol. Energy Center, Univ. Oregon. (1979).
[172] J.M. Mottard, A. Fissore, Thermal simulation of an attached sunspace and its experimental validation, Sol. Energy. 81 (2007) 305–315. https://doi.org/10.1016/j.solener.2006.07.005.
[173] J.J. Roux, C. Teodosiu, D. Covalet, R. Chareille, Validation of a glazed space simulation model using full-scale experimental data, Energy Build. 36 (2004) 557–565. https://doi.org/10.1016/j.enbuild.2004.01.030.
[174] K.M. Bataineh, N. Fayez, Analysis of thermal performance of building attached sunspace, Energy Build. 43 (2011) 1863–1868. https://doi.org/10.1016/j.enbuild.2011.03.030.
[175] G. Oliveti, M. De Simone, S. Ruffolo, Evaluation of the absorption coefficient for solar radiation in sunspaces and windowed rooms, Sol. Energy. 82 (2008) 212–219. https://doi.org/10.1016/j.solener.2007.07.009.
[176] G. Mihalakakou, On the use of sunspace for space heating/cooling in Europe, Renew. Energy. 26 (2002) 415–429. https://doi.org/10.1016/S0960-1481(01)00138-0.
[177] G. Oliveti, N. Arcuri, M. De Simone, R. Bruno, Solar heat gains and operative temperature in attached sunspaces, Renew. Energy. 39 (2012) 241–249. https://doi.org/10.1016/j.renene.2011.08.010.

[178] G. Chiesa, M. Simonetti, G. Ballada, Potential of attached sunspaces in winter season comparing different technological choices in Central and Southern Europe, Energy Build. 138 (2017) 377–395. https://doi.org/10.1016/j.enbuild.2016.12.067.
[179] D. Aelenei, H. De Azevedo Leal, L. Aelenei, The use of attached-sunspaces in retrofitting design: The case of residential buildings in Portugal, Energy Procedia. 48 (2014) 1436–1441. https://doi.org/10.1016/j.egypro.2014.02.162.
[180] G. Mihalakakou, A. Ferrante, Energy conservation and potential of a sunspace: Sensitivity analysis, Energy Convers. Manag. 41 (2000) 1247–1264. https://doi.org/10.1016/S0196-8904(99)00178-8.
[181] D. Kolokotsa, M. Santamouris, A. Synnefa, T. Karlessi, Passive Solar Architecture, in: Compr. Renew. Energy, Elsevier, 2012: pp. 637–665. https://doi.org/10.1016/B978-0-08-087872-0.00320-6.
[182] M. Qingsong, H. Fukuda, M. Lee, T. Kobatake, Y. Kuma, Experimental Analysis of the Thermal Performance of a Sunspace Attached to a House with a Central Air Conditioning System, (2018). https://doi.org/10.3390/su10051428.
[183] D. Ignjatović, M. Jovanović Popović, J. Kavran, Application of sunspaces in fostering energy efficiency and economical viability of residential buildings in Serbia, Energy Build. 98 (2015) 3–9. https://doi.org/10.1016/j.enbuild.2015.02.049.
[184] G. Ulpiani, D. Giuliani, A. Romagnoli, C. di Perna, Experimental monitoring of a sunspace applied to a NZEB mock-up: Assessing and comparing the energy benefits of different configurations, Energy Build. 152 (2017) 194–215. https://doi.org/10.1016/j.enbuild.2017.04.034.
[185] S. Pizzo, Architetture nZEB: Come Si Vive in una Casa a Zero Consumi?, HouzzItalia. (2016).
[186] F. Stazi, E. Tomassoni, C. Bonfigli, C. Di Perna, Energy, comfort and environmental assessment of different building envelope techniques in a Mediterranean climate with a hot dry summer, Appl. Energy. 134 (2014) 176–196. https://doi.org/10.1016/j.apenergy.2014.08.023.
[187] G. Chiesa, M. Grosso, The influence of different hourly typical meteorological years on dynamic simulation of buildings, in: Energy Procedia, 2015: pp. 2560–2565.
[188] W. Köppen, R. Geiger, Das Geographische System der Klimate, Handb. Der Klimatologie. (1936).
[189] ISO, ISO 7726:1998 Ergonomics of the thermal environment -- Instruments for measuring physical quantities, (1998).
[190] DPR, n. 74 Decreto del Presidente della Repubblica, Regolamento recante definizione dei criteri generali in materia di esercizio, conduzione, controllo, manutenzione e ispezione degli impianti termici per la climatizzazione invernale ed estiva degli edifici e, (2013).
[191] M.J. Malik, R. van der Velde, Z. Vekerdy, Z. Su, M.F. Salman, Semi-empirical approach for estimating broadband albedo of snow, Remote Sens. Environ. 115 (2011) 2086–2095. https://doi.org/10.1016/j.rse.2011.04.010.
[192] E.L. Pope, I.C. Willis, A. Pope, E.S. Miles, N.S. Arnold, W.G. Rees, Contrasting snow and ice albedos derived from MODIS, Landsat ETM+ and airborne data from Langjökull, Iceland, Remote Sens. Environ. 175 (2016) 183–195. https://doi.org/10.1016/j.rse.2015.12.051.

[193] B.J. Choudhury, A.T.C. Chang, NASA Technical Memorandum 80649 THE ALBEDO OF SNOW, (1980).
[194] X. Li, S. Kang, G. Zhang, B. Qu, L. Tripathee, R. Paudyal, Z. Jing, Y. Zhang, F. Yan, G. Li, X. Cui, R. Xu, Z. Hu, C. Li, Light-absorbing impurities in a southern Tibetan Plateau glacier: Variations and potential impact on snow albedo and radiative forcing, Atmos. Res. 200 (2018) 77–87. https://doi.org/10.1016/j.atmosres.2017.10.002.
[195] W.L. Lee, K.N. Liou, Effect of absorbing aerosols on snow albedo reduction in the Sierra Nevada, Atmos. Environ. 55 (2012) 425–430. https://doi.org/10.1016/j.atmosenv.2012.03.024.
[196] F. Cereceda-Balic, V. Vidal, H. Moosmüller, M. Lapuerta, Reduction of snow albedo from vehicle emissions at Portillo, Chile, Cold Reg. Sci. Technol. 146 (2018) 43–52. https://doi.org/10.1016/j.coldregions.2017.11.008.
[197] A.S. Gardner, M.J. Sharp, A review of snow and ice albedo and the development of a new physically based broadband albedo parameterization, J. Geophys. Res. Earth Surf. 115 (2010) 1–15. https://doi.org/10.1029/2009JF001444.
[198] G. Ulpiani, M. Borgognoni, A. Romagnoli, C. Di Perna, Comparing the performance of on/off, PID and fuzzy controllers applied to the heating system of an energy-efficient building, Energy Build. 116 (2016) 1–17. https://doi.org/10.1016/j.enbuild.2015.12.027.
[199] G. Ulpiani, Overheating phenomena induced by fully-glazed facades: Investigation of a sick building in Italy and assessment of the benefits achieved via fuzzy control of the AC system, Sol. Energy. 158 (2017). https://doi.org/10.1016/j.solener.2017.10.024.
[200] F. Stazi, F. Naspi, G. Ulpiani, C. Di Perna, Indoor air quality and thermal comfort optimization in classrooms developing an automatic system for windows opening and closing, Energy Build. 139 (2017). https://doi.org/10.1016/j.enbuild.2017.01.017.
[201] G. Ulpiani, M. Benedettelli, C. di Perna, B. Naticchia, Overheating phenomena induced by fully-glazed facades: Investigation of a sick building in Italy and assessment of the benefits achieved via model predictive control of the AC system, Sol. Energy. 157 (2017). https://doi.org/10.1016/j.solener.2017.09.009.
[202] V. Ciancio, F. Salata, S. Falasca, G. Curci, I. Golasi, P. de Wilde, Energy demands of buildings in the framework of climate change: An investigation across Europe, Sustain. Cities Soc. 60 (2020) 102213. https://doi.org/https://doi.org/10.1016/j.scs.2020.102213.
[203] M. Olonscheck, A. Holsten, J.P. Kropp, Heating and cooling energy demand and related emissions of the German residential building stock under climate change, Energy Policy. 39 (2011) 4795–4806. https://doi.org/https://doi.org/10.1016/j.enpol.2011.06.041.
[204] K. Verichev, M. Zamorano, M. Carpio, Effects of climate change on variations in climatic zones and heating energy consumption of residential buildings in the southern Chile, Energy Build. 215 (2020) 109874. https://doi.org/https://doi.org/10.1016/j.enbuild.2020.109874.
[205] M.E. Angeles, J.E. González, N. Ramírez, Impacts of climate change on building energy demands in the intra-Americas region, Theor. Appl. Climatol. 133 (2018)

59–72. https://doi.org/10.1007/s00704-017-2175-9.
[206] T. Frank, Climate change impacts on building heating and cooling energy demand in Switzerland, Energy Build. 37 (2005) 1175–1185. https://doi.org/https://doi.org/10.1016/j.enbuild.2005.06.019.
[207] C. Tribuiani, L. Tarabelli, S. Summa, C. Di Perna, Thermal performance of a massive wall in the Mediterranean climate: Experimental and analytical research, Appl. Sci. 10 (2020). https://doi.org/10.3390/app10134611.
[208] L.F. Cabeza, M. Chàfer, Technological options and strategies towards zero energy buildings contributing to climate change mitigation: A systematic review, Energy Build. 219 (2020) 110009. https://doi.org/https://doi.org/10.1016/j.enbuild.2020.110009.
[209] L. Troup, M.J. Eckelman, D. Fannon, Simulating future energy consumption in office buildings using an ensemble of morphed climate data, Appl. Energy. 255 (2019) 113821. https://doi.org/10.1016/j.apenergy.2019.113821.
[210] L. Wang, X. Liu, H. Brown, Prediction of the impacts of climate change on energy consumption for a medium-size office building with two climate models, Energy Build. 157 (2017) 218–226. https://doi.org/https://doi.org/10.1016/j.enbuild.2017.01.007.
[211] P.A. Favarolo, H. Manz, Temperature-driven single-sided ventilation through a large rectangular opening, Build. Environ. 40 (2005) 689–699. https://doi.org/https://doi.org/10.1016/j.buildenv.2004.08.003.
[212] M.J. Duffy, M. Hiller, D.E. Bradley, J.W. Werner Keilholz, TRNSYS – FEATURES AND FUNCTIONALITITY FOR BUILDING SIMULATION 2009, (2009).
[213] I.N.C. TRIMBLE, SketchUp, (2020).
[214] P. Ellis, OpenStudio plugin for Google SketchUp3D, (2009). http://sourceforge.net/projects/openstudio.
[215] C.T. Italiano, C.T.I. Energia, Prestazioni energetiche degli edifici Parte 1: Determinazione del fabbisogno di energia termica dell'edificio per la climatizzazione estiva ed invernale, Italy, 2008.
[216] D. D'Agostino, P. Zangheri, B. Cuniberti, D. Paci, P. Bertoldi, D. D'Agostino, P. Zangheri, B. Cuniberti, D. Paci, P. Bertoldi, Synthesis Report on the National Plans for Nearly Zero Energy Buildings (NZEBs), 2016. https://doi.org/10.2790/659611.
[217] L. Ortiz, J.E. González, W. Lin, Climate change impacts on peak building cooling energy demand in a coastal megacity, Environ. Res. Lett. 13 (2018). https://doi.org/10.1088/1748-9326/aad8d0.

Appendix A.

A.1. Thermo-physical properties of all stratigraphies used for case study simulations

N.	Distribution of Mass	U	Ms	YIE	fa	φ	κj
-	-	W/(m^{2}K)	kg/m²	W/(m^{2}K)	-	h	kJ/(m²K)
1	D	0.228	315.00	0.004	0.019	23.10	44.12
2	D	0.315	246.00	0.019	0.060	18.75	37.60
3	D	0.343	294.00	0.018	0.052	18.18	44.02
4	D	0.230	432.00	0.001	0.005	5.93	39.57
5	D	0.355	228.00	0.026	0.074	16.83	39.10
6	D	0.368	353.20	0.013	0.036	20.83	41.74
7	D	0.356	274.85	0.018	0.050	18.55	40.55
8	D	0.237	228.86	0.007	0.031	21.10	35.77
9	D	0.218	227.80	0.007	0.031	21.92	34.56
10	D	0.163	292.99	0.001	0.006	29.22	34.36
11	D	0.238	265.09	0.006	0.026	22.70	36.17
12	D	0.243	444.15	0.002	0.010	26.95	38.85
13	D	0.208	444.15	0.001	0.004	29.08	38.86
14	D	0.343	375.06	0.011	0.033	20.35	41.30
15	D	0.209	360.00	0.001	0.005	28.72	41.93
16	D	0.215	287.00	0.003	0.015	25.35	39.77
17	D	0.169	369.00	0.001	0.003	32.77	39.80
18	D	0.192	328.00	0.001	0.007	28.88	39.87
19	D	0.239	308.25	0.004	0.017	24.57	37.29
20	D	0.310	404.10	0.005	0.016	24.70	41.48
21	D	0.230	432.00	0.001	0.005	5.93	39.57
22	D	0.215	52.13	0.120	0.554	6.67	21.63
23	D	0.244	49.63	0.154	0.631	5.87	22.12
24	D	0.364	44.18	0.288	0.793	4.31	22.79
25	D	0.281	47.93	0.191	0.679	5.50	22.24

26	D	0.383	43.55	0.310	0.810	4.13	22.66
27	D	0.292	47.30	0.204	0.699	5.30	22.38
28	D	0.271	48.55	0.179	0.660	5.70	22.22
29	D	0.371	199.50	0.048	0.130	13.80	44.38
30	D	0.296	265.60	0.013	0.044	20.20	37.73
31	D	0.285	345.60	0.006	0.020	23.76	39.50
32	D	0.262	187.60	0.020	0.075	17.86	34.47
33	D	0.380	246.75	0.040	0.105	15.40	38.84
34	D	0.275	270.00	0.007	0.027	21.40	41.82
35	D	0.352	180.00	0.036	0.102	15.08	41.94
36	D	0.363	164.00	0.059	0.163	14.21	39.97
37	D	0.252	246.00	0.009	0.035	21.50	39.74
38	D	0.402	196.00	0.059	0.146	13.08	44.58
39	D	0.518	246.75	0.090	0.173	12.90	42.23
40	D	0.482	41.05	0.422	0.875	3.20	22.12
41	IE	0.323	286.44	0.135	0.418	6.73	50.13
42	IE	0.233	278.64	0.056	0.241	10.70	42.74
43	IE	0.369	271.14	0.115	0.310	8.68	43.64
44	IE	0.226	20.55	0.192	0.888	3.81	34.26
45	IE	0.248	19.95	0.223	0.901	3.46	33.99
46	IE	0.350	18.75	0.321	0.918	2.88	33.20
47	IE	0.339	272.38	0.048	0.141	14.28	42.76
48	IE	0.266	276.13	0.033	0.125	15.30	42.52
49	IE	0.376	285.19	0.067	0.178	12.41	49.46
50	IE	0.295	285.94	0.050	0.169	12.80	49.37
51	IE	0.260	25.10	0.227	0.871	3.96	36.96
52	IE	0.303	19.20	0.276	0.913	3.08	33.53
53	IE	0.322	24.35	0.284	0.883	3.58	36.54
54	IE	0.368	18.60	0.339	0.920	2.83	33.08
55	IE	0.598	17.55	0.570	0.953	2.03	26.22
56	IE	0.561	14.98	0.528	0.941	2.22	30.39
57	I	0.259	249.13	0.008	0.031	20.56	37.70
58	I	0.269	248.50	0.009	0.034	20.36	37.69
59	I	0.253	229.50	0.010	0.041	17.90	39.16
60	I	0.298	228.90	0.015	0.051	17.50	39.13

61	I	0.326	228.60	0.020	0.061	17.20	39.11
62	I	0.278	354.10	0.004	0.015	22.81	41.87
63	I	0.317	353.65	0.006	0.020	22.33	41.83
64	I	0.255	381.31	0.004	0.016	21.68	41.89
65	I	0.264	380.69	0.005	0.018	21.53	41.39
66	I	0.284	379.44	0.006	0.021	21.25	41.37
67	I	0.287	238.60	0.035	0.121	12.30	45.99
68	I	0.328	238.15	0.042	0.128	12.10	46.10
69	I	0.383	237.70	0.053	0.138	11.90	46.25
70	I	0.262	404.70	0.002	0.007	2.36	41.51
71	I	0.208	253.50	0.004	0.020	21.68	37.76
72	I	0.207	230.40	0.007	0.033	18.35	39.18
73	I	0.197	355.60	0.002	0.009	23.60	41.90
74	I	0.211	385.06	0.003	0.014	22.55	41.41
75	I	0.227	405.30	0.001	0.005	26.85	41.52
76	I	0.214	239.80	0.023	0.109	12.88	45.83
77	I	0.345	238.00	0.045	0.131	12.03	46.14
78	I	0.580	236.80	0.109	0.187	11.32	47.08
79	I	0.462	237.25	0.071	0.154	11.67	46.52
80	I	0.505	196.25	0.121	0.239	9.67	47.52
81	E	0.208	253.50	0.005	0.022	21.45	23.47
82	E	0.207	230.40	0.008	0.039	18.03	21.56
83	E	0.197	355.60	0.002	0.011	23.26	21.57
84	E	0.211	385.06	0.003	0.016	22.26	23.58
85	E	0.214	239.80	0.030	0.139	12.51	21.94
86	E	0.345	238.00	0.056	0.163	11.65	22.01
87	E	0.227	405.30	0.001	0.006	2.53	22.33
88	E	0.259	249.13	0.009	0.033	20.33	25.14
89	E	0.269	248.50	0.010	0.036	20.13	26.10
90	E	0.274	229.20	0.014	0.052	17.40	22.27
91	E	0.298	228.90	0.017	0.058	17.18	23.17
92	E	0.278	354.10	0.005	0.017	22.46	23.19
93	E	0.317	353.65	0.007	0.022	22.00	26.93
94	E	0.255	381.31	0.005	0.020	21.36	23.31
95	E	0.264	380.69	0.006	0.022	21.21	23.40

96	E	0.284	379.44	0.007	0.024	20.93	23.87
97	E	0.321	377.56	0.010	0.031	20.41	26.16
98	E	0.328	238.15	0.052	0.159	11.71	21.91
99	E	0.383	237.70	0.065	0.170	11.50	22.33
100	E	0.262	404.70	0.002	0.008	2.05	25.21
101	E	0.538	199.28	0.135	0.251	10.77	29.74
102	E	0.442	201.15	0.090	0.205	11.35	25.41
103	E	0.417	201.78	0.081	0.195	11.50	24.77

A.2. Weight analysis of the thermo-physical attributes of opaque structures

Legend:

Range	Upper limit
0.000 - 0.150	0.150
0.151 - 0.300	0.300
0.301 - 0.450	0.450
0.451 - 0.600	0.600
0.601 - 0.750	0.750
0.751 - 0.900	0.900
0.901 - 1.000	1.000

Table A2.4 Weight analysis of the thermo-physical attributes of opaque structures, for the winter period and with ggl=0.77.

	M,h_EU	M,h_IT	M,h_TRN	R,h_EU	R,h_IT	R,h_TRN	P,h_EU	P,h_IT	P,h_TRN
U [W/(m^{2}K)]	0.999	0.996	0.997	0.998	0.992	0.994	0.979	0.985	0.974
Yie [W/(m²K)]	0.564	0.567	0.576	0.565	0.526	0.580	0.585	0.604	0.592
phi [h]	0.468	0.454	0.479	0.470	0.444	0.484	0.477	0.479	0.500
Ctot [kJ/m²K]	0.439	0.448	0.453	0.437	0.430	0.452	0.457	0.479	0.451
Ms [kg/m²]	0.388	0.396	0.405	0.385	0.374	0.405	0.403	0.426	0.408
fa [-]	0.378	0.376	0.392	0.376	0.347	0.396	0.395	0.409	0.414
ki [kJ/(m²K)]	0.053	0.030	0.077	0.028	0.038	0.082	0.099	0.041	0.102

Table A2.5 Weight analysis of the thermo-physical attributes of opaque structures, for the summer period and with ggl=0.77.

	M,c_EU	M,c_IT	M,c_TRN	R,c_EU	R,c_IT	R,c_TRN	P,c_EU	P,c_IT	P,c_TRN
U [W/(m^{2}K)]	0.852	0.954	0.762	0.876	0.833	0.825	0.775	0.759	0.727
Yie [W/(m²K)]	0.291	0.322	0.345	0.253	0.127	0.352	0.123	0.116	0.303
phi [h]	0.290	0.325	0.385	0.310	0.243	0.394	0.244	0.273	0.365
Ctot [kJ/m²K]	0.208	0.259	0.211	0.190	0.138	0.220	0.113	0.121	0.170

Ms [kg/m²]	0.163	0.200	0.184	0.129	0.072	0.186	0.043	0.055	0.143
fa [-]	0.135	0.151	0.221	0.088	0.001	0.214	0.025	0.028	0.186
ki [kJ/(m²K)]	0.439	0.203	0.302	0.273	0.206	0.288	0.061	0.022	0.320

Table A2.6 Weight analysis of the thermo-physical attributes of opaque structures, for the winter period and with ggl=0.34.

	M,h_EU	**M,h_IT**	**M,h_TRN**	**R,h_EU**	**R,h_IT**	**R,h_TRN**	**P,h_EU**	**P,h_IT**	**P,h_TRN**
U [W/(m²K)]	0.998	0.996	0.996	0.999	0.995	0.993	0.988	0.993	0.970
Yie [W/(m²K)]	0.552	0.556	0.566	0.551	0.553	0.568	0.556	0.572	0.566
phi [h]	0.463	0.447	0.473	0.459	0.445	0.477	0.467	0.454	0.488
Ctot [kJ/m²K]	0.428	0.438	0.442	0.424	0.433	0.439	0.423	0.452	0.425
Ms [kg/m²]	0.378	0.386	0.393	0.372	0.380	0.392	0.368	0.398	0.382
fa [-]	0.365	0.365	0.381	0.361	0.358	0.383	0.358	0.378	0.389
ki [kJ/(m²K)]	0.092	0.042	0.085	0.061	0.025	0.095	0.033	0.037	0.129

Table A2.7 Weight analysis of the thermo-physical attributes of opaque structures, for the summer period and with ggl=0.34.

	M,c_EU	**M,c_IT**	**M,c_TRN**	**R,c_EU**	**R,c_IT**	**R,c_TRN**	**P,c_EU**	**P,c_IT**	**P,c_TRN**
U [W/(m²K)]	0.537	0.798	0.670	0.461	0.394	0.619	0.064	0.014	0.510
Yie [W/(m²K)]	0.036	0.001	0.254	0.724	0.843	0.227	0.375	0.588	0.188
phi [h]	0.050	0.131	0.324	0.446	0.440	0.318	0.153	0.300	0.294
Ctot [kJ/m²K]	0.024	0.002	0.112	0.556	0.612	0.106	0.342	0.406	0.068
Ms [kg/m²]	0.050	0.063	0.082	0.565	0.630	0.083	0.394	0.455	0.054
fa [-]	0.063	0.136	0.145	0.642	0.753	0.135	0.461	0.579	0.119
ki [kJ/(m²K)]	0.481	0.312	0.341	0.531	0.055	0.334	0.149	0.376	0.357

Appendix B.

B.1. Comparison between the models for separation of direct (I,b) and diffuse (I,d) solar irradiance on the horizontal and vertical plane

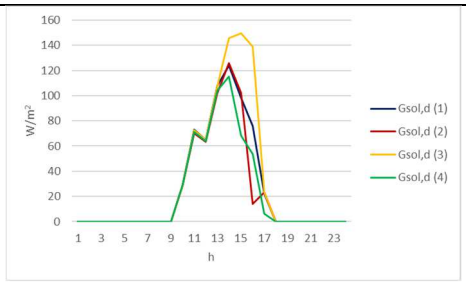

De Bilt - January 21st

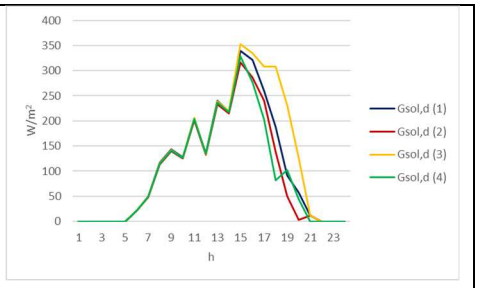

De Bilt - July 21st

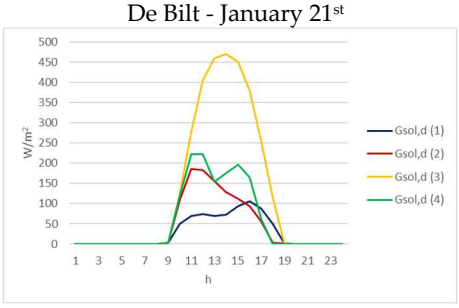

Malaga - January 21st

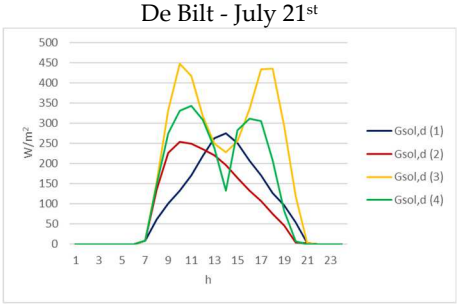

Malaga - July 21st

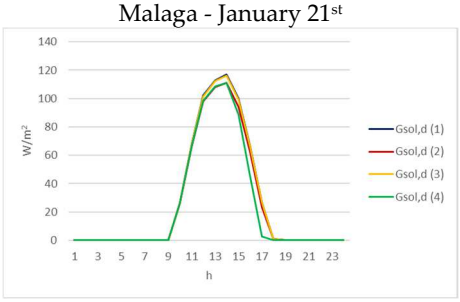

Paris - January 21st

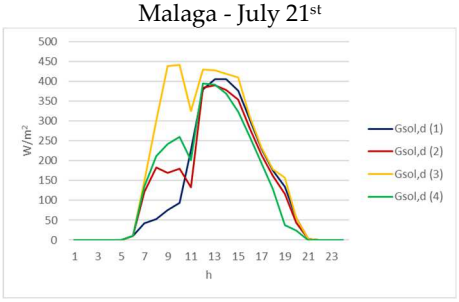

Paris - July 21st

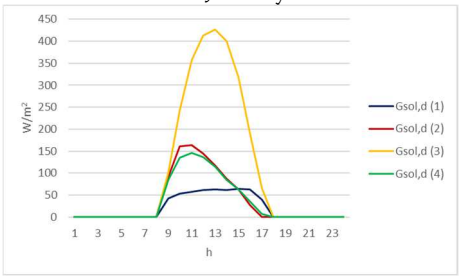

Rome - January 21st

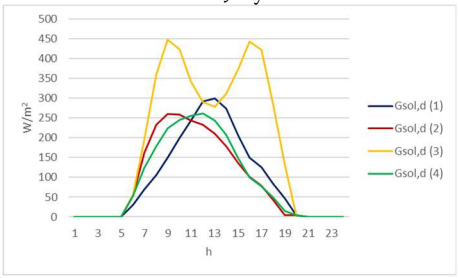

Rome - July 21st

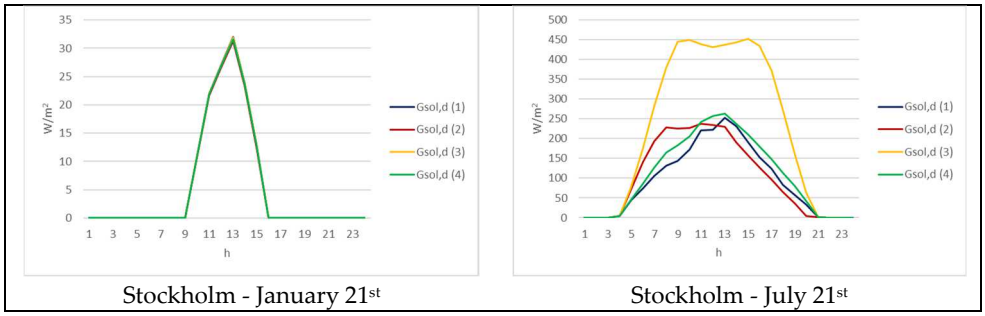

Stockholm - January 21st | Stockholm - July 21st

Figure B1.1 Comparison between the models for the separation of direct and diffuse solar irradiance on the horizontal plane. Gsol,d(1): Perez 1991, Gsol,d (2): Boland and Ridley 2007, Gsol,d (3): Erbs 1982, Gsol,d (4): Reindl 1990

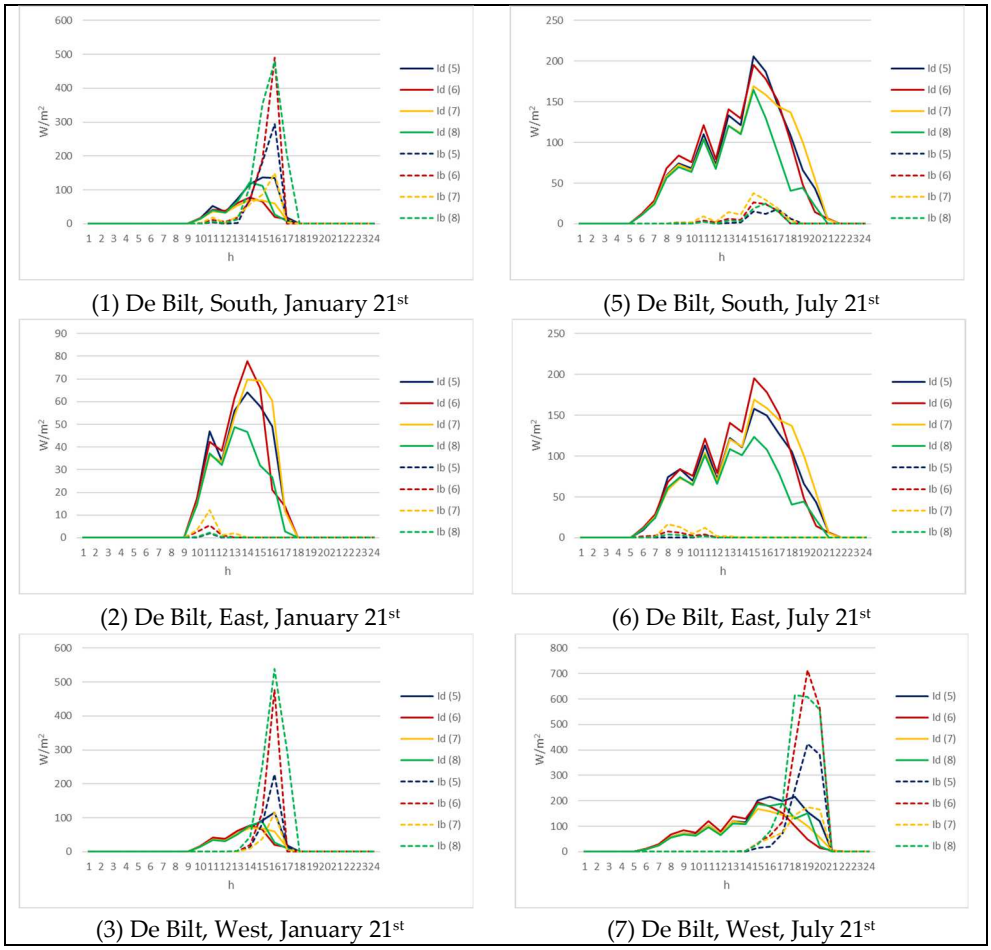

(1) De Bilt, South, January 21st | (5) De Bilt, South, July 21st

(2) De Bilt, East, January 21st | (6) De Bilt, East, July 21st

(3) De Bilt, West, January 21st | (7) De Bilt, West, July 21st

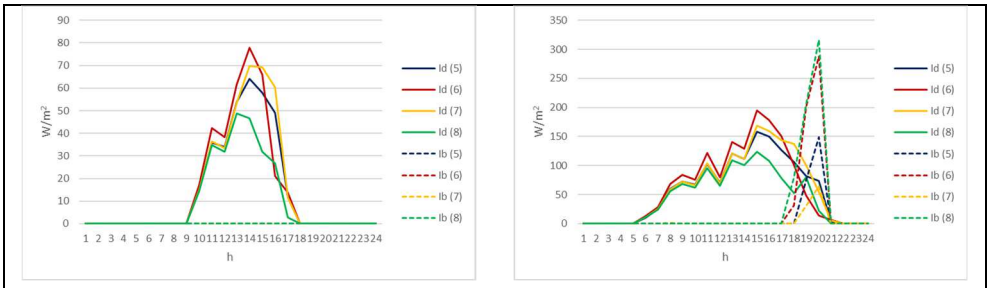

(4) De Bilt, North, January 21st (8) De Bilt, North, July 21st

Figure B1.2 Comparison between the models for separation of direct (I,b) and diffuse (I,d) solar irradiance on the vertical plane for the De Bilt location. I,d/b (5): Perez 1991+Perez 1990, I,d/b (6): Boland/Ridley 2007+Liu/Jordan 1960, I,d/b (7): Erbs 1982+Perez 1990, I,d/b (8): Reindl 1990+Perez 1990.

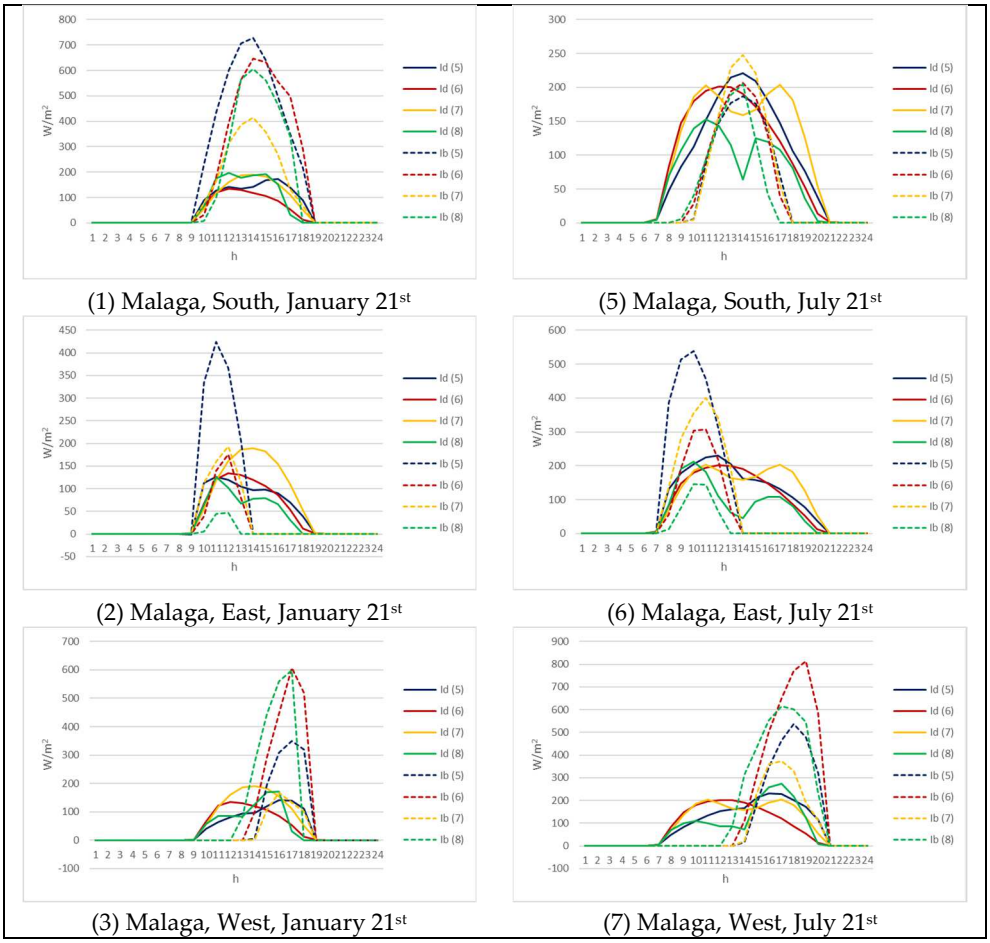

(1) Malaga, South, January 21st (5) Malaga, South, July 21st

(2) Malaga, East, January 21st (6) Malaga, East, July 21st

(3) Malaga, West, January 21st (7) Malaga, West, July 21st

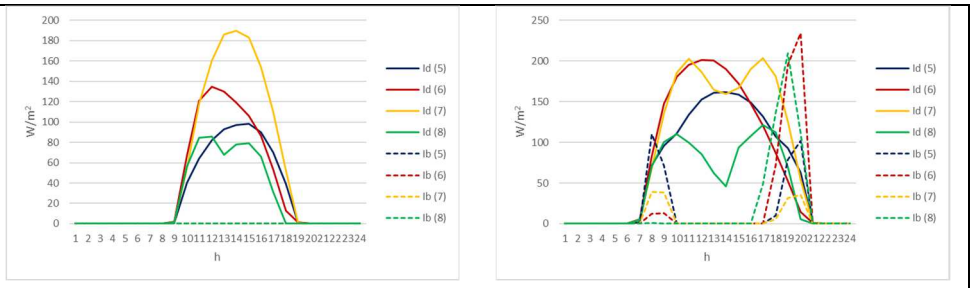

(4) Malaga, North, January 21st (8) Malaga, North, July 21st

Figure B1.3 Comparison between the models for separation of direct (I,b) and diffuse (I,d) solar irradiance on the vertical plane for the Malaga location. I,d/b (5): Perez 1991+Perez 1990, I,d/b (6): Boland/Ridley 2007+Liu/Jordan 1960, I,d/b (7): Erbs 1982+Perez 1990, I,d/b (8): Reindl 1990+Perez 1990.

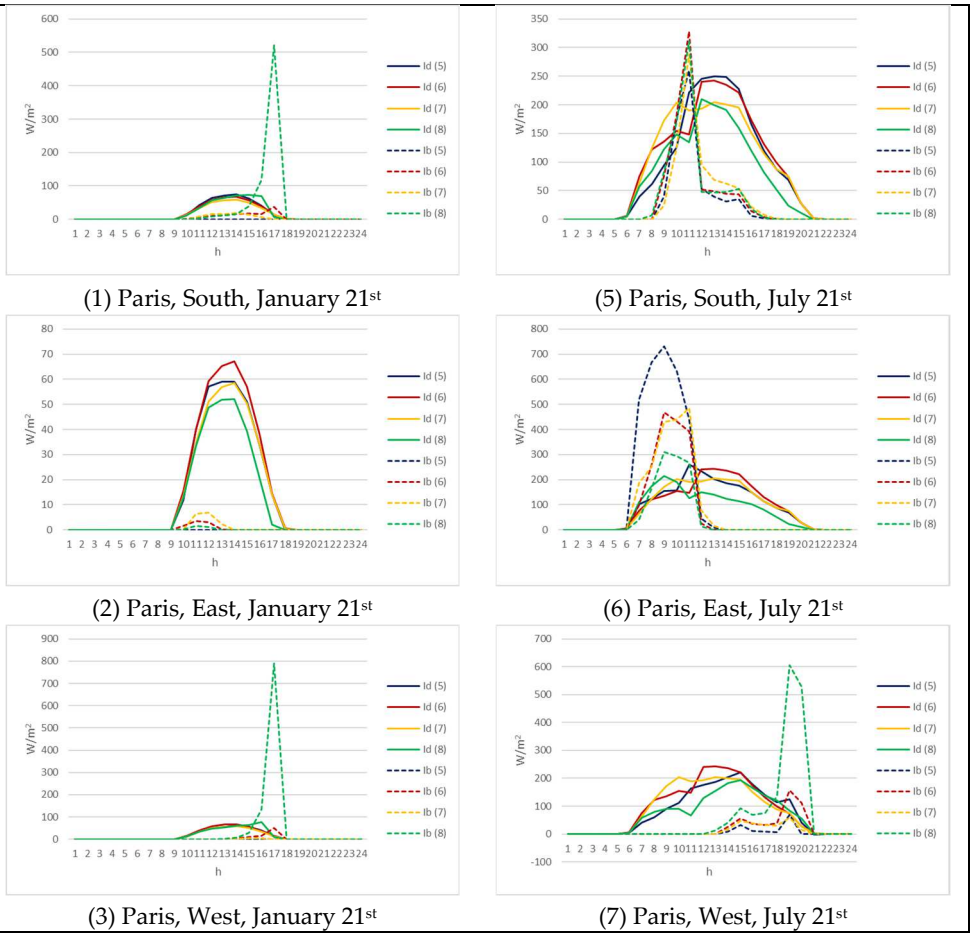

(1) Paris, South, January 21st (5) Paris, South, July 21st

(2) Paris, East, January 21st (6) Paris, East, July 21st

(3) Paris, West, January 21st (7) Paris, West, July 21st

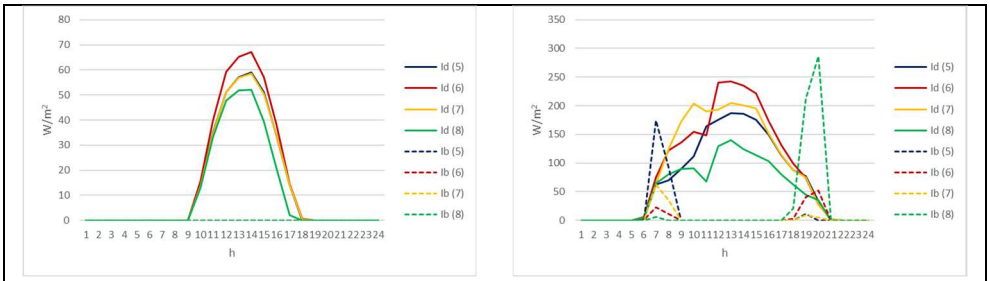

(4) Paris, North, January 21st (8) Paris, North, July 21st

Figure B1.4 Comparison between the models for separation of direct (I,b) and diffuse (I,d) solar irradiance on the vertical plane for the Paris location. I,d/b (5): Perez 1991+Perez 1990, I,d/b (6): Boland/Ridley 2007+Liu/Jordan 1960, I,d/b (7): Erbs 1982+Perez 1990, I,d/b (8): Reindl 1990+Perez 1990.

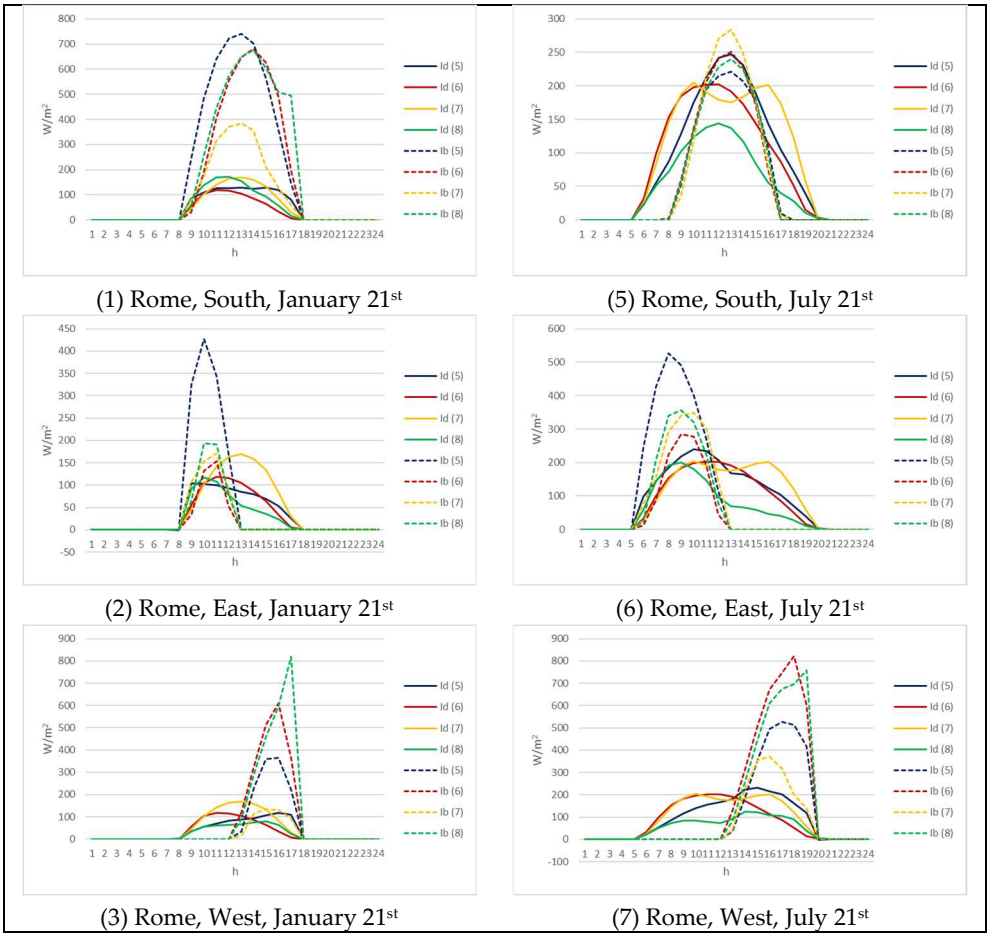

(1) Rome, South, January 21st (5) Rome, South, July 21st

(2) Rome, East, January 21st (6) Rome, East, July 21st

(3) Rome, West, January 21st (7) Rome, West, July 21st

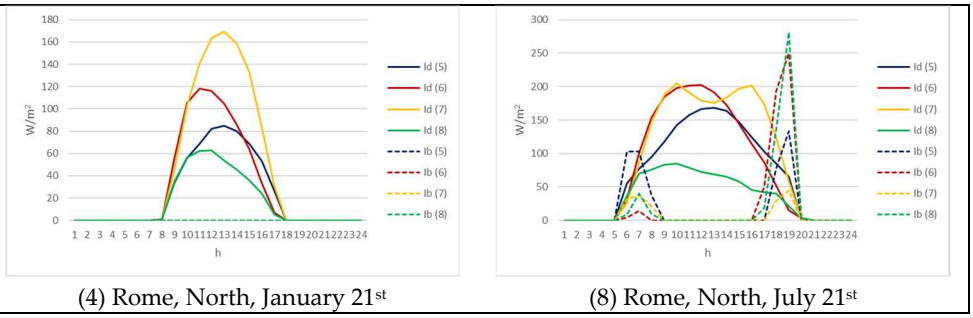

(4) Rome, North, January 21st (8) Rome, North, July 21st

Figure B1.5 Comparison between the models for separation of direct (I,b) and diffuse (I,d) solar irradiance on the vertical plane for the Rome location. I,d/b (5): Perez 1991+Perez 1990, I,d/b (6): Boland/Ridley 2007+Liu/Jordan 1960, I,d/b (7): Erbs 1982+Perez 1990, I,d/b (8): Reindl 1990+Perez 1990.

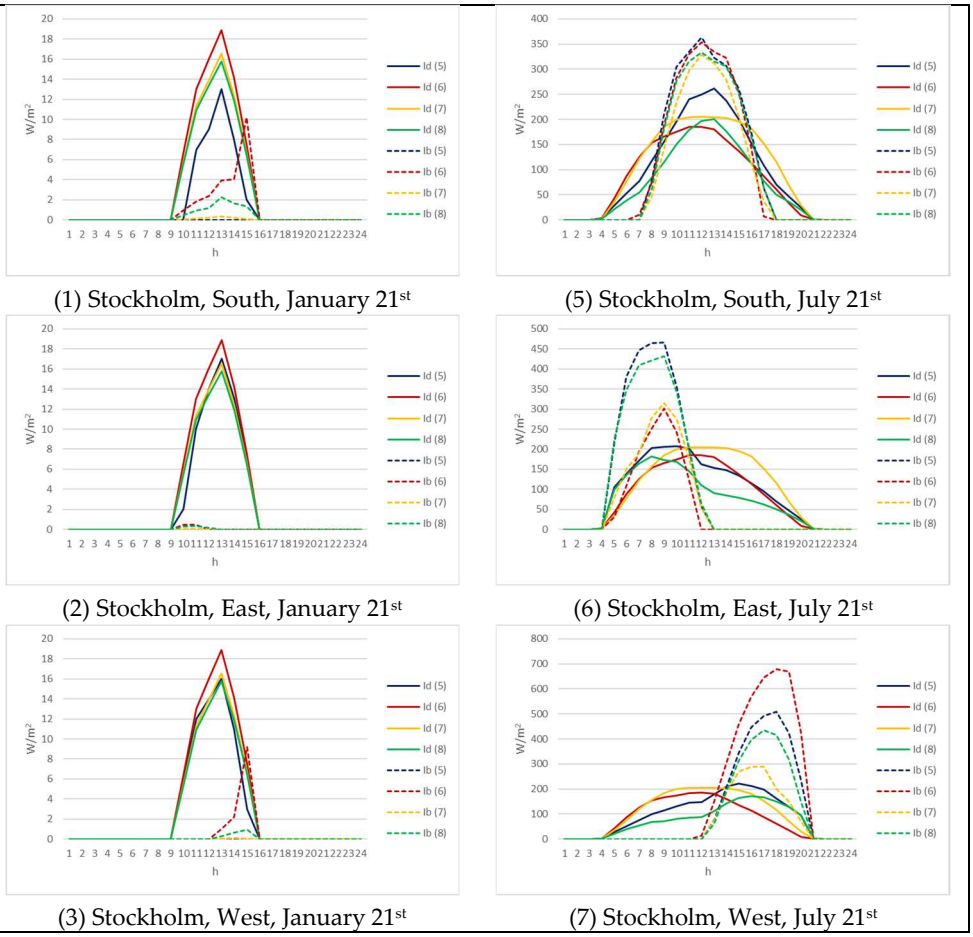

(1) Stockholm, South, January 21st (5) Stockholm, South, July 21st

(2) Stockholm, East, January 21st (6) Stockholm, East, July 21st

(3) Stockholm, West, January 21st (7) Stockholm, West, July 21st

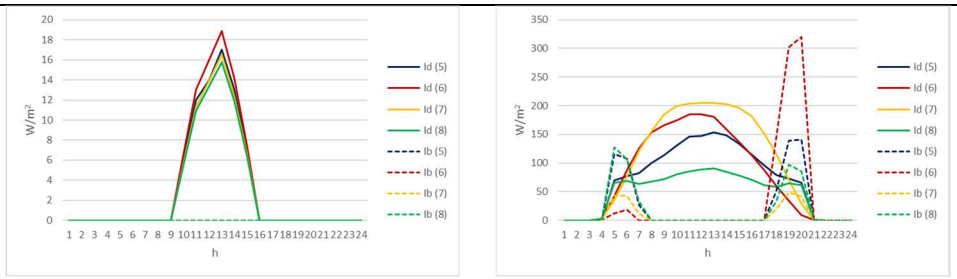

(4) Stockholm, North, January 21st (8) Stockholm, North, July 21st

Figure B1.6 Comparison between the models for separation of direct (I,b) and diffuse (I,d) solar irradiance on the vertical plane for the Stockholm location. I,d/b (5): Perez 1991+Perez 1990, I,d/b (6): Boland/Ridley 2007+Liu/Jordan 1960, I,d/b (7): Erbs 1982+Perez 1990, I,d/b (8): Reindl 1990+Perez 1990.

B.2. Comparison of standard statistical parameters

De Bilt		Perez 1991 + Perez 1990 VS Reindl 1990 + Perez 1990			Boland et al 2007+ Liu et al1960 VS Reindl 1990 + Perez 1990			Erbs 1982 + Perez 1990 VS Reindl 1990 + Perez 1990		
		I,d	I,b	I,g	I,d	I,b	I,g	I,d	I,b	I,g
S	Δ(Xmax)	30,34%	-14,13%	**-4,98%**	6,17%	-9,69%	**-8,89%**	-10,55%	-39,29%	**-20,32%**
	MBE%	22,74%	-5,90%	**8,34%**	3,74%	-4,21%	**-0,26%**	6,99%	-27,93%	**-10,58%**
	RMSE%	59,13%	104,86%	**53,16%**	41,93%	60,24%	**38,59%**	55,17%	136,91%	**73,20%**
E	Δ(Xmax)	21,96%	59,70%	**40,91%**	12,50%	12,09%	**2,05%**	-5,22%	8,47%	**9,91%**
	MBE%	35,90%	162,86%	**64,74%**	31,11%	23,17%	**29,31%**	35,22%	72,15%	**43,61%**
	RMSE%	75,10%	607,93%	**160,53%**	83,54%	96,03%	**68,04%**	103,53%	221,48%	**96,84%**
W	Δ(Xmax)	21,70%	-22,81%	**-13,13%**	10,63%	0,08%	**4,20%**	-6,79%	-53,51%	**-34,40%**
	MBE%	19,92%	-54,93%	**-26,13%**	13,86%	-19,74%	**-6,81%**	17,43%	-71,13%	**-37,05%**
	RMSE%	63,10%	166,20%	**90,24%**	73,80%	101,01%	**67,72%**	71,21%	212,00%	**130,78%**
N	Δ(Xmax)	16,01%	-40,37%	**-26,35%**	50,03%	-15,98%	**-12,83%**	26,40%	-78,43%	**-49,46%**
	MBE%	34,39%	-59,57%	**16,99%**	54,64%	-35,16%	**38,02%**	59,49%	-82,56%	**33,19%**
	RMSE%	75,73%	488,13%	**102,52%**	113,08%	303,60%	**106,97%**	131,88%	533,17%	**138,81%**

Table B2.1 - Comparison of standard statistical parameters for the De Bilt location. Evaluation against Trnsys' algorithm of all oriented vertical surfaces. Gray cells are those with the minimum error.

Malaga		Perez 1991 + Perez 1990 VS Reindl 1990 + Perez 1990			Boland et al 2007+ Liu et al1960 VS Reindl 1990 + Perez 1990			Erbs 1982 + Perez 1990 VS Reindl 1990 + Perez 1990		
		I,d	I,b	I,g	I,d	I,b	I,g	I,d	I,b	I,g
S	Δ(Xmax)	34,49%	1,21%	**7,73%**	15,12%	5,98%	**6,77%**	-9,79%	-30,31%	**-12,42%**
	MBE%	27,87%	20,33%	**23,57%**	9,61%	13,94%	**12,08%**	26,03%	-11,79%	**4,47%**
	RMSE%	77,08%	99,80%	**58,44%**	54,75%	70,71%	**42,01%**	66,05%	92,28%	**56,67%**
E	Δ(Xmax)	28,21%	218,76%	**97,49%**	18,52%	91,92%	**34,83%**	-7,13%	116,16%	**54,76%**
	MBE%	52,53%	526,58%	**143,42%**	42,15%	174,41%	**67,51%**	63,44%	307,06%	**110,15%**
	RMSE%	98,71%	1322,82%	**287,48%**	99,91%	459,16%	**128,30%**	128,34%	745,61%	**190,48%**
W	Δ(Xmax)	10,51%	-18,04%	**-10,42%**	0,49%	1,38%	**3,82%**	-21,26%	-47,34%	**-29,17%**
	MBE%	20,13%	-46,11%	**-25,25%**	11,75%	-10,85%	**-3,73%**	28,48%	-65,22%	**-35,71%**
	RMSE%	71,28%	119,36%	**76,03%**	87,45%	92,14%	**64,50%**	72,56%	145,87%	**97,14%**
N	Δ(Xmax)	17,39%	-34,74%	**-24,56%**	53,57%	-5,27%	**-8,69%**	20,34%	-75,69%	**-35,20%**
	MBE%	44,03%	-44,83%	**27,89%**	68,27%	-16,74%	**52,83%**	93,47%	-75,82%	**62,73%**
	RMSE%	93,44%	392,24%	**94,82%**	131,30%	239,18%	**115,57%**	158,28%	433,39%	**136,06%**

Table B2.2 - Comparison of standard statistical parameters for the Malaga location. Evaluation against Trnsys' algorithm of all oriented vertical surfaces. Gray cells are those with the minimum error

Paris		Perez 1991 + Perez 1990 VS Reindl 1990 + Perez 1990			Boland et al 2007+ Liu et al1960 VS Reindl 1990 + Perez 1990			Erbs 1982 + Perez 1990 VS Reindl 1990 + Perez 1990		
		I,d	I,b	**I,g**	I,d	I,b	**I,g**	I,d	I,b	**I,g**
S	$\Delta(x_{max})$	37,59%	-7,34%	**-0,16%**	9,14%	-3,41%	**-1,98%**	-10,39%	-20,66%	**-6,40%**
	MBE%	23,69%	-1,78%	**10,78%**	6,88%	-2,75%	**1,99%**	11,47%	-23,58%	**-6,30%**
	RMSE%	65,50%	110,26%	**56,95%**	45,18%	74,15%	**42,87%**	56,30%	128,21%	**69,34%**
E	$\Delta(x_{max})$	28,36%	89,54%	**56,17%**	15,21%	37,70%	**16,01%**	-5,41%	34,91%	**26,71%**
	MBE%	39,89%	229,33%	**80,39%**	35,46%	50,47%	**38,67%**	41,28%	113,67%	**56,76%**
	RMSE%	84,41%	804,13%	**196,18%**	92,22%	189,60%	**82,22%**	109,06%	338,68%	**117,73%**
W	$\Delta(x_{max})$	15,09%	-21,37%	**-9,90%**	-2,44%	0,28%	**4,70%**	-19,89%	-36,62%	**-19,48%**
	MBE%	18,58%	-54,52%	**-27,47%**	13,81%	-22,41%	**-9,01%**	18,70%	-70,49%	**-37,48%**
	RMSE%	63,83%	160,03%	**90,46%**	78,69%	107,34%	**70,67%**	69,46%	198,72%	**125,55%**
N	$\Delta(x_{max})$	21,55%	-56,34%	**-43,43%**	55,31%	-32,50%	**-29,88%**	27,52%	-83,10%	**-57,27%**
	MBE%	36,38%	-56,57%	**19,40%**	58,20%	-34,20%	**41,32%**	65,00%	-81,57%	**38,22%**
	RMSE%	81,37%	492,61%	**104,64%**	120,88%	271,01%	**109,29%**	136,56%	530,15%	**139,14%**

Table B2.3 - Comparison of standard statistical parameters for the Paris location. Evaluation against Trnsys' algorithm of all oriented vertical surfaces. Gray cells are those with the minimum error.

Rome		Perez 1991 + Perez 1990 VS Reindl 1990 + Perez 1990			Boland et al 2007+ Liu et al1960 VS Reindl 1990 + Perez 1990			Erbs 1982 + Perez 1990 VS Reindl 1990 + Perez 1990		
		I,d	I,b	**I,g**	I,d	I,b	**I,g**	I,d	I,b	**I,g**
S	$\Delta(x_{max})$	24,62%	3,99%	**4,89%**	12,69%	7,54%	**4,40%**	-11,03%	-27,00%	**-16,70%**
	MBE%	27,13%	3,07%	**14,44%**	10,97%	1,99%	**6,23%**	18,08%	-19,73%	**-1,86%**
	RMSE%	56,49%	47,61%	**33,42%**	53,41%	48,80%	**33,04%**	62,93%	90,58%	**53,24%**
E	$\Delta(x_{max})$	28,55%	9,40%	**10,72%**	19,42%	-20,39%	**-15,30%**	-5,72%	-15,76%	**-6,24%**
	MBE%	33,22%	37,86%	**35,17%**	27,10%	-38,40%	**-0,39%**	35,24%	-8,35%	**16,95%**
	RMSE%	66,59%	142,41%	**74,94%**	75,00%	128,17%	**71,55%**	98,67%	96,95%	**74,53%**
W	$\Delta(x_{max})$	33,17%	-11,89%	**-4,03%**	22,05%	6,11%	**7,89%**	-3,65%	-44,25%	**-25,84%**
	MBE%	31,92%	-22,80%	**1,58%**	27,29%	31,43%	**29,59%**	35,44%	-49,53%	**-11,68%**
	RMSE%	66,78%	95,35%	**46,65%**	96,91%	118,51%	**68,20%**	91,65%	178,94%	**103,64%**
N	$\Delta(x_{max})$	24,07%	-37,21%	**-23,67%**	58,56%	-10,34%	**-9,94%**	25,18%	-73,52%	**-39,47%**
	MBE%	44,87%	-10,83%	**38,89%**	69,33%	23,07%	**64,37%**	80,19%	-61,93%	**64,92%**
	RMSE%	86,23%	353,62%	**82,61%**	133,56%	342,72%	**122,85%**	153,35%	470,80%	**141,02%**

Table B2.4 - Comparison of standard statistical parameters for the Rome location. Evaluation against Trnsys' algorithm of all oriented vertical surfaces. Gray cells are those with the minimum error

Stockholm		Perez 1991 + Perez 1990 VS Reindl 1990 + Perez 1990			Boland et al 2007+ Liu et al1960 VS Reindl 1990 + Perez 1990			Erbs 1982 + Perez 1990 VS Reindl 1990 + Perez 1990		
		I,d	I,b	**I,g**	I,d	I,b	**I,g**	I,d	I,b	**I,g**
S	$\Delta(x_{max})$	40,64%	-4,82%	**3,58%**	0,60%	0,31%	**-0,81%**	-9,62%	-34,59%	**-21,18%**
	MBE%	20,61%	5,11%	**11,91%**	-3,71%	0,60%	**-1,29%**	5,79%	-30,08%	**-14,33%**
	RMSE%	47,62%	57,05%	**35,33%**	55,08%	86,69%	**49,68%**	58,92%	99,29%	**62,27%**
E	$\Delta(x_{max})$	31,42%	-17,25%	**-5,59%**	9,12%	-28,67%	**-20,54%**	-1,97%	-45,95%	**-28,17%**
	MBE%	23,81%	-14,81%	**2,65%**	14,37%	-60,86%	**-26,86%**	25,65%	-51,48%	**-16,62%**
	RMSE%	54,97%	83,04%	**43,26%**	64,20%	195,95%	**115,37%**	95,17%	180,20%	**110,76%**
W	$\Delta(x_{max})$	42,31%	8,85%	**12,95%**	14,08%	32,37%	**28,17%**	2,49%	-33,10%	**-13,75%**
	MBE%	29,12%	27,51%	**28,39%**	18,39%	104,38%	**57,58%**	30,07%	-27,63%	**3,77%**
	RMSE%	61,77%	114,00%	**64,87%**	104,65%	307,78%	**124,07%**	104,20%	122,84%	**85,44%**
N	$\Delta(x_{max})$	35,93%	-45,51%	**-33,59%**	58,00%	-23,96%	**-23,86%**	41,95%	-73,50%	**-57,62%**
	MBE%	37,84%	-13,39%	**28,77%**	55,76%	15,02%	**48,54%**	71,12%	-65,60%	**46,91%**
	RMSE%	77,00%	269,28%	**76,67%**	123,96%	706,72%	**151,92%**	157,13%	425,00%	**148,64%**

Table B2.5 - Comparison of standard statistical parameters for the Stockholm location. Evaluation against Trnsys' algorithm of all oriented vertical surfaces. Gray cells are those with the minimum error.